Process Parameter Optimisation of Steel Components Laser Forming using a Taguchi Design of Experiments Approach

Student Name Siyasanga Sobetwa

Student Number: 312597

A research report submitted to the Faculty of Engineering and the Built Environment, University of the Witwatersrand, Johannesburg, in partial fulfilment of the requirements for the degree of Master of Science in Engineering.

Date: September 2017, Johannesburg

Declaration

I declare that this dissertation is my own unaided work. It is being submitted to the Degree of Master of Science of Engineering to the University of the Witwatersrand, Johannesburg. It has not been submitted before for any degree or examination to any other University.

Candidate: .....

Date: .....

Signature: .....

Abstract

The focus in this research investigation is to investigate the Process Parameter Optimisation in Laser Beam Forming (LBF) process using the 4.4 kW Nd: YAG laser system – Rofin DY 044 to form 200 x 50 x 3 mm^3 mild steel - AISI 1008 samples. The laser power P, beam diameter B, scan velocity V, number of scans N, and cooling flow C were the five input parameters of interest in the investigation because of their influence in the final formed product. Taguchi Design of Experiment (DoE) was used for the selection and combination of input parameters for LBF process. The investigation was done experimentally and computationally. Laser Beam Forming (LBF) input parameters were categorised to three different levels, low (L), medium (M), and high (H) laser forming (LBF) parameters to evaluate parameters that yield maximum bending and better surface finish/quality. The conclusion drawn from LBF process is that samples which are LBFormed using low parameter settings had unnoticeable bending and good material surface finishing. On the other hand, samples LBFormed using medium parameters yielded visible bending and non-smooth surface finishing, while samples processed using high LBF parameters yielded maximum bending and more surface roughness than the other two process parameters.

Acknowledgements

The first person that needs to be thanked for making this report possible is Mr Stephen Akinlabi for paving the way as my first supervisor and for procuring the materials used for the investigation and for facilitating the booking of laser time from CSIR. Prof. Claudia Polese, thank you for accepting to take over as my supervisor, while my supervisor had to go away. You accepted to take over whilst there was still no light in this research and with your guidance, patience, and resourcefulness this journey became easier with certainty. Prof. Alexander Ziegler and Dr Deran Reddy of the Wits University Microscopy and Microanalysis Unit (MMU) for giving me access to use the microscopes.

Table of Contents

List of Figures

List of Tables

Nomenclature

Symbol	Definition	Units
ANOVA	Analysis of Variance	
DOE	Design of Experiments	
HLFP	High Laser Forming Parameter	
HP	High Parameter	
HV	Vickers Hardness number	
LBF	Laser Beam Forming	
LLFP	Low Laser Forming Parameter	
LF	Laser Forming/Formed	
LP	Low Parameter	
MLFP	Medium Laser Forming Parameter	
MP	Medium Parameter	
RSM	Surface Response Method	
TGM	Temperature Gradient Mechanism	
BM	Buckling Mechanism	
UPM	Upset Mechanism	
PM	Point Mechanism	
LST	Laser Surface Texturing	
SPIF	Single Point Incremental Forming	

Chapter 1

Literature Survey & Research Objectives

This chapter provides an introduction to the broad concepts that are investigated and evaluated within this report. A detailed literature survey that gives an overview on Laser Beam Forming (LBF) process is covered. The literature also discusses the process parameters, stress and stress behaviour on LBFormed material. The reader is also introduced to the general topic of mild steel base material, Design of Experiments (DOE), and response surface method (RSM) which goes hand in hand with laser forming research work that is available in literature.

1. Introduction

This section provides a basic introduction to LBF and more specifically the LBF of steel components which is the focus of this research. The summary and the research motivation on LBF is also presented in this chapter. LBF is a manufacturing process which originated from flame bending or line heating process. LBF is a process whereby defocused laser beam induces thermal stresses to the material without melting the surface of a work piece in order to produce controlled distortion on the work piece. Consequently, the laser induces plastic strains, bending the material with a heat source which is mainly used for straightening and curving steel components. A

graphical depiction of a common laser forming machine setup is illustrated in Figure 1-1.

Figure 1-1 shows the laser light which is energised with the power P1 pointing in the Z direction and moving along the x axis towards the right being introduced to the material.

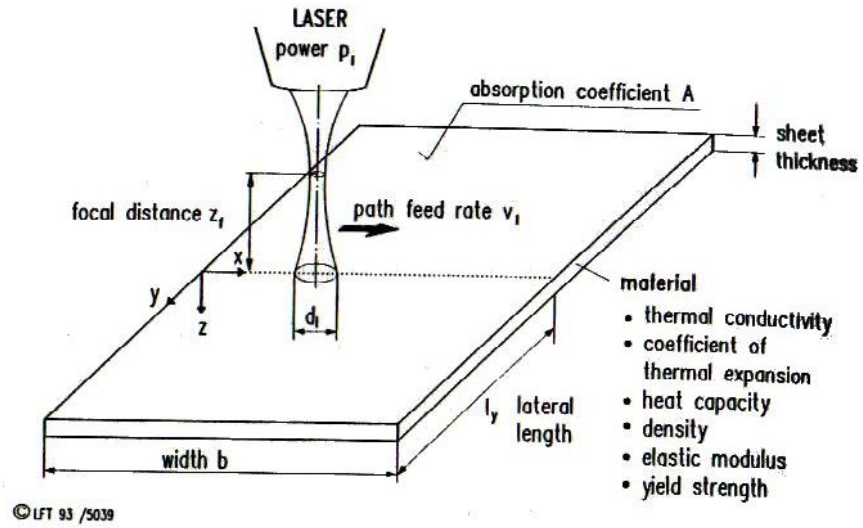

Figure 1-1 Schematic of the Laser Beam Forming process [1]

The process is principally used at macro level to form metallic sheet material. The principle behind LBF of metal sheet, is that a guided laser beam moves across the surface of the material to create the desired shape. The path of the laser is dependent on the desired forming result. In the simplest case, laser beam may be a point and in another case it may be a straight line, a rotating beam across the whole part.

The study and the modification of laser beam geometry or the orientation has become essential in the LBF process because it is one possible method of varying the temperature distribution without changing the input power or scanning speed [3]. The

effect of beam geometry on laser bending and the result from investigations from the literature suggests that, the beam geometry plays an important role in the resulting temperature distributions on the work piece [3]. Longer beam dimension in the scanning direction produces higher temperatures due to longer beam-material interaction time. It is implied that higher temperatures produce more plastic strains and hence higher deformation [3].

LBF has several distinct mechanisms which are the temperature gradient mechanism (TGM), buckling mechanism (BM), upsetting mechanism (UPM), and point mechanism (PM). The most extensively studied mechanisms are the TGM and BM which depend on the laser setup. Table 1-1 is the summary of LBF mechanisms.

Table 1-1 Summary of Laser Forming Mechanism [4]

Laser Beam Forming Mechanisms			
Principle	**Process variables**	**Applications**	**Formed Curvature**
TGM	-Rapid scan velocity - Small beam diameter or the same plate thickness -Mostly used in thick plates	Form thick plates	Curvature is towards the beam
BM	-Slow scan velocity - Plate thickness: thin - Large beam diameter	Form thin plates	Depend on boundary conditions
UPM	-Slow scan velocity - Large beam diameter or the same as the plate thickness - Thick and stiff plates	Alignment and adjustment	Thickening of the curvature
PM	- Moderate scan velocity - Thin plate - Small beam diameter	Form micro-components	Form spot rather than line pattern

The LBF process can be categorised into two groups which are basic single line two dimensional (2D) forming, which produces shapes that are folds of varying angles.

The second group is a more complex multi-line three dimensional (3D) forming, that produces continuous surfaces. Three dimensional (3D) forming comprises of developable forming, which is a series of (2D) bends producing a surface with single curvature and non-developable forming, which makes use of the shortening mechanism to produce a surface containing a double curvature [4-5].

A. Laser Beam Forming Process Parameters

The best approach to initiate LBF operation, is to consider the process parameters that will yield a suitable bending angle and surface quality to a given piece of material. The laser power P, beam diameter B, scan velocity V, number of scans N, and the cooling flow C are very important process parameters in LBF process. This is because these process parameters influence the bending angle which have significant effect on the ultimate material surface finishing. LBF process can also be optimised by using the following material parameters, thermal conductivity, and coefficient of thermal expansion, heat capacity, elastic modulus, yield stress, and the rate of laser absorption [5]. Good results in LBF process are achieved with the ability to optimise process parameters to suit process variables [5]. Important LBF process parameters and significant material variables are generally taken into consideration whenever the LBF process is carried out, refer to Figure 1-1.

B. Stress and Strain Behaviour on Laser Beam Formed Material

The stress and strain behaviour on LBFormed material is used to investigate the effect of different beam geometries and their contribution on stress and strain behaviour on a material. This stress and strain behaviour effect on LBFormed material is expressed

by plotting a stress-strain curve. Stresses and strains in the x-direction are chosen due to their significant contribution to the bending formation, see Figure 1-2 [6]. The strain ε_x consists of plastic and elastic components. Figure 1-2 shows a typical stress-strain path during a laser scan. Generally, the steps are divided into four stages which are; pre-heating, heating, post-heating and cooling [6]

The stages are explained as follows.

Preheating. This is the stage when laser scan starts and moves towards the measured point, i.e. the area where the laser cutting or bending is required. The plate is assumed to be free from any residual stresses and strains and hence the plot starts at the origin (0, 0) in Figure 1-2. The area on the material where the laser beam is starting to be introduced, the stresses and strains are tensile. This is due to the expansion of the heated region behind the measured point. The maximum tensile stress is produced just before the laser beam reaches the measured point [6].

Heating. This is the stage when the measured point is heated by the beam. During heating, the stress rapidly changes into compression. This is because the material expansion is restricted by the surrounding material (path 1-a). With increasing temperature during the heating stage, the material flow stress reduces (step a-b) due to the effect of the temperature-dependent material properties. Compressive plastic strain continues to develop at constant flow stress (step b-2) [6]

Post-heating. This is the stage when the laser beam leaves the reference point and moves towards the exit path. At this point, the temperature starts to drop. As the temperature drops, the thermal strain reduces leaving plastic and residual elastic

strain (path 2-c). In addition, compressive stress reduces and becomes tensile (path 2-3) [6].

Cooling. This is the period after the laser scan path is completed. During this stage, the temperature and thermal strain continue to drop. The compressive plastic strain in x-direction increases slightly due to the thermal shrinkage in both the z- and y-direction. Figure 1-2 is a typical stress-strain response during a laser scan.

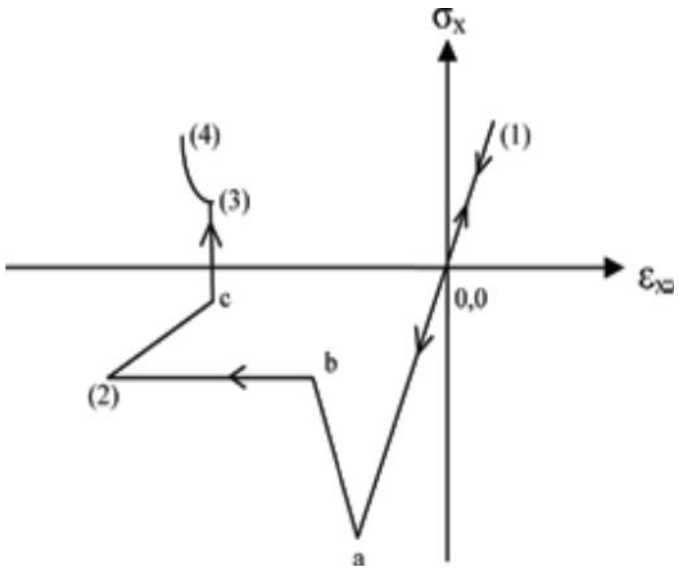

Figure 1-2 Typical stress-strain response during a laser scan [6]

1.1 Laser Bending of Stainless Steel

A study on laser bending of AISI 304 stainless steel sheet using a high power (2 kW) continuous wave CO2 laser with a 3mm beam diameter was looked at [7]. The main process variables taken into account were incident power density, scan speed, number of passes and sheet thickness. A detailed characterization of the bent sheet was carried out by measuring the bending angle, detailed microstructural study, and phase analysis. The micro-hardness of the bent sheet at different positions was carefully measured using a Vickers micro-hardness tester. Bending angle, microstructural and mechanical properties of the bent sheet were correlated with laser parameters and sheet thickness to derive an optimum processing zone for laser bending. Table 1.2 is a summary of the LBF process parameters used in LBF of AISI 304 stainless steel sheet.

Table 1-2 Summary of Process Parameters (Sheet thickness, Power density, Scan speed, Number of passes) Employed in laser Bending of AISI 304 stainless Steel [7]

Sheet thickness (mm)	Power density (kW/cm^2)	Scan speed (mm/min)	Number of passes
0.9	13–55	4000–6000	5–40
1.6	13–55	1000–2500	5–40

The bending angle for the AISI 304 stainless steel sheet obtained using the process parameters in Table 1.2 were measured and correlated. Figure 1.1-1 shows the effect of scan speed (v) on the bending angle for laser bent AISI 304 stainless steel sheet of thickness (t) (a) 1.6mm and (b) 0.9 mm, respectively.

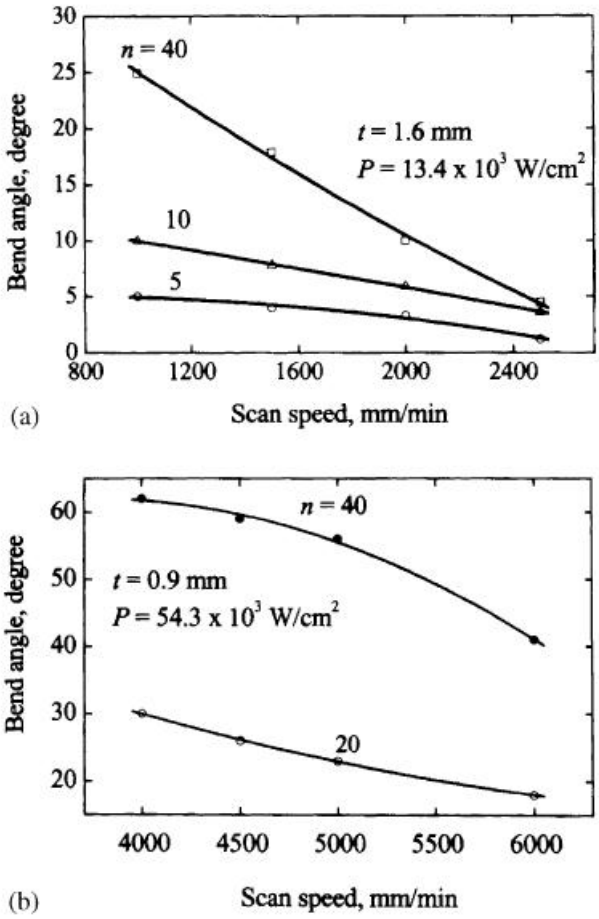

Figure 1.1-1 Variation of angle of bending with scan speed in laser bent AIS 304 stainless steel sheet with a thickness of (a) 1.6mm and (b) 0.9 mm, respectively [7]

Figure 1.1-1 demonstrates that the bending angle varies inversely with the scan speed for both sheet thicknesses. The decreased bending angle with increase in scan speed is attributed to decreased absorbed energy with increasing scan speed (because of a lower interaction time at a higher scan speed), leading to a lower thermal stress and hence, a lower bending angle. In this regard, it is relevant to mention that though bending angle increases with decrease in scan speed, application of a very low scan speed leads to evaporation of material from the surface and hence, crater formation.

Figure 1.1-1 also demonstrates the effects of number of passes (*n*) on the angle of bending. A careful observation of Figure 1.1-1(a) and (b) shows that bend angle increases with increase in number of passes for both sheet thicknesses. Figure 1.1-1(b) shows that higher bending for a 1.6mm sheet AISI 304 stainless steel is achieved at a higher interaction time (lower scan speed). Also, the range of scan speeds used for bending the 1.6mm thick sheet without the adverse effect of surface evaporation is between 500 mm/min–3000 mm/min. These results are significantly lower when compared to those achieved for bending angles of a 0.9mm thick which are between (3500 mm/min–7500 mm/min).

Furthermore, bending angle that is achieved in the case of 0.9mm thick stainless steel plate is from $1° - 75°$ versus the bending angle of $1° - 30°$ that is achieved on a 1.6mm thick stainless steel sheet. These results show that it is easier to bend thinner materials versus thicker materials. Therefore, it may be concluded that sheet thickness also plays a role in determining the bending limit and the choice of LBF parameters to be used.

Figure 1.1-2(a) and (b) summarize the variation of bending angle with number of passes. With each pass, thermal stress proportional to thermal gradient is introduced to the LBFormed material, hence the bending angle also increases with increasing number of passes.

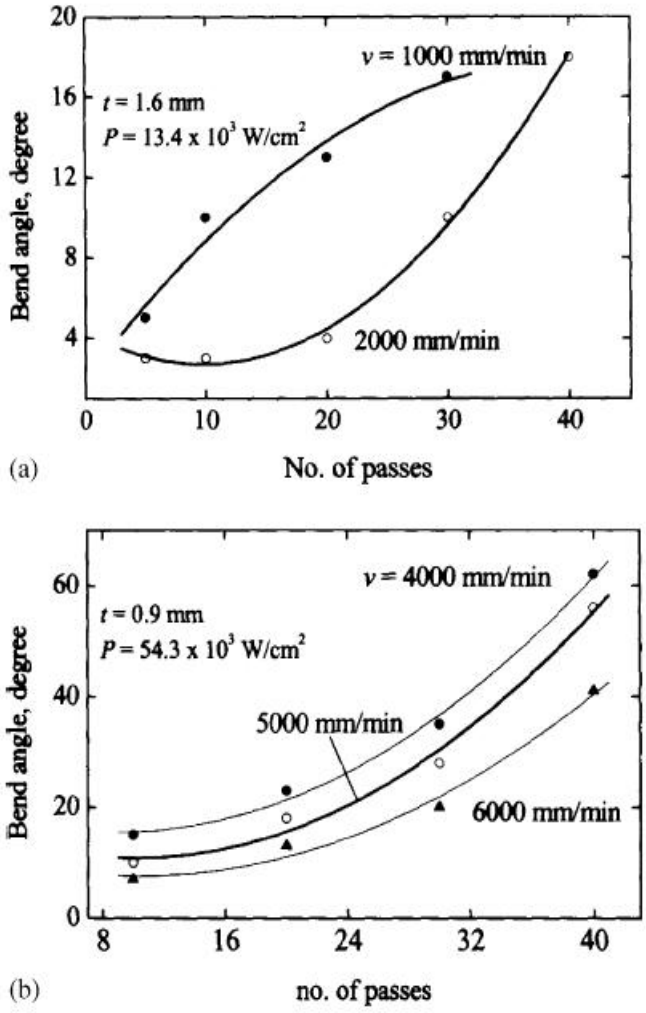

Figure 1.1-2 Variation of angle of bending with number of passes for laser bent AISI 304 stainless steel sheet with a thickness of (a) 1.6mm and (b) 0.9 mm, respectively [7].

The results from Figure 1.1-2 indicates that the increase in the number of passes result in an increase of the bending angle. An increase in bending angle with increasing laser power density *P.* Figure 1.1-2 is attributed to increased material flow at a higher absorbed energy density

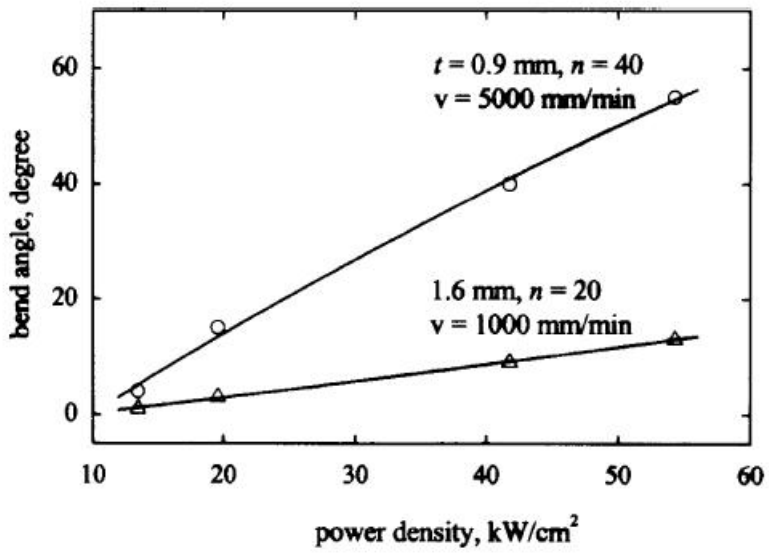

Figure 1.1-3 Variation of angle of bending with applied power density for laser bent AISI 304 stainless steel [7].

Furthermore, Figure 1.1-3 illustrates that the rate of increase in bend angle with power is, much lower for 1.6mm thick sheet than 0.9mm thick sheet. This is said to be attributed by larger thermal stresses required for bending a sheet with a higher thickness (in this instance 1.6 mm thick sheet). Cheng and Lin [8] developed an analytical model to calculate thermal stresses required for bending, which evidences the increased level of required thermal stresses with increasing sheet thickness. It is relevant to note that though the bending angle increases with increase in power density, application of a very large power density causes excessive melting and evaporation of surface material at the inner side (laser–material interaction side) of the bent region.

1.2 The Edge Effect and Longitudinal Distortion in Laser Bending Process

The literature indicates that one of the most important factors concerning the in LBF process is the sheet/material thickness. This is because an increase in sheet thickness leads to a reduction of bending angle sharply [7-9]. Bending angle is known to be inversely proportional to the beam diameter [9]. Also, when the length and the width of the sheet increases, the bending angle increases and decreases respectively when the power and speed of the beam are constant [10].

The effect of overlap in multi-pass paths indicates that when a path is scanned exactly twice by one beam, it leads to an increase in the bending angle [12]. Theoretically, by considering other factors concerning LBF i.e. sample properties, process parameters, etc. the accuracy of laser bending with good surface finishing is attainable. The non-uniformity of the bending angle along the scan path introduces an inevitable phenomenon called the ‘‘edge effect.’’ Geometrical constraints and non-uniform distribution of the temperature field caused by existence of expansion and heat conduction coefficients are the reasons behind the edge effect [13].

Theoretically, Mucha et al. [14] illustrated that the area of the sample that is irradiated by the laser beam bends, proportional to the thermal contraction that takes a curve shape in the scanning path. Also, Bao and Yao [15] investigated the edge effect phenomenon under the BM mechanism. They suggested that the maximum temperature difference along the scan path and the expansion and contraction of the top and bottom surfaces of the plate are the reasons of this phenomenon [13-15].

Shen et al. [16] proposed variable patterns of scan speed based on linear energy control to overcome this phenomenon and demonstrated that the edge effect is to some extent controllable by this method. Hu et al. [17] studied the edge effect phenomenon by means of considering three factors: beam diameter, scan speed, and laser power in the bending of an aluminium plate. Their study indicated that the beam diameter is the most effective factor leading to the edge effect.

Other statistical analysis works studied were done just to estimate the bending angle. It was illustrated that the number of passes, sheet thickness and beam features affect the bending angle [18]. Another very important issue is the undesirable deformation which occurs in LBF process and owing to that, the sheet deforms along the radiation path in the direction of the axis perpendicular to the radiation plane. This phenomenon is called longitudinal distortion and leads to a curvature in the x–y plane of the plate during LBF [19]. Yu [20] and Li and Yao [20] presented theoretical relations which implied that the longitudinal distortion and the bending angle are affected by heating conditions. Heating conditions include the heat input to the plate surface are highly dependent on the beam scan speed and the intensity of radiation. Jha et al. [20] demonstrated that the scan speed of the beam is a key factor in generating a kind of undesirable deformation in laser forming that is called multi curvature.

1.3 Temperature Gradient Mechanism in Laser Forming of Thin Plates

Laser forming is a complex transient process that involves thermodynamics, elastic–plastic mechanics, metallography, etc. Stress–strain relationship of the plate is not only nonlinear, but also a function of temperature [21]. To realize accurate forming, research on mechanisms is the key. A number of mechanisms for LBF process has been suggested in Table 1-1. Most available LBF mechanisms include the temperature gradient mechanism (TGM), the buckling mechanism (BM) and the upsetting mechanism (UM). TGM is the main forming mechanism under which LBFormed plates bends about the x-axis [3, 22]. However, previous studies have revealed that under the processing conditions of TGM, LBFormed plates do not only bend about the x-axis, but also bend about the about the y-axis. There is little research done to date about the bending of the plates about the y-axis [22]. To obtain further insights into the deformation of a plate in the laser forming process Shi, Shen, and Yao [22] studied the TGM using an analytical model of the bending angle about the y-axis using simplified assumptions.

1.3-1 Analysis of TGM

Shi, Shen, and Yao [22] illustrated that a fast scan of the sample by a laser beam forms a steep thermal gradient across the thickness that produces differential thermal expansion. At the beginning of the LBF process refer back to Figure 1-1, counter bending occurs due to the bending moment created [1, 22]. With continued heating,

the flow stress of metal decreases in the heat-affected zone. Once the thermal stress reaches the flow stress, any additional thermal expansion is converted into a plastic compressive strain because free expansion is restricted by the surrounding material [22, 23]. At the cooling stage, the small counter bending angle is quickly reversed to a large concave bending angle because of the significant shortening at the top surface caused by the action of the temperature through the thickness which serves as a strong pulling force. As a result, the plate bends about the x-axis towards the laser beam, as shown in Figure 1-6(a) [22, 23].

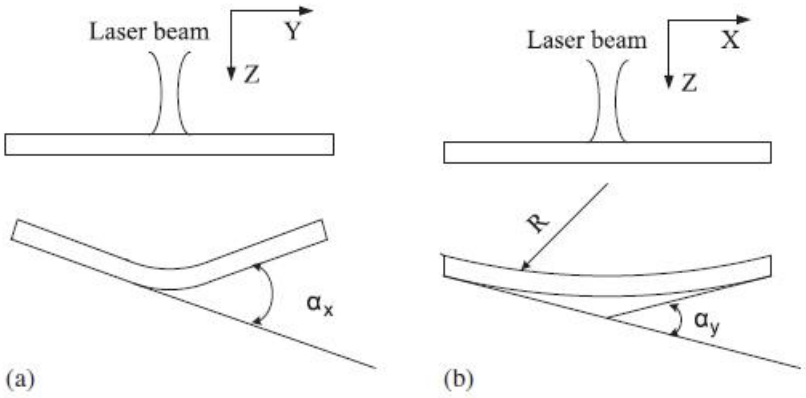

Figure 1.3-1 Temperature gradient mechanism: (a) bending about the x-axis; (b) bending about the y-axis [22].

On the other hand, the material along the x-axis also produces thermal expansion due to heating, and the expansion of the top surface is greater than that of the bottom surface. Plastic deformation is produced because free expansion is restricted by the surrounding material. At the cooling stage, the material in the top layers contracts, and then a local shortening of these layers results in making the plate bend about the y-axis towards the laser beam, as shown in Figure 1.3-1 (b) [22,23].

1.3-2 Analytical model estimate of the bending angle

When the laser beam is scanning, it is assumed that the distortion of the plate can be limited to the heated zone whose length and width are equal to the laser spot diameter d [22, 23]. In a study done by Shi, Shen, and Yao [22] on the sample top surface, the small plate is taken with length is L and width d. Refer to Figure 1-7.

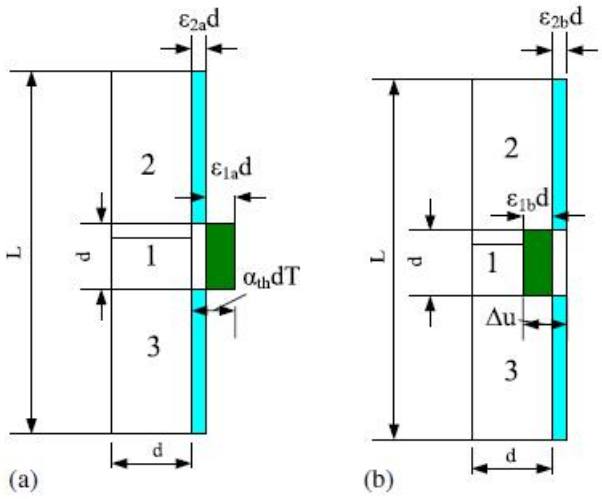

Figure 1.3-2 Schematic diagram of heating deformation of a plate [22]

In Figure 1.3-2, zone 1 is the heated zone; zone 2 and 3 are normal-temperature zones. It is assumed that the initial temperatures of zone 1, 2 and 3 is 0 , meaning before the introduction of the heat source. In the heating process it is assumed that the highest temperature of zone 1 is T and the temperature of zones 2 and 3 are constant to simplify the analysis. The free thermal expansion of zone 1 is $\alpha_{th}dT$ and that of zones 2 and 3 is zero, so zone 1 is compressed and shortened while zones 2 and 3 are pulled to lengthen [22, 23].

As a result, the constraint of zones 2 and 3, the shortening value of zone 1 is $\varepsilon_{1a}d$, i.e. $\frac{\sigma_{1a}d}{E}$, and then the final expansion value of zone 1, Δu is equal to $\alpha_{th}dT + \frac{\sigma_{1a}d}{E}$. The final expansion value of zones 2 and 3 are $\varepsilon_{2a}d$, i.e., $\frac{\sigma_{2a}d}{E}$ as shown in Figure 1.3-2(a). The final expansion value of zone 1 should be equal to that of zones 2 and 3, therefore [22, 23]:

$$\alpha_{th}dT + \frac{\sigma_{1a}d}{E} = \frac{\sigma_{2a}d}{E} \quad (1)$$

Note that α_{th} is the coefficient of thermal expansion, T maximum is the average temperature of the heated area, σ_{1a} is the compressive stress of zone 1, and σ_{2a} is the tensile stress of zones 2 and 3. The compressive force of zone 1 should be equal to the tensile force of zone 2 and 3, i.e.: [22, 23]

$$\sigma_{1a}S_1 = -\sigma_{2a}(S_{2+}S_3) \quad (2)$$

Where S_1, S_2 and S_3 are the cross-sectional areas of zones 1, 2 and 3, respectively, and $S_2 = S_3$. From Eqns. (1) and (2), we can obtain [22, 23]

$$\sigma_{1a} = -\frac{2\alpha_{th}ETS_2}{(S_{1+}2S_2)} \quad (3)$$

$$\sigma_{2a} = \frac{\alpha_{th}ETS_1}{(S_{1+}2S_2)} \quad (4)$$

The equation for the final expansion value of zone 1,Δu which is the shortening value

$$\Delta u = \frac{\alpha_{th} E T S_1}{(S_1 + 2S_2)} \quad (5)$$

After cooling, zone 1 is pulled to lengthen and zones 2 and 3 are compressed to shorten. The lengthening value of zone 1 is $\varepsilon_{1b} d$, i.e., $\frac{\sigma_{1b} d}{E}$ and then the final shortening value of zone 1, Δv is equal to $-\Delta u + \frac{\sigma_{1b} d}{E}$. The final lengthening value of zones 2 and 3 is $\varepsilon_{2b} d$, i.e. $\frac{\sigma_{2b} d}{E}$, as shown in Figure 1-7(b). The final shortening value of zone 1 should be equal to that of zones 2 and 3: [22, 23]

$$-\Delta u + \frac{\sigma_{1b} d}{E} = \frac{\sigma_{2b} d}{E} \quad (6)$$

Note that σ_{1b} is the tensile stress of zone 1 and σ_{2b} the compressive stress of zones 2 and 3. The tensile force of zone 1 should be equal to the compressive force of zones 2 and 3, i.e.: [22, 23]

$$-\sigma_{1b} S_1 = 2\sigma_{2b} S_2 \quad (7)$$

From Eqns. (6) and (7), we can obtain [22, 23]

$$\sigma_{1b} = \frac{2\Delta u E S_2}{d(S_1 + 2S_2)} \quad (8)$$

$$\sigma_{2b} = -\frac{\Delta u E S_1}{d(S_1 + 2S_2)} \quad (9)$$

Then the final shortening value of zone 1,Δv is [22, 23]

$$\Delta v = \frac{\Delta u S_1}{S_1 + 2S_2} \tag{10}$$

Substituting Eq. (5) into Eq. (10), the above equation can be expressed as follows [22, 23]

$$\Delta v = \frac{\alpha_{th} d T S_1^2}{(S_1 + 2S_2)^2} \tag{11}$$

The length of the plate is L, and its width is B. In the above equation $S_1 = d$, $S_1 + 2S_2 = L$, and the total shortening value is [22, 23]

$$\Delta B = \Delta v \frac{B}{d} = \frac{\alpha_{th} B T S_1^2}{(S_1 + 2S_2)^2} = \frac{\alpha_{th} B T d^2}{L^2} \tag{12}$$

For the bottom surface, the plate only generates elastic deformation under the TGM. If plastic deformation occurs at the bottom surface, then BM or UM play a dominant role. Therefore, longitudinal shortening value of the bottom surface is zero. According to the geometrical relationship of the deformation, as shown in Figure 1.3-3, we get [22, 23]

$$\alpha_B R - \alpha_{Br} = \Delta B \tag{13}$$

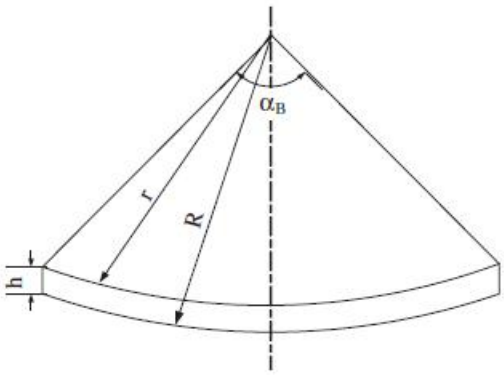

Figure 1.3-3 Analysis of angular deformation about the y-axis [22].

From the above equation, the bending angle about the y-axis can be given as [22, 23]

$$\alpha_B R = \frac{\Delta B}{R-r} = \frac{\Delta B}{h} \tag{14}$$

NB: The temperatures of the top and bottom surfaces of the LBFormed plates is given by [22, 23]:

$$T\ 0, t\ = \frac{6.92AP\sqrt{\alpha d}/\pi V}{\pi d^2 k} \tag{15}$$

Substituting Eqns. (12) and (15) into Eq. (14), the bending angle about the y-axis can be rewritten as follows [22, 23]:

$$\alpha_B = \frac{6.92AP\ \alpha_{th} B d^{\frac{1}{2}}}{\pi^{\frac{3}{2}} L^2 h (\rho c k V)^{\frac{1}{2}}} \tag{21}$$

The analytical model of the TGM indicates the plate bends not only about the x-axis but also about the y-axis. This analytical model allows for the results simulation of the bending angle about the y-axis which may describe more fully the deformation of a plate, which is helpful in high-precision laser forming [22, 23].

1.4 The Influence of Tool Rotation and Laser Surface Texturing (LST) On Formability, In Single Point Incremental Forming (SPIF)

Single point incremental forming (SPIF) is a die-less sheet metal forming process in which blank sheets are peripherally clamped and then locally deformed using a generic hemispherical ended tool moving along a predefined trajectory [24]. These local deformations accumulate and finally achieve the desired component shapes. Compared to the conventional sheet metal forming process, such as deep drawing, SPIF has greater process flexibility and enhanced blank formability due to the non-dependence of specific product shape and the nature of local deformation, respectively [24–27]. Additionally, since the requirement of forming force in SPIF is lower compared to conventional forming, this allows the usage of smaller and more mobile machines. Because of these advantages, SPIF satisfies the requirement of decreasing lead time and costs in manufacturing process and further carries out the reduction of energy consumption and environmental pollution [28 & 29]. However, it should be noted that the forming time in SPIF is much higher than those in conventional forming. According to the mentioned advantages and limits of SPIF, this process is particularly suitable to small batch production and prototypes in the automotive, aerospace and biomedical manufacturing sectors [30 & 31].

With the growth application of lightweight alloys, SPIF is inevitable to encounter the challenges in forming these alloys. The maximum formable wall angle for different series of aluminium alloys is about 60-70°C for blank thicknesses ranging from 0.8 to

1.5mm [24 to 31]. Titanium and magnesium alloys with pre-hardening or heat treatment are regarded as hard-to-form sheet metals, in terms of their very poor formability in room temperature [32 to 34]. Multi-pass single point incremental forming (MSPIF) was developed to increase the maximum formable wall angle in SPIF, by forming multiple intermediate shapes before obtaining the final component [35 to 38]. MSPIF however, makes the forming time even longer than the regular SPIF, and brings difficulties in determining the number and type of intermediate shapes. As a consequence, a few studies have been done to elevate the room temperature to warm or hot conditions by various methods in order to enhance the material formability. These heat-assisted SPIF methods can be simply divided into six categories based on different types of heat sources as described in Table1.4-1.

Table 1.4-1 Heat-assisted SPIF methods [38].

Heat-assisted methods	Principle	Flexibility	Equipment cost	Special lubricant	Tooling wear	Local dynamic heating
I: Hot air blower [17]	Convection	Fair	Fair	No	Low	No
II: Laser heating [18,19]	Radiation	Fair	High	No	Low	Yes
III: Heater band [20]	Conduction	Low	Fair	No	Low	No
IV: Electric heating [21–24]	Joule heat	Fair	Fair	Yes	High	Yes
V: Frictional heating [25–27]	Friction heat	High	Low	No	Fair	Yes
VI: Combination [28]	Joule heat+friction heat	Low	Fair	No	Fair	Yes

Different heat assisted SPIF methods have their pros and cons, as summarised in Table1.4-1. Among those, frictional heating (Category V) generated by increasing tool rotation speed, i.e. increasing the relative speed between forming tool and workpiece, is a good option to bring blank sheets into warm or hot conditions without sacrificing process flexibility or adding process complexity. Otsu et al. [39] employed tool rotation speed in a range of $2000-\ 10{,}000\ rpm$ to study formability improvement in forming AA5052- H34 aluminium alloy sheet with a thickness of 0.5 mm into pyramid shape.

The findings showed that the material formability was dramatically improved due to temperature rising and dynamic recrystallization when tool rotation speed was greater than $7000rpm$. Similarly, a significant formability enhancement at forming AZ31, AZ61 and AZ80 magnesium alloy sheets was achieved at a tool rotation speed of 8000rpm [40].

Buffa et al. [41] formed AA1050-O, AA1050-H24, and AA6082-T6 aluminium alloy sheets by elevated tool rotation speeds of up to $10{,}000rpm$. With this approach an increase of material formability was observed and formability limit curves were developed at the varying utilized rotational speeds. There are also few research works which are focused on finding the influence of tool rotation at a relatively low speed $200\ to\ 2000rpm$ on the forming forces and surface finish of formed components. Durante et al. [42] indicated that friction decreases with the increase of tool rotation speed which are ranging from $0\ to\ 800rpm$ through a straight groove test. Furthermore a reduction in surface roughness by up to 10% when internal surface of the components formed at 200 rpm and 600rpm is measured was observed.

Hamilton and Jeswiet [43] investigated the external surface roughness (orange peel effect), thickness distribution and sectional microstructure in SPIF at high feed rates $(5080-8890\ mm/min)$ tool rotation speeds of between $400\ to\ 2000\ rpm$. However, the mechanisms behind the effect of tool rotation speed for both low and high ranges on material formability and require more studies to fill in the gaps that currently exists in the literature. Figure 1.4-1 is a schematic of laser surface textures for a SIFP process

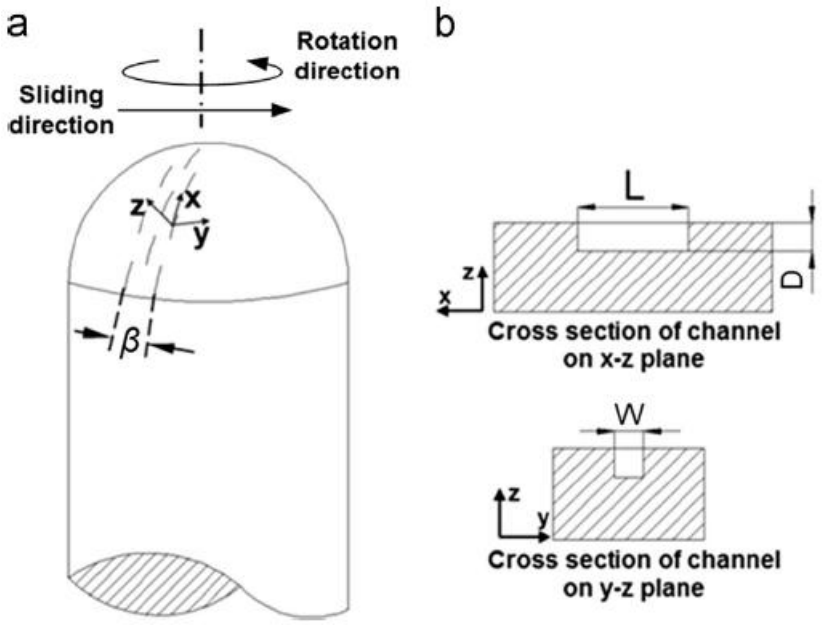

Figure 1.4-1 Schematic of laser surface textures: (a) distribution pattern of surface textures (θ=10.56°) and (b) desired bottom shape of textures (length (L) × width (W) × depth (D) = 200 μm ×25 μm × 25 μm) [47].

- **Laser forming forces**

Force measurements are carried out not only to monitor the approach of failure, but also to study the mechanisms of SPIF [44 to 47]. Force components normally imposed onto the blank sheet in the X, Y and Z directions are as shown in Figure 1.4-2, and are measured by the six-component dynamometer.

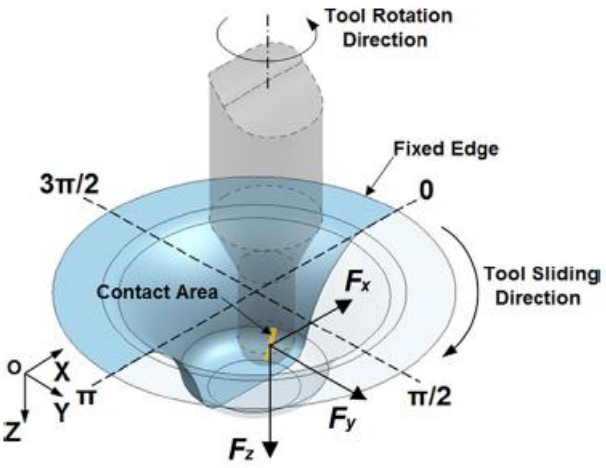

Figure 1.4-2 Schematic representation of the forming forces in SPIF [48].

Figure 1.4-2 illustrates the force curves of Fz and Fx throughout the forming process with typical tool rotation speeds. According to a study done in the literature [48], the forming tool is indented into the blank sheet, Fz force is instantaneously introduced and then gradually increased until the force peak is reached. This phenomenon can be mainly attributed to the bending near the edge of the fixture and the incomplete contact interface between the tool and sheet at the first several contours. After the peak, it can be seen that Fz force monotonically decreases until material failure occurred. This is because four competing factors are involved simultaneously. Material thinning and temperature increase induced by frictional heat generation tend to reduce the required forming forces. Material strain-hardening and increased wall angle of the design shape tend to increase the forming forces. Consequently, material thinning and temperature increase dominated after reaching peak values, and caused Fz force to decrease. The variation of Fx force followed a trend which was analogous to a sine curve and its value depended on the position of the forming tool within one contour.

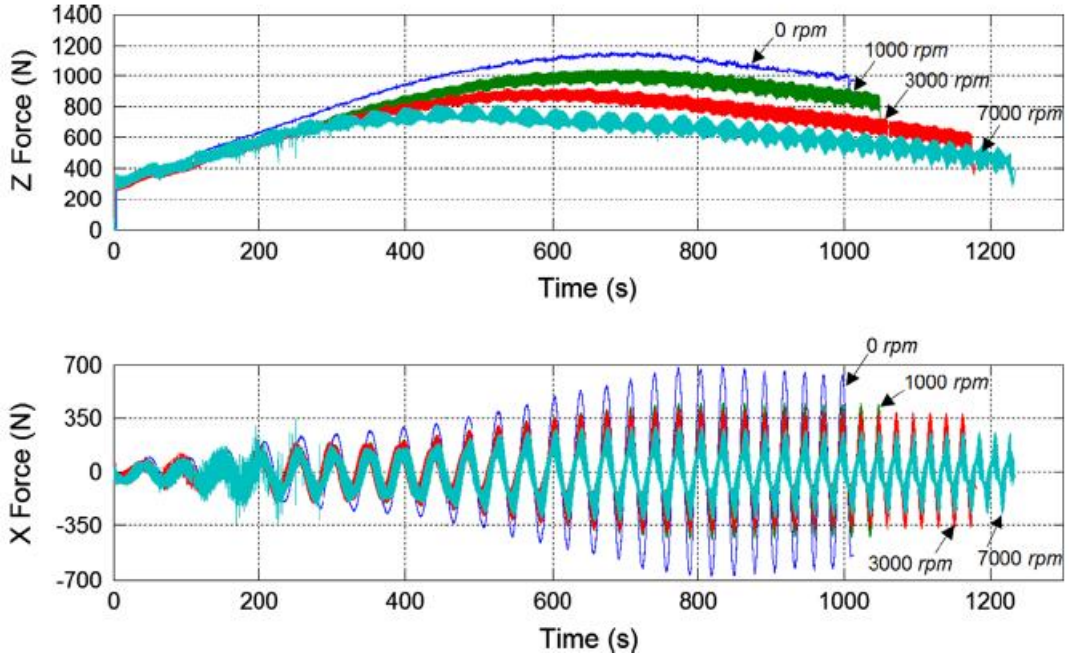

Figure 1.4-3 Forming force curves at different tool rotation speeds [48]

When the tool is subjected to a specific rotation speed, it was noted that the general trend in the force curve did not change refer to Figure 1.4-3. However, as tool rotation speed is elevated, the values of both Fz and Fx forces decreases. Another observation was that the peak forces were reached earlier with higher tool rotation speeds. These different force evolution behaviours are determined by the combined effect of friction and heat. It was found in [42] that the friction coefficient decreased from 0.19 to 0.06 as tool rotation speed increased from 0 to $800rpm$ by using a groove test. Therefore, the force reduction below $1000\ rpm$ was mainly attributed to the decrease of friction because material softening did not occur since the temperature was still less than $100°C$. On the other hand, tool rotation speeds over $1000rpm$ generated more frictional heat which was sufficient to soften the material. Particularly, the detected maximum temperatures at $3000\ rpm$ and $7000\ rpm$ were around $175°C$ and $220\ °C$, respectively as shown in Figure 1.4-4. Due to significant material softening above$150°C$, it is concluded that the thermal effect gradually becomes the dominant reason for the force reduction as the tool rotation speed increases.

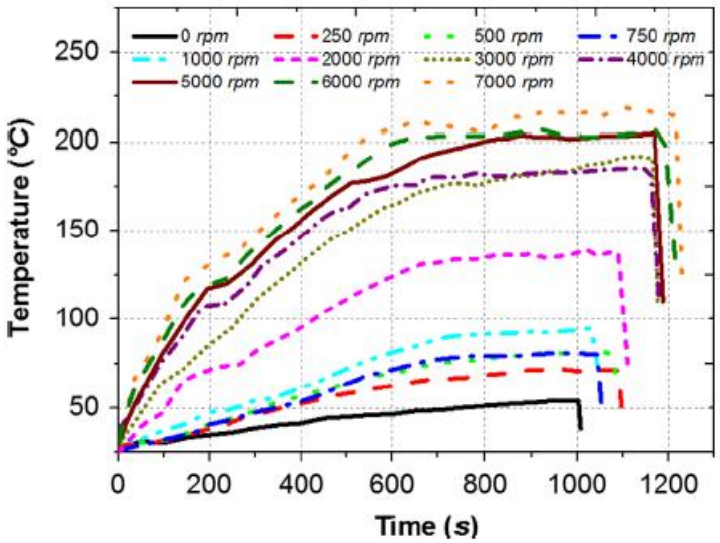

Figure 1.4-4 Temperature trends at different tool rotation speeds [48]

Figure 1.4-5 shows the obtained stress versus strain relations of AA5052- H32 at different temperatures

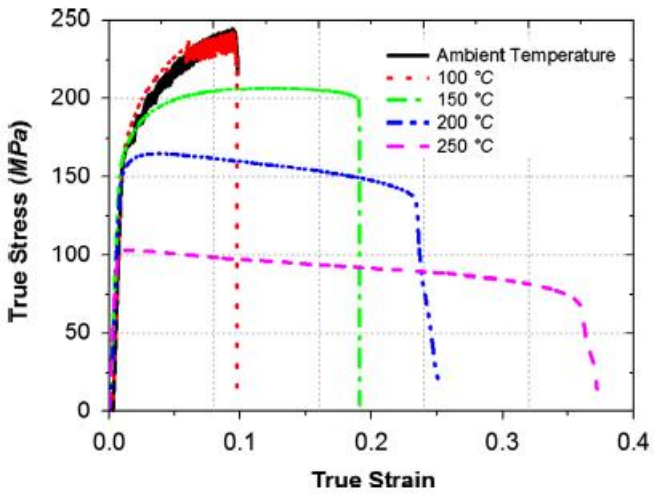

Figure 1.4-5 Stress vs Strain Relation of AA5052-H32 at different temperatures [48]

It can be seen that no obvious material softening occurred when rising ambient temperature up to100 □ . Subsequently, a decrease of flow stress was observed when the temperature increased from $100\ to\ 150$ □ , which implied the material started to get soft. Furthermore, it is important to note that the phenomenon of dynamic recrystallization was detected from the stress and strain curves at temperatures of 200 □ $and\ 250$ □ and the material ductility had been further improved [48].

1.5 Mild Steel in the Industry

Mild Steel was preferred for this research investigation because it is one of the most common steels and one of the least expensive steels available. It is weldable, very durable (although it has a generally high corrosion rate when compared to other metals), it is relatively hard and is easily annealed. Figure1.5-1 shows the relationship

between carbon content and maximum obtainable hardness in Carbon in alloy steels [49].

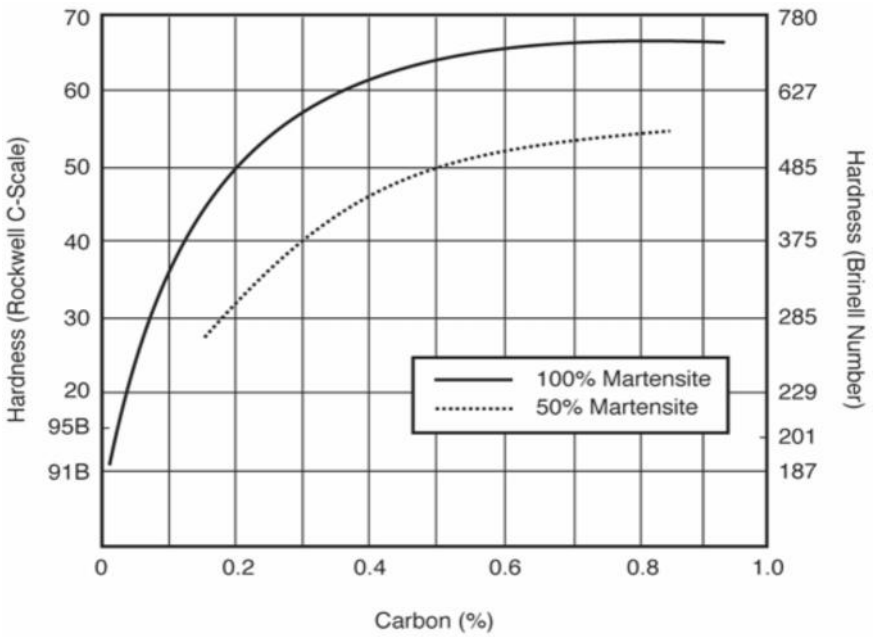

Figure 1.5-1 The Hardness vs Carbon in Alloy Steels [49]

When it comes to design, mild steel has the following strengths [49]:

i. Reasonable strength-to-weight ratio & High stiffness-to-weight ratio
ii. Good strength with high toughness
iii. Very cheap, easy to shape, and easy to weld
iv. Easy to recycle

The following are the weaknesses that are associated with mild steel:

i. Poor electrical and thermal conductivity when compared to copper

Typical products made from mild steel are:

i. Large structures - bridges, buildings, oil rigs
ii. Car body panels, trains
iii. Machine tools

iv. Pressure vessels

v. Nails

- **Mild Steel-AISI 1008**

AISI 1008 carbon steel has excellent weldability, which includes butt, spot and fusion, as well as brazeability. Table 1.5-1 shows the chemical composition of AISI 1008 carbon steel [50].

Table 1.5-1 Chemical Composition of AISI 1008 Carbon Steel [50]

Element	Content (%)
Iron, Fe	99.31-99.7 %
Manganese, Mn	0.30-0.50 %
Carbon, C	0.10 %
Sulfur, S	0.050 %
Phosphorous, P	0.040 %

The physical properties of AISI 1008 carbo steel are; density at (composition 0.06%C, 038% Mn, 0.01% Si, annealed at 925^{o}C is 7.872 g/cm^{3} (Metric) or 0.2844 lb/in$^{3.}$

Table 1.5-2 shows the mechanical properties of cold drawn AISI 1008 carbon steel.

Table 1.5-2 Mechanical properties of cold drawn AISI 1008 carbon steel [50]

Properties	Metric	Imperial
Tensile strength	340 MPa	49300 psi
Yield strength (depending on temper)	285 MPa	41300 psi
Elastic modulus	190-210 Gpa	27557-30458 ksi
Bulk modulus (typical for steel)	200 GPa	29000 ksi
Shear modulus (typical for steel)	80.0 GPa	11600 ksi
Poisson's ratio	0.27-0.30	0.27-0.30
Elongation at break (in 50 mm)	20%	20%
Reduction of area	45%	45%
Hardness, Brinell	95	95
Hardness, Knoop (converted from Brinell hardness)	113	113
Hardness, Rockwell B (converted from Brinell hardness)	55	55
Hardness, Vickers (converted from Brinell hardness)	98	98
Machinability (based on AISI 1212 steel as 100 machinability) The machinability of group I bar, rod, and wire products can be improved by cold drawing)	55	55

Table 1.5-3 shows the thermal properties of AISI 1008 carbon steel.

Table 1.5-3 Thermal properties of AISI 1008 carbon steel [50]

Properties	Metric	Imperial
Thermal expansion co-efficient (@0.000-100°C/32-212°F)	12.6 µm/m°C	7 µin/in°F
Thermal conductivity (composition of 0.06% C, 0.4% Mn; 0°C)	65.2 W/mK	452 BTU in/hr.ft².°F

Low carbon steel consists mainly of ferrite and pearlite. It is iron in its pure form, ferrite or α-iron has a body-centred-cubic crystal structure, which can undergo three phase changes when heated sufficiently. Iron remains ferrite up to 912 °C and with increased temperature it will exist as austenite or γ-iron with a face-centred-cubic crystal structure. From 1394 °C to 1538 °C it again exists as ferrite and becomes liquid when the temperature is increased [9]. Each phase change brings a transformation in the crystal structure as shown in the iron-carbon equilibrium diagram indicated in Figure

1.5-1. The 0.06% carbon in Figure 1.5-1 is marked with a red line, this indicates how the microstructure of AISI 1008 will change with a change in temperature

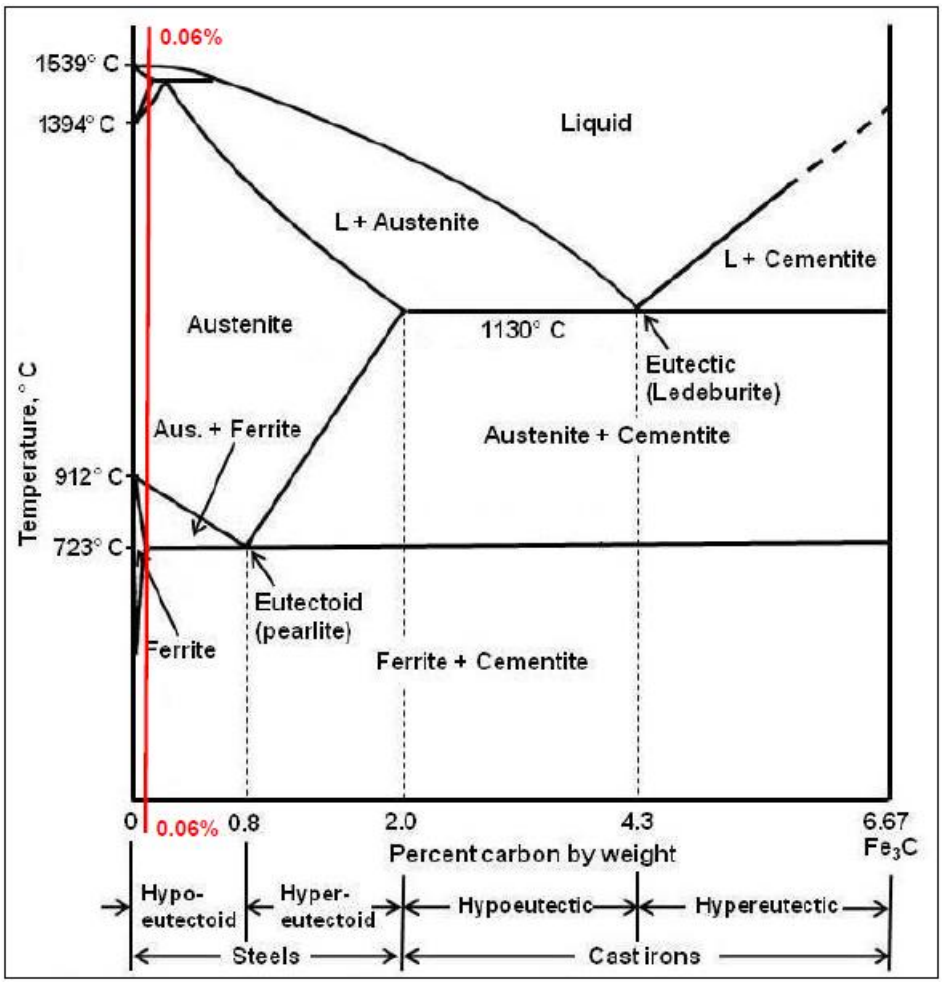

Figure 1.5-1 Iron-carbon equilibrium diagram indicating how the microstructure of the steel will change with a change in temperature [52]

A micrograph of an AISI 1008 steel at 50 micrometres after polishing and etching is shown in Figure 1.5-2 [52]. The micrograph which was taken along the rolling direction of the material, clearly shows the ferrite indicated by the grey constituent and the pearlite indicated by the black constituent. The micrograph was taken along the rolling direction of the material [52].

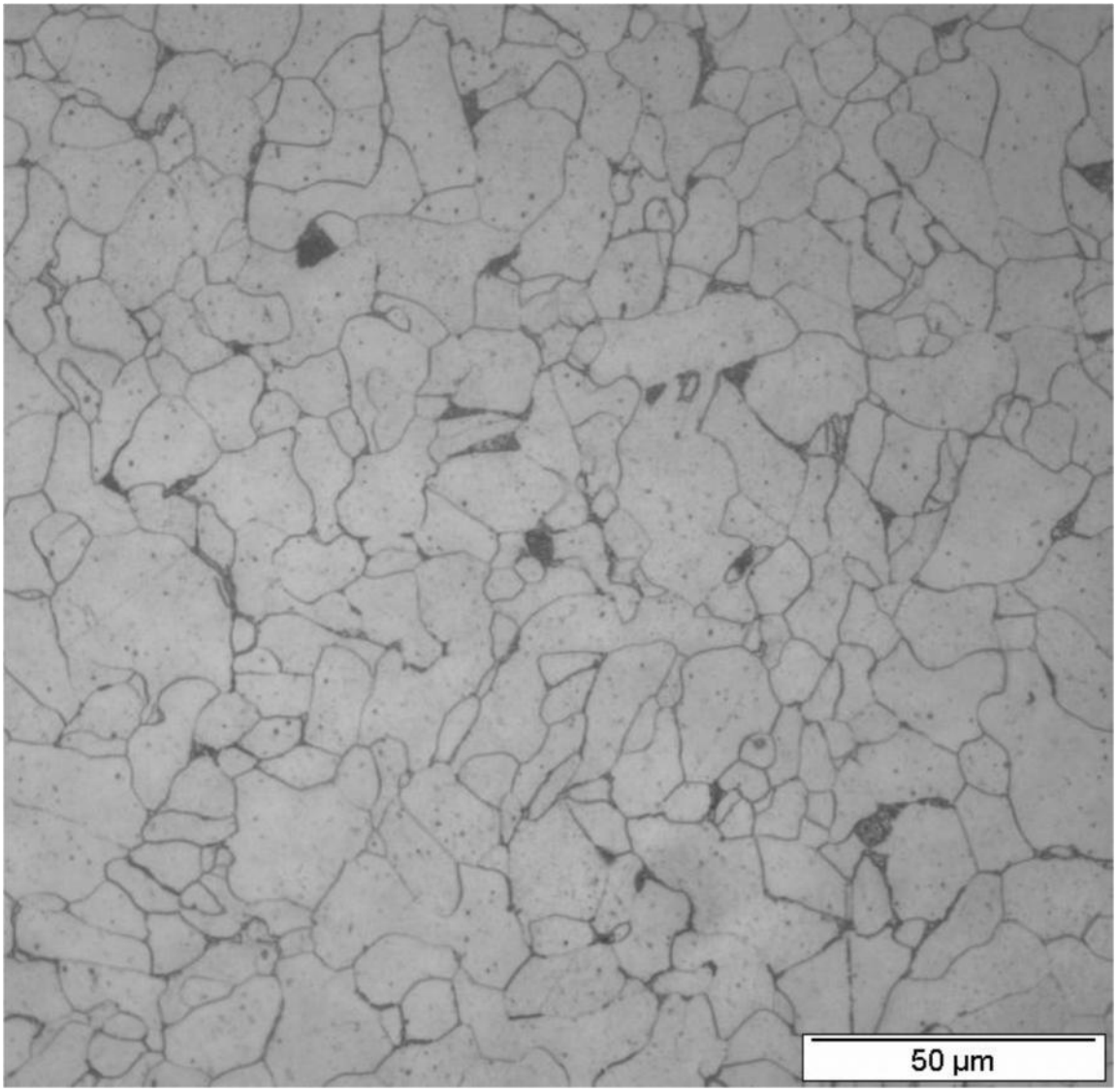

Figure 1.5-2 Micrograph indicating the ferrite in grey constituents and pearlite in black constituents [52]

1.6 Design of Experiments (DoE)

DoE is one of the many problem-solving quality tools that can be used for various investigations such as finding the significant parameters (known as factors) with various possible settings (known as levels) in a process [53]. When the purpose of the investigation is an optimisation, a critical concern is the interaction between the different parameters and how they affect the desired outcome.

Many industries use this tool to stay competitive worldwide by designing robust products as well as improving quality and reliability of a product. By using strategically designed and statistically performed experiments, it is possible to study the effects of several variables at one time, and to study inter-relationships and interactions. The data obtained from the DoE, can help propose a strategy to apply and the required performance optimisation of a process [53].

DoE techniques which allow for the study of parametric effects, with a reduced number of trials, are known as fractional factorial designs. There is a wide range of fractional factorial DoE methods, such as: Taguchi, Plackett–Burman, Box–Behnken, Doehlert and D-Optimal to name only a few [54]. The three primary functions associated with DoE's are screening, optimisation and robustness.

1.7 Response Surface Methodology (RSM)

Response surface methodology (RSM) also known as a meta-model, is a collection of mathematical and statistical techniques for empirical model building. It creates a multi-dimensional contour plot, which is used to create relationships between input parameters (factors) and a response as shown in Figure 1.7-1. By careful design of *experiments*, the objective is to optimize a *response* (output variable) which is influenced by several *independent variables* (input variables). An experiment is a series of tests, called *runs*, in which changes are made in the input variables in order to identify the reasons for changes in the output response.

Originally, RSM was developed to model experimental responses and then migrated into the modelling of numerical experiments [54]. The difference is in the type of error generated by the response. In physical experiments, inaccuracy can be resulted due to measurement errors, while in computer experiments, numerical noise is a result of the incomplete convergence of iterative processes, round-off errors, or the discrete representation of continuous physical phenomena [54]. In RSM, errors are assumed to be random when factors are adjusted.

The surfaces are formulated using advanced algorithms such as: Shepard, Kriging, Gaussian Processes, Radial Basis Functions, and Neural Networks. Once the surface has been created, generating solutions from it is as simple as reading the response value that correlates to the desired inputs. RSM is typically employed for optimisation purposes and to reduce experimental costs and time. By using the RSM to establish the relationships between factors and responses, the response surface can effectively

be utilised to ‘convert’ a set of fractional factorial results into a set of ‘virtual’ results with a much larger sample size. For example, the 27 results of a Taguchi L_{27} orthogonal array can be converted into infinitely many ‘virtual’ results, with infinitely many levels between the original levels used in the experiments.

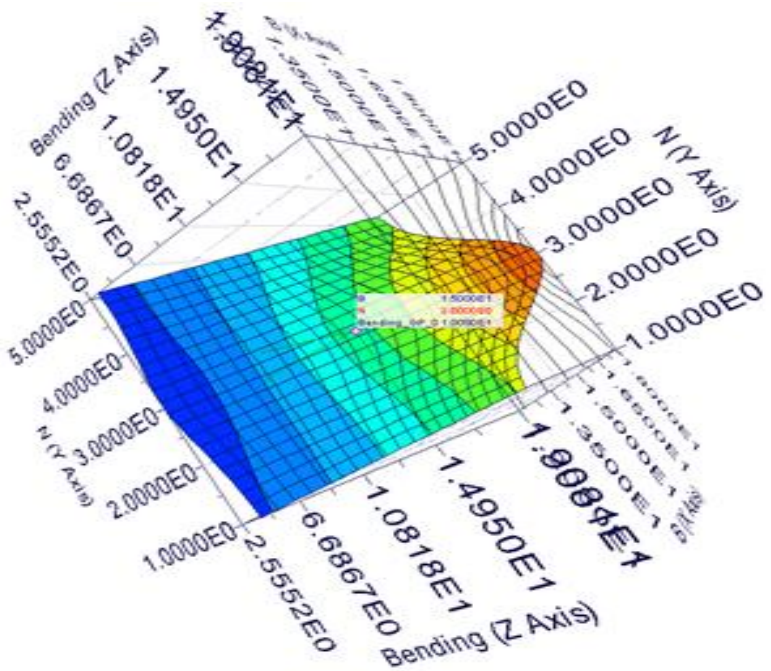

Figure 1.7-1 Sample response surface [54]

The increase in sample size satisfies the Central Limit Theorem (CLT) and ultimately the requirements of analysis of variance (ANOVA) [54]. An important consideration is that the quality of the results depends entirely on the goodness-of-fit of the response surface to the experimental data. Therefore, RSM technique should be used with caution. The residuals of the response surface must be analysed critically, because when the surface does not fit the experimental data with a high level of accuracy, the results generated will not be reliable.

1.8 Objectives

LBF is a fast forming process which requires no tooling, but poor material surface quality which resulted from failure in obtaining optimum bending is what motivated this research. A different approach which incorporates DOE is seen to have the ability to deliver improved results to LBF process and yet to save cost, and time.

This section provides an itemized list of the primary objectives of this research investigation in accordance with the requirements of the University of the Witwatersrand.

1. Optimise laser parameters to get the results that will maximise the bending with less material surface damage on AISI 1008-mild steel.
2. Measure and quantify obtained results.
3. Assess the impact of general process parameters i.e. parameters and levels versus the results.

1.9 Methodology

The research was focused on optimising LBF process parameters to achieve maximum bending with good surface finishing. A DOE was used for the selection of LBF process parameters. The parameters that are generated through the DOE are used as input parameters for the LBF process. The material bending from the LBFormed samples was measured in the workshop with tools that are described in

detail in Chapter 2. The material bending is a critical part of LBF process because of its relation to material surface quality. Chapter 3 is the LBF procedure and the bending measurement procedure.

LBFormed samples are further analysed for material property variations using the microscope. Furthermore, the hardness testing is also carried through to determine if LBF process parameters have any effects on material hardness. The procedures and the results for microscopy and microanalysis, together with micro-hardness are available in Chapter 4. The results generated by the DOE as output parameters are used to feed the RSM as input parameters to generate virtual results that are compared to experimental results. The RSM is covered in Chapter 5, while chapter 6 is the concluding chapter.

Chapter 2

Experimental Tools

This chapter gives a general overview of this research together with the experimental optimisation and experimental procedures used in investigation.

2.1 Introduction

The samples are AISI 1008 mild steel and this research is focused on optimising LBF process parameters to achieve maximum bending with excellent surface finishing. The approach taken to optimise LBF process parameters involved the use of the DOE tool. This means identifying the most suitable DOE tool to optimise critical LBF input process parameters and levels, which are discussed in this research. Details of the laser machine used to LBF the samples are shared. Experimental facilities and detailed workshop experimental procedures used to investigate LBF parameter optimisation is presented in this Chapter.

LBFormed samples were further analysed using the microscopy and microanalysis unit (MMU) at the School of Microbiology, Wits University. The details of the instruments used are presented in this chapter. A further analysis was done using the RSM to compare the results with the previous analyses. Lastly, the hardness test was done on LBF samples to see variations in samples formed using different laser forming parameters which are presented.

2.2 Experimental Facilities and Instruments

The Taguchi OA selection matrix in Table 2.3-1 was used to select LBF process input parameters that are used to machine 200 x 50 x 3 mm^3 AISI 1008 mild steel samples, which are experimental samples for this investigation. The Taguchi OA output parameters are then used as LBF input parameters, where samples machined using these parameters were categorised into three levels. Levels 1, 2 and 3 categories refer to low, medium and high LBF parameter settings respectively. The quantities that are associated with each level for a specific parameter in the LBF process are also presented in Table 2.3-1 of section 2.3-1 of this report.

This categorisation is aimed at deriving the parameters and levels that will yield the desired results and further check consistency of the outcomes using the RSM modeFRONTIER. The LBF machine that is used for machining the experimental samples is the 4.4 kW Nd: YAG laser system – Rofin DY 044, which is at the National Laser Centre (NLC), Council for Scientific and Industrial Research (CSIR), Pretoria.

The procedure followed to machine the 200 x 50 x 3 mm^3 AISI 1008 mild steel experimental samples is similar to the one that is presented in Figure 1-1 (Chapter 1), where samples are secured and clamped during laser forming process.

Figure 2.2-1 Figure 4 1 A 4.4 kW Nd: YAG laser system – Rofin DY 044

Each sample is identically machined by passing a laser light at equal parallel spacing, set at 10 mm apart along the width of the surface area of each sample. The distance between these spacing (laser scan track) are set such that, the laser heated zone does not overlap with the next laser scan track. This is to avoid corrupting the detail of the neighbouring scan track and ensuring accuracy of the results. Figure 2.2-2 is a presentation of LBFormed experimental samples that are machined using levels 1, 2 and 3 quantities for the five mentioned LBF process parameters.

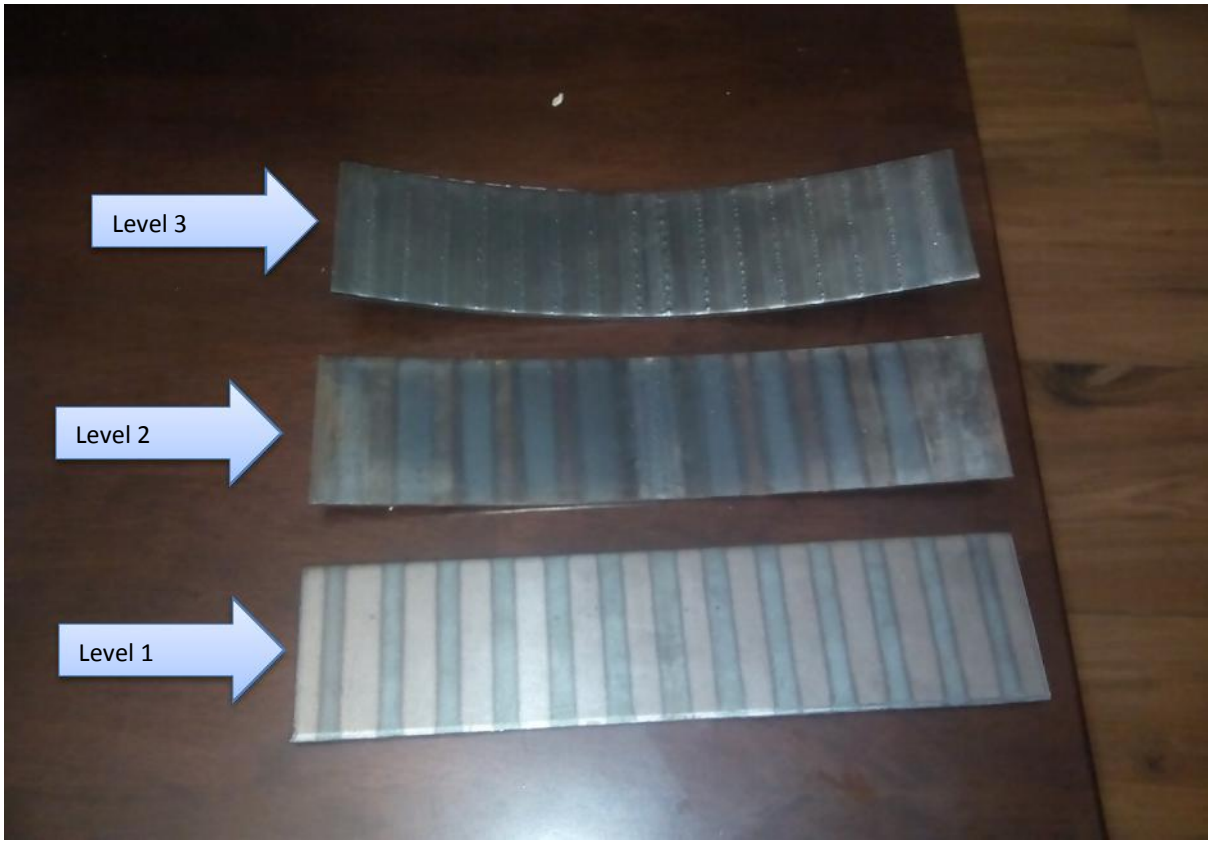

Figure 2.2-2 A 200 x 50 x 3 mm3 mild steel -AISI 1008 LBF Samples

Post laser forming analysis of the LBFormed samples from the CSIR were carried out at School of Mechanical Engineering workshop, and the Microscopy and Microanalysis Unit (MMU) of Wits University. The analysis done on LBFormed samples involved measuring of sample bending, performing microanalysis, hardness testing, and RSM on laser formed samples. The workshop tools that were used to measure the bending were the dial indicator with magnetic stand, G-clamp, steel bar, and a 300 mm steel ruler. The listed instruments are presented in Figure 2.2-3. Micro hardness testing was done on the LBFormed samples and the details are discussed under micro hardness test section of this Chapter.

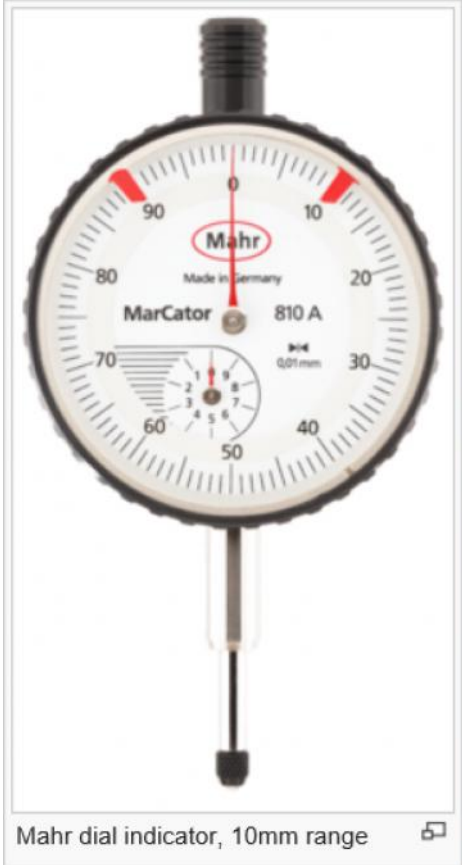

Mahr Dial Indicator (a)

30 Centimetre steel Ruler (b)

Square Steel Bar (c)

G-Clamp (d)

Figure 2.2-3 Mahr Dial Indicator, 30 Centimetre (cm) Steel Ruler, Square Steel Bar, and G-Clamp

Microanalysis was done on LBFormed samples for further investigation and verification of the results generated from the LBF process parameters. The 200 x 50 x 3 mm^3 mild steel–AISI 1008 LBFormed samples had to be cut into smaller sizes of 65 x 20 x 3 mm^3 in order to fit on the microscope stand during microanalysis. Figure 2.2-4 presents the schematics of how the smaller pieces used for microanalysis were cut from the original laser formed samples.

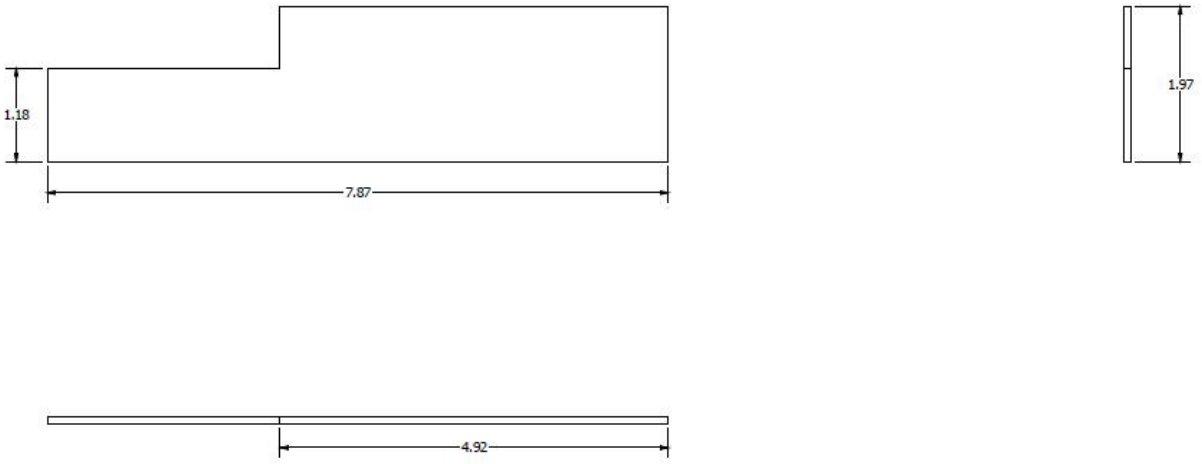

Figure 2.2-4 A 200 x 50 x 3 mm3 mild steel -AISI 1008 LBF Samples Schematic Sectioned

The NSM V horizontal milling machine from the school of mechanical engineering was used to cut the 200 x 50 x 3 mm^3 AISI 1008 mild steel laser formed samples to 65 x 20 x 3 mm^3 that are able to fit on the stage of the microscope. NSM V horizontal milling machine is represented in Figure 2.2-5 and Figure 2.2-6 is a representation of the smaller cut pieces of 65 x 20 x 3 mm^3.

Figure 2.2-5 The NSM-V horizontal milling machine

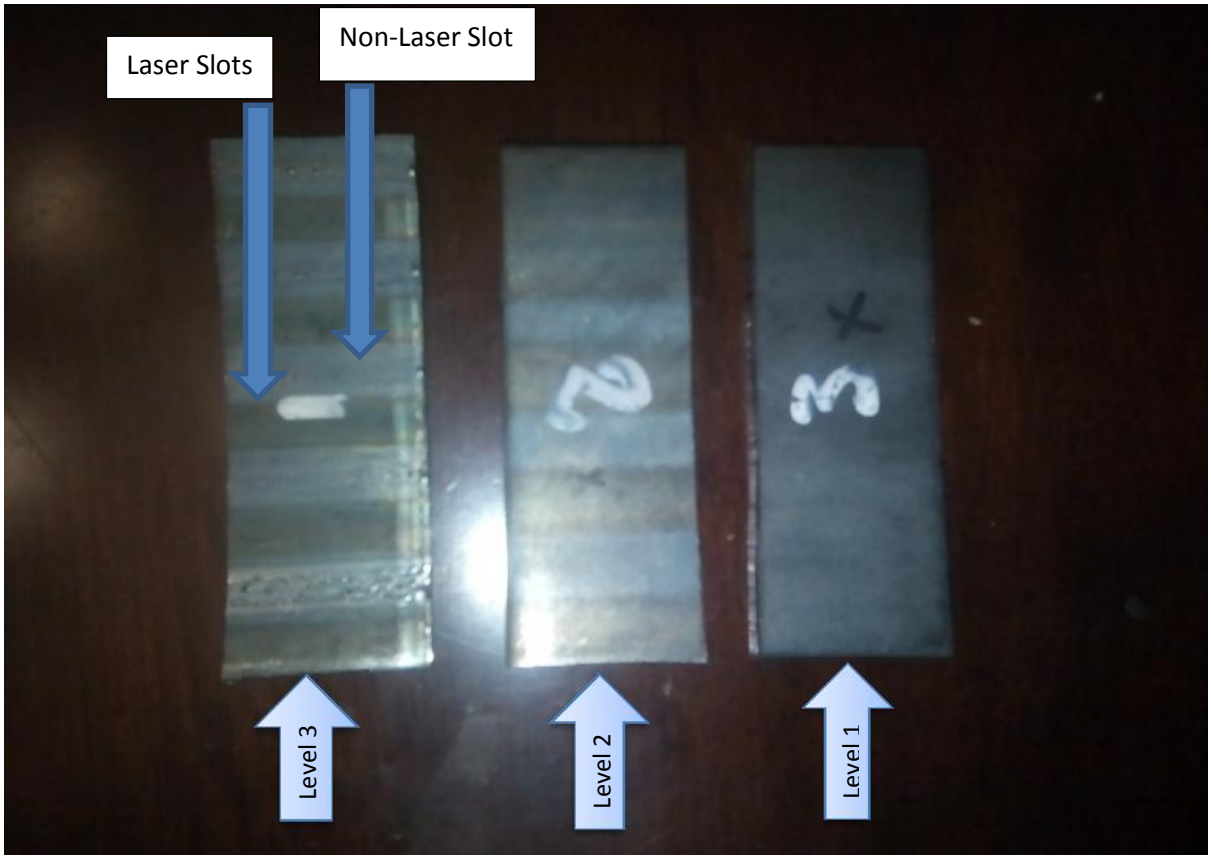

Figure 2.2-6 Smaller cut sample pieces (65 x 20 x 3 mm3 AISI 1008 Mild Steel)

The following discussions are around the equipment and tools that were used during the MMU, HV Test, the Taguchi DOE, and the RSM modeFRONTIER for the analysis of LBFormed samples.

As already mentioned, the MMU was used to analyse the surface roughness of the LBFormed samples. The instruments used for the analysis of the 65 x 20 x 3 mm^3 AISI 1008 mild steel are the Confocal and the Quanta FEG-SEM microscopes. Figure 2.2-7 presents the Leica TCP SP2 SE Confocal microscope, whilst Figure 2.2-8 presents the FEI Quanta FEG-SEM microscope. The details of the MMU are in Chapter 4 of this report.

Figure 2.2-7 Leica TCP SP2 SE Confocal microscope

Figure 2.2-8 FEI Quanta FEG-SEM microscope

LBFormed samples were further analysed for Vickers Hardness (HV) Test, to determine the influence that the three laser categories/levels have on the LBF parameters, during LBF of the samples. The Future Tech FM-700 micro-hardness tester from the Wits School of Chemical and Metallurgical Engineering was used to perform HV Test on LBFormed samples. Figure 2.2-9 presents the Future Tech FM-700 micro-hardness tester. The HV Test was done on a number of points on the sample in both the laser track and non-laser track.

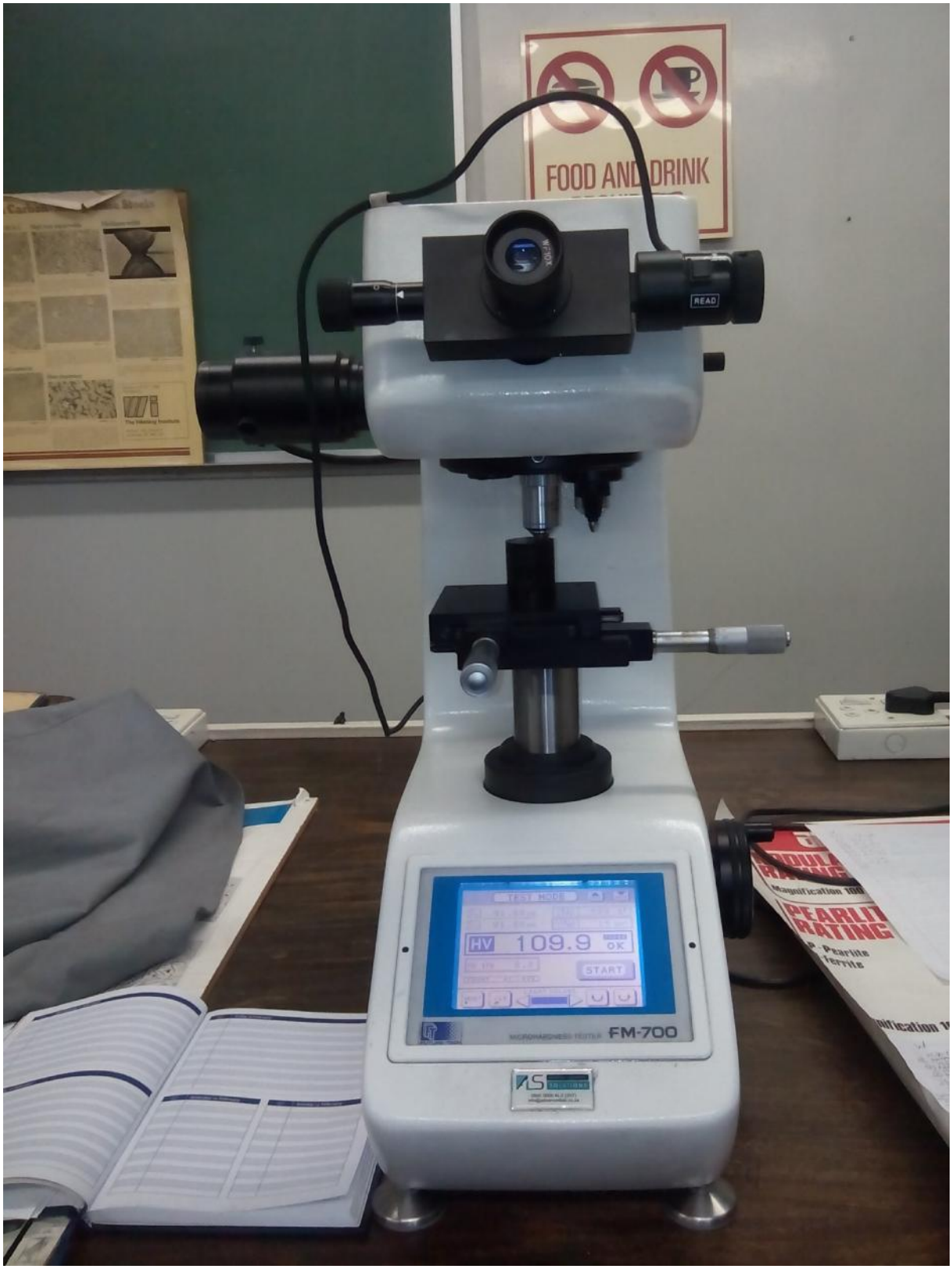

Figure 2.2-9 Future Tech FM-700 micro-hardness tester

2.3 Experimental Tools

2.3.1 The Taguchi Method (DOE)

This is a robust design philosophy, developed by Genichi Taguchi in the late 1940s [55]. It focuses on enhancing product quality while simultaneously minimising the expenditure of resources. The Taguchi Method differs from regular quality engineering practices since it focuses on building the quality into the product and processes, rather than the usual approach which relies on inspection [55]. Taguchi developed his philosophy based on the observation that 85% of poor quality on products is attributable to the manufacturing process and only 15% to the worker. Taguchi concluded that the product design and production process, must be so robust that it is immune to the influence of uncontrollable environmental factors. He also came to the conclusion that quality is directly related to the deviation of a design parameter from the target value, rather than its conformance to some fixed specifications. Therefore, his philosophy focuses on determining manufacturing processes that meet the target value of a response with little deviation.

The Taguchi Method is chosen for this research because it is the most common, versatile, and robust design technique which also accommodates response optimisation. An advantage of the Taguchi Method is that there are many DOE sequences readily available which can be used to analyse multiple factors and levels, while some DoE methods are limited to only two levels.

In order to assess product quality and the process parameters which are affecting it, Taguchi constructed DOE tables known as Orthogonal Arrays (OA). A researcher has to first determine the number of factors to inspect in a system, as well as the number of levels for each factor. Thereafter, the OA which best suits research requirements can be decided. The nomenclature for these orthogonal arrays is *LN* where *L* indicates a Taguchi orthogonal array and *N* refers to the number of experiments required to fulfil the chosen OA

The laser power, beam diameter, scan velocity, number of scans, and cooling flow are the five LBF input variables used for the DOE in this investigation. Three levels were selected for each of these LBF input variables according to three LBF process parameters discussed i.e. level 1, 2, and LBF parameters. This information allowed for a construction of an orthogonal array selection matrix to decide the DoE sequence to use. Table 2.3-1 shows the Taguchi orthogonal array selection matrix for the data used in the experiment.

Table 2.3-1 Taguchi Orthogonal Array Selection Matrix

Factor	Description	Levels		
		1	2	3
P	Laser power (W)	1800	2400	3600
B	Beam diameter (mm)	12	15	18
V	Scan Velocity (m/sec)	0,06	0,08	0,2
N	Number of scan tracks	1	3	5
C	Cooling flow (l/min)	5	10	15

This means by using the Taguchi Method where there are five parameters under these parameters and three levels, to establish the DoE, only 27 (5x3!)-3 samples will be assessed, rather than the 729 samples that would have had to be assessed for a full

factorial DoE see Table 2.3-2. This amounts to a 27x reduction in experimental trials and results which in theory draw the same conclusions.

Table 2.3-2 is the DoE sequence for the *L*27 orthogonal array based on the orthogonal array selection matrix.

Table 2.3-2 Taguchi L27 orthogonal array DOE used experimental parameter optimisation

Run #	Factors (Inputs)				
	P (W)	B (mm)	V (m/s)	N	C (l/min)
1	1800	12	0,06	1	5
2	1800	12	0,06	3	10
3	1800	12	0,06	5	15
4	2400	12	0,08	1	5
5	2400	12	0,08	3	10
6	2400	12	0,08	5	15
7	3600	12	0,2	1	5
8	3600	12	0,2	3	10
9	3600	12	0,2	5	15
10	1800	15	0,08	1	5
11	1800	15	0,08	3	10
12	1800	15	0,08	5	15
13	2400	15	0,2	1	5
14	2400	15	0,2	3	10
15	2400	15	0,2	5	15
16	3600	15	0,06	1	5
17	3600	15	0,06	3	10
18	3600	15	0,06	5	15
19	1800	18	0,2	1	5
20	1800	18	0,2	3	10
21	1800	18	0,2	5	15
22	2400	18	0,06	1	5
23	2400	18	0,06	3	10
24	2400	18	0,06	5	15
25	3600	18	0,08	1	5
26	3600	18	0,08	3	10
27	3600	18	0,08	5	15

2.3.2 ModeFRONTIER

It is highlighted in section 2.1 that the DoE is a tool that is used for selecting LBF process input parameters for LBF of the 200 x 50 x 3 mm^3 AISI 1008 mild steel samples for the investigation. The DoE output parameters are also used as input parameters to the RSM, to interpolate experimental output data. The RSM that has been selected is modeFRONTIER because of its available algorithms and their ability to interpolate input combinations that are derived from the DOE. modeFRONTIER enable the execution of complex chains of design optimization, innovative algorithms to determine the set of best possible solutions combining opposing objectives, and post-processing tools built in the model allows the user to perform sophisticated statistical analysis, data visualization and decision making [54]. modeFRONTIER assist in deriving the selection of the best sample population from those which are derived from the DOE. At the end of this research investigation, conclusions are drawn simulated from experimental results.

2.4 Conclusion

The tools and experimental facilities used in this investigation are presented. The presentation included the description and the purpose of each tool for a specific task. The detail procedures are presented in the Chapters that will follow.

Chapter 3

Laser Forming Process and Material Bending Measurement

This chapter contains the workshop procedural work that was done to study the sample bending LBF process of the 200 x 50 x 3 mm^3 AISI 1008 mild steel samples. A step by step method, tools, and the equipment used in the workshop for the material bending measurement are highlighted in this section.

3.1 Laser Beam Forming

LBF is a manufacturing process which originated from flame bending or line heating process. This is a process whereby defocused laser beam induces thermal stresses without melting the surface of a work piece in order to produce controlled distortion. Consequently, the pressure induces plastic strains, bending the material with a heat source in which for this experiment was used for curving steel plates.

Chapter 2 highlighted that the Taguchi DoE is used to develop the L_{27} orthogonal array. The Taguchi OA output parameters are then used as LBF input parameters, where samples machined using these parameters are categorised into three levels. Level 1 in the categories is referred to as low parameter, level 2 is referred to as a medium

parameter, and level 3 is referred to as high LBF parameter settings as mentioned in previous Chapters. The quantities that are associated with each level for a specific parameter in the LBF process are presented in Table 2.3-1 of this report.

Categorisation is aimed at identifying the parameters and levels that will yield the desired results. Research has indicated that a change in the LBF process parameter quantity, result in changes of the LBF outputs. The 4.4 kW Nd: YAG laser system – Rofin DY 044, which is at the National Laser Centre (NLC), within the Council for Scientific and Industrial Research (CSIR) in Pretoria is the LBF machine that was used in machining the 200 x 50 x 3 mm^3 AISI 1008 mild steel experimental samples, as mentioned in Chapter 2. The total number of LBFormed samples are 27 as per the Taguchi L_{27} OA presented in Table 2.3-2. This means that a total of nine LBFormed samples per category were machined and three categories formed for this investigation makes a total of 27 samples.

The procedure followed to machine the experimental samples is similar to the one presented in Figure 1-1 of Chapter 1, where samples are secured and clamped during LBF process. For this investigation the Temperature Gradient Mechanism (TGM) is the LBF mechanism used for machining experimental samples. The adoption of the TGM for this investigation was motivated because it is a mechanism that is principally used at macro level to form metallic sheet material. AISI 1008 mild steel plates used for the experiment were selected to suit the criteria for applied TGM. The curvature of the LBFormed steel plates is towards the beam as expected for the TGM.

Each sample is identically machined by passing the laser light on equal parallel spacing set at 10 mm apart along the width of the surface area of each sample. The distance between the spaces (laser scan track) are set such that, the laser heated zone does not overlap to the next laser scan track and corrupt the detail of the neighbouring scan track. This was aimed to keep accuracy of the results throughout the experiment. The principle behind the sheet material process is that it uses the laser beam that is guided across the sheet surface. The laser path used is a beam moving on the straight line across the width of the whole part that is machined.

3.2 Material Bending Measurement

It has been mentioned in Chapter 2 that there are nine samples which are LBFormed using category 1 parameters, also another nine samples which are LBFormed using category 2 parameters, as well as 9 samples which are LBFormed using category 3 parameters. The combined samples for the three categories makes up a total of 27 samples to suit the requirements of the Taguchi L_{27} OA. Six of the 9 LBFormed samples from each LBF category were selected and the total number of samples measured for bending was18.

Statistically the 9 unavailable LBFormed samples which were made out of 3 unavailable LBFormed samples from each category is not expected to have a negative impact on the accuracy of the results generated. It is because the number of samples available for bending measurement for a respective LBF category are sufficient for demonstrating where the population of the results is situated in the normal distribution

curve, refer to Figure 3.4-1, 3.4-2, and 3.4-3. This means that the results for the 3 missing samples in a LBF category would have been in a region of the population generated in the charts presented in Figure 3.4-1, 3.4-2, and 3.4-3. Also the results acquired through the RSM in Chapters 5 assist in giving an indication and a comparison between the available bending measurement results and the RSM results for each LBF category.

As highlighted in Chapter 2, the sample bending analysis was carried out at the Wits University Mechanical Engineering Workshop with the tools listed in Section 2.2 of Chapter 2. The following procedure is followed to measure bending for all LBFormed samples. The square steel bar that is represented in Figure 2.2-3(C) is perfectly placed at the edge of a working bench. The steel bar is then clamped with a G clamp to have the steel bar secured and restricted into position from any movements. This is to ensure that the steel bar is rigid, because it is a reference point where samples are placed and pushed along the steel bar, so that the same reference can be maintained while sliding through the dial indictor when taking bending measurements.

A 300mm steel ruler and a permanent marker were used for measuring and marking divisions, which are the reading points in all LBFormed steel samples measured for bending. Before beginning bending measurement for each LBFormed sample, the dial indicator is adjusted to reflect 0.00mm at the starting point of 0mm of the 200mm long LBFormed steel sample. One LBFormed sample at a time is placed on the working bench against the clamped steel bar, as illustrated in Figure 3.2-1.

Figure 3.2-1 Bending Measurement on LBF Samples

The material bending results for LBFormed steel samples are presented for each LBF category in Table 3.2-1, 3.2-2, and 3.2-3. Table 3.2-1 tabulates the bending results for samples that are LBFormed using the low/level 1 LBF parameters. Table 3.2-2 are the bending results for samples that are LBFormed using medium/level 2 LBF parameters, and Table 3.2-3 are the bending results for samples that are LBFormed using high/level 3 LBF parameters respectively. In the sample bending column of Table 3.2-1, 3.2-2, and 3.2-3; L_1 =Level 1 (Low LBF parameter), L_2 = Level 2 (Medium LBF parameter), and L_3 = Level 3 (High LBF parameter). F_1, F_2… F_6 = LBFormed sample that is being measured for bending i.e. 1st, 2nd, 3rd, 4th… 6th sample in the same LBF category. Therefore, the letters in sample displacement column in Table 3.2-1, 3.2-2, and 3.2-3 can be named by starting with the subscript and the meaning of the last letter as defined in the previous sentence, that is, L_1F_1 = 1st LBFormed sample machined using low/level 1 LBF parameter, therefore, L_1F_2= 2nd LBFormed sample machined using low/level 1 LBF parameter.

Table 3.2-1 Results for Sample Displacement as Function of Position for Low/Level 1 LBF Parameters

Sample Displacement (mm)	Position on a Sample at (0mm)	Position on a Sample at (25mm)	Position on a Sample at (50mm)	Position on a Sample at (75mm)	Position on a Sample at (100mm)	Position on a Sample at (125mm)	Position on a Sample at (150mm)	Position on a Sample at (175mm)	Position on a Sample at (200mm)
L_1,F1	0	0,79	1,46	1,89	2,06	1,95	1,61	0,94	0
L_1,F2	0	1,18	2	2,55	2,76	2,6	2,1	1,31	0,11
L_1,F3	0	1,1	1,85	2,31	2,49	2,34	1,93	1,24	0,28
L_1,F4	0	1,18	2,24	2,8	3	2,76	2,18	1,22	-0,12
L_1,F5	0	0,75	1,37	1,79	1,95	1,84	1,48	0,9	0,12
L_1,F6	0	1	1,69	2,14	2,31	2,15	1,73	1,08	0,04
L_{1aver},F_{aver}	0	1	1,7683333	2,24666667	2,428333	2,273333	1,838333	1,115	0,071667

Table 3.2-2 Results for Sample Displacement as Function of Position for Medium/Level 2 LBF Parameters

Sample Displacement (mm)	Position on a Sample at (0mm)	Position on a Sample at (25mm)	Position on a Sample at (50mm)	Position on a Sample at (75mm)	Position on a Sample at (100mm)	Position on a Sample at (125mm)	Position on a Sample at (150mm)	Position on a Sample at (175mm)	Position on a Sample at (200mm)
L_2,F1	0	3,89	5,76	7,66	8,4	7,89	6,2	3,57	-0,02
L_2,F2	0	4,05	7,06	8,81	9,53	9,05	7,39	4,56	0,44
L_2,F3	0	3,59	6,5	8,27	8,93	8,54	7,05	4,4	0,59
L_2,F4	0	3,44	6,07	7,89	8,55	8,05	6,45	3,78	0,34
L_2,F5	0	3,5	6,46	8,35	9,03	8,47	6,66	3,73	0,5
L_2,F6	0	3,33	6,1	7,89	8,75	8,23	6,43	3,73	0,22
L_{2aver},F_{aver}	0	3,633333	6,325	8,145	8,865	8,371667	6,696667	3,961667	0,345

Table 3.2-3 Results for Sample Displacement as Function of Position for High/Level 3 LBF Parameters

Sample Displacement (mm)	Position on a Sample at (0mm)	Position on a Sample at (25mm)	Position on a Sample at (50mm)	Position on a Sample at (75mm)	Position on a Sample at (100mm)	Position on a Sample at (125mm)	Position on a Sample at (150mm)	Position on a Sample at (175mm)	Position on a Sample at (200mm)
L_3,F1	0	7,65	12,88	17	18,7	17,58	14,78	8,82	0,44
L_3,F2	0	7,18	12,43	16,66	17,92	16,6	13,47	7,65	0,32
L_3,F3	0	8,45	15,22	19,49	21,65	20,05	15,95	9,86	0,93
L_3,F4	0	7,76	13,23	17,03	18,46	17,81	15,24	9,81	0,82
L_3,F5	0	7,47	13,37	17,27	19,38	17,85	14,39	8,01	0,41
L_3,F6	0	9,57	15,19	20,56	22,7	20,71	15,88	9,3	0,38
L_{3aver},F_{aver}	0	8,013333	13,72	18,0016667	19,80167	18,43333	14,95167	8,908333	0,55

The bending results captured in the above thee tables are graphically represented in Figure 17, 18, and 19 of section 3.4.

3.3 Observations

The behaviour for all LBFormed samples measured for bending using the three LBF categories showed similar profiles for bending measurement. It is observed that all samples that are LBFormed using high LBF parameters have maximum curvatures with rough surfaces. The areas on samples where the laser beam had passed through are extremely rough. This is caused by the material property change, since high heat intensity on the material affects material properties [53 to 55]. A similar effect where rough surface finish is noted on samples, is where slower scan velocity and high beam intensity were applied to LBF the samples. Samples which are LBFormed using medium LBF parameter were observed to be slightly less curved and less rough than samples that are LBFormed using high LBF parameters. A marginal change in sample curvature and surface roughness observed in samples that are LBFormed using low LBF parameters. The most apparent observation in this category is the visibility of the laser scan, which left a darker flame colour on sample surfaces due to laser beam irradiation.

3.4 Results and Discussions

The data that is captured from Table 3.2-1, 3.2-2, and 3.2-3 is plotted in Figure 3.4-1, 3.4-2, and 3.4-3. Figure 3.4-1, 3.4-2, and 3.4-3 are column charts representing bending for LBFormed samples for the entire length of individual sample. Both the sample bending and the sample length in Figure 3.4-1, 3.4-2, and 3.4-3 are recorded in millimetres.

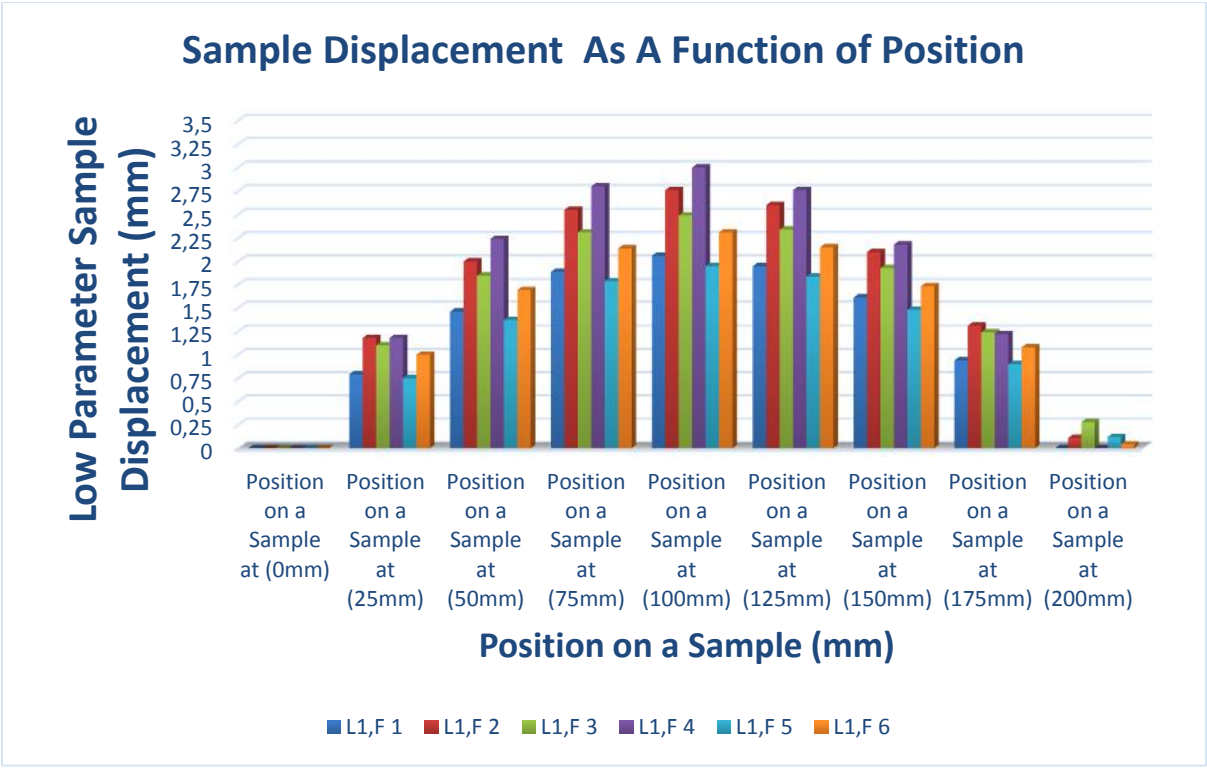

Figure 3.4-1 Graph of Sample Displacement as a Function of Position on Low/Level 1 LBF Parameters

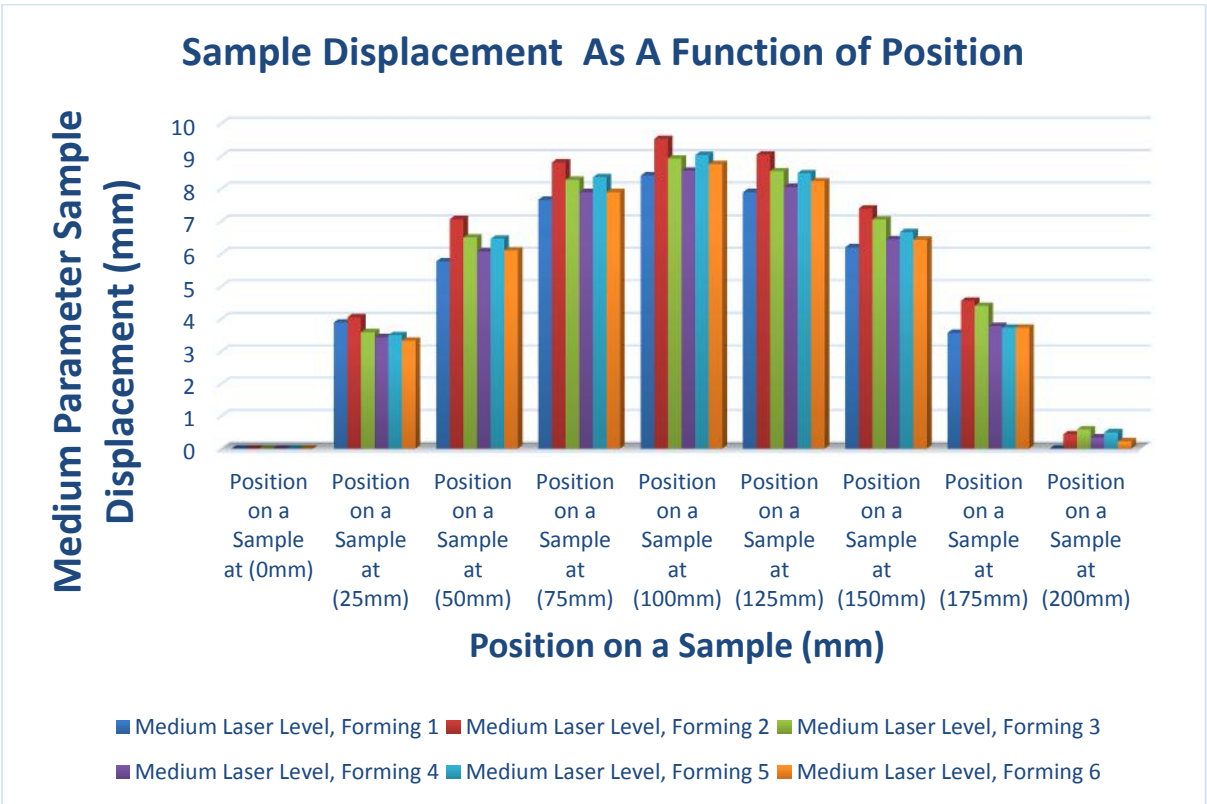

Figure 3.4-2 Graph of Sample Displacement as a Function of Position on Medium/Level 2 LBF Parameters

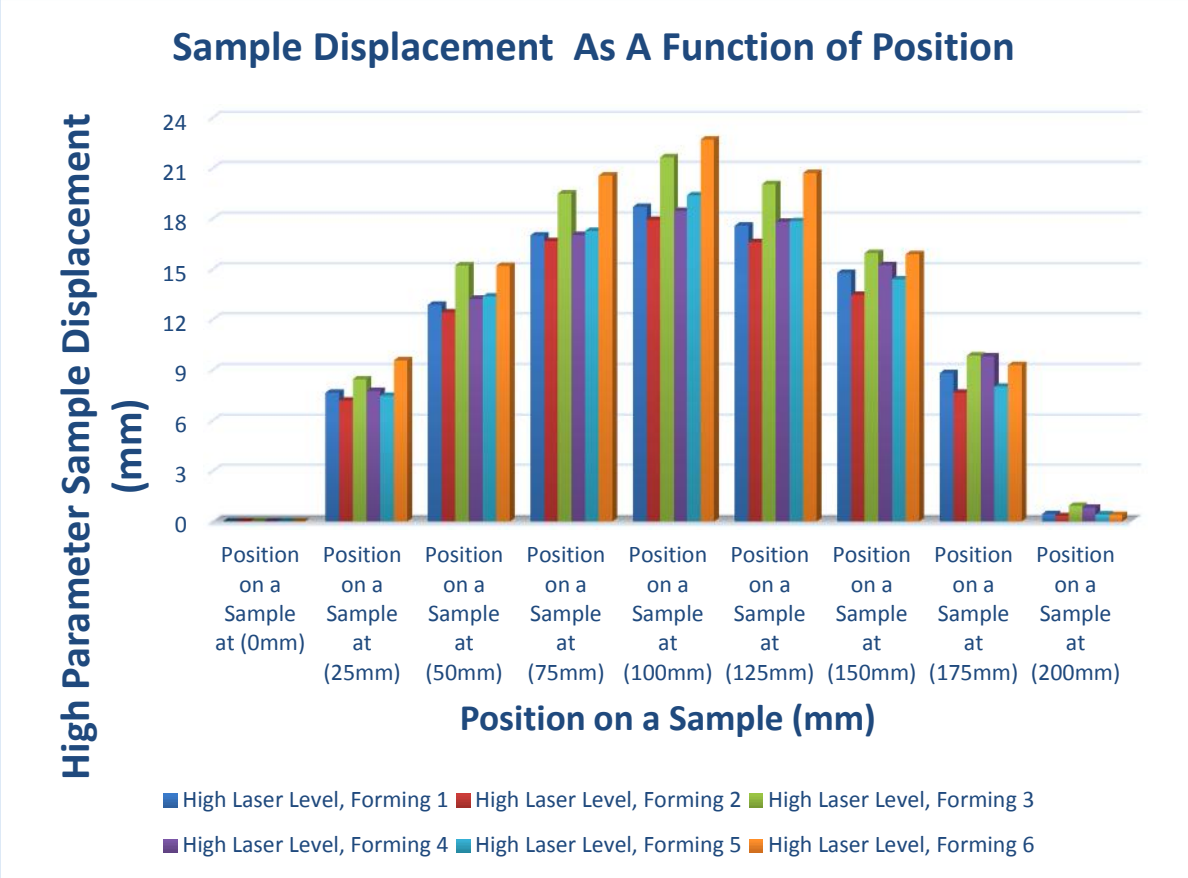

Figure 3.4-3 Graph of Sample Displacement as a Function of Position on High/Level 3 LBF Parameters

The same data plotted in Figure 3.4-1, 3.4-2, and 3.4-3 is presented using line charts in Figure 8.1-1, 8.1-2, and 8.1-3 in Appendix B for more bending behavioural expression. The average values for sample bending results are captured at the bottom row of Table 3.2-1 as $\mathbf{L_{1aver}}$, $\mathbf{F_{aver}}$, where $\mathbf{L_{1aver}}$, $\mathbf{F_{aver}}$ = results for average LBFormed samples for level 1 LBF parameters. A similar procedure is followed to capture the average sample bending results for Table 3.2-2, where $\mathbf{L_{2aver}}$, $\mathbf{F_{aver}}$ = results for average LBFormed samples for level 2 LBF parameters. Also, the average sample bending is also captured for Table 3.2-3, where $\mathbf{L_{3aver}}$, $\mathbf{F_{aver}}$ = results for average LBFormed samples for level 3 LBF parameters. The data that is collected from the three LBF average level parameters is plotted against each other in a column chart,

see Figure 3.4-4. Figure 3.4-4 gives a good indication that demonstrates the influence that each LBF category have on the sample bending results.

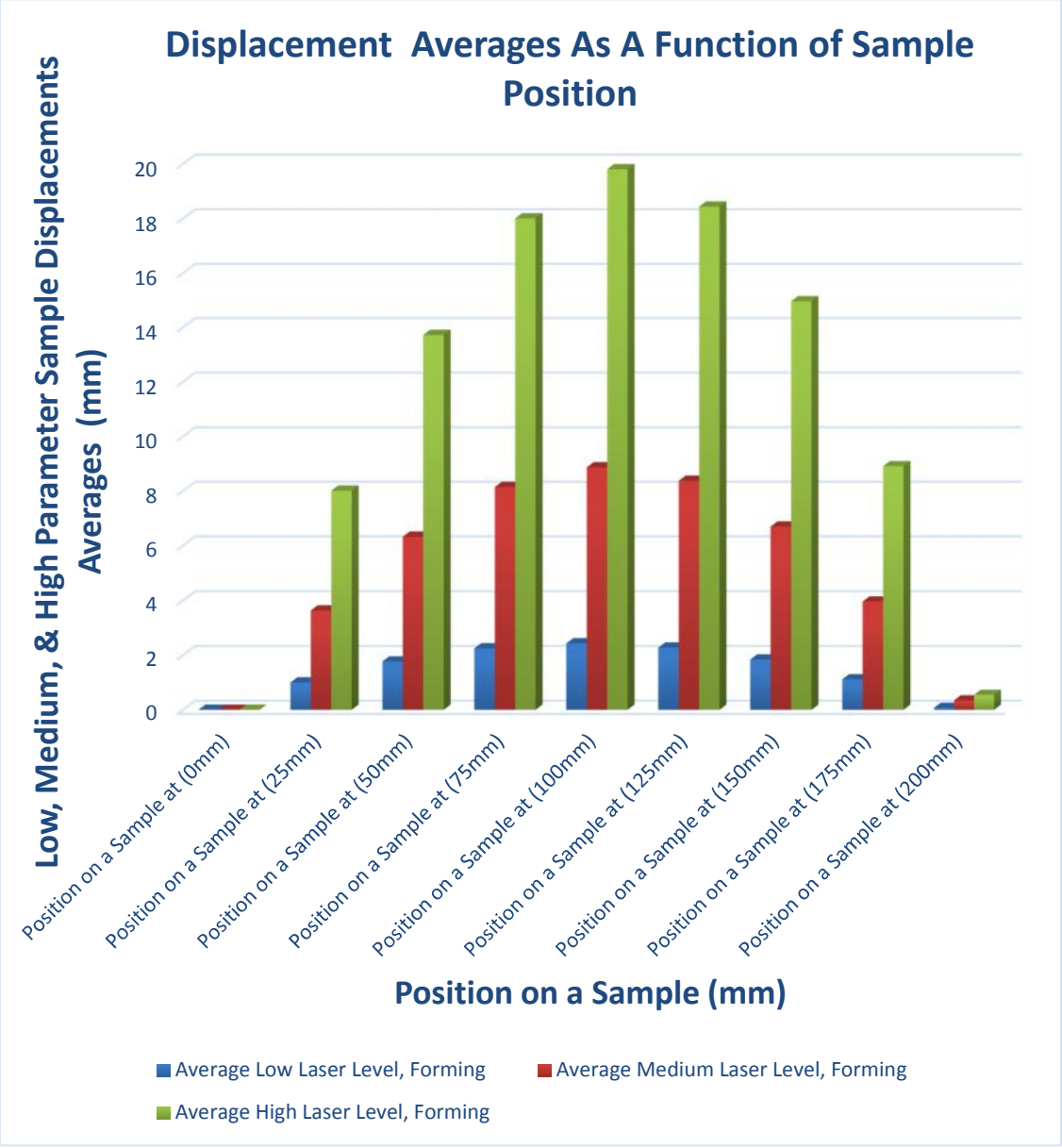

Figure 3.4-4 Displacement Averages as A Function of Position, on Low, Medium, & High LBF Parameters

As illustrated in Figure 3.4-4 there is no overlapping on the bending results generated amongst categories i.e. when looking at the bending results at each increment of

25mm over the sample length, there is no overlap in the sample bending results for the three LBF level categories. These results confirm that the sample bending for samples machined using level 1 LBF category is lower when compared to the samples machined using level 2 LBF category. Also, the bending for samples machined using level 3 LBF category were observed to be higher when compared to the bending for samples machined using level 2 and 1 LBF categories. It can be witnessed from the sample bending results that on the reference points, beginning and end, sample bending is at the lowest and it is almost equal. This was because at the edge of the sample bending is not favourable due minimal buckling [56].

Although there is no overlapping in sample bending results from the reading taken from the three categories, variations in bending results that are taken from the same category and at same increment were observed. This sample bending variation is believed to have been caused by the fact that each sample was LBFormed with unique parameter combinations that were identified in the OA and a change in LBF process parameters, caused a change in the bending results [4, 56]. The calculation of the average sample bending results $\mathbf{L_{aver}}$, $\mathbf{F_{aver}}$ recorded in Table 3.2-1, 3.2-2, and 3.2-3 were aimed at analysing the behaviour of the sample bending results with those gathered for each increment in the respective tables. The accuracy of the sample bending results for each LBF category was further analysed by determining the positive and the negative percentage sample bending error results which are tabulated in Table 3.4-1, 3.4-2, and 3.4-3 respectively.

Table 3.4-1 Low Parameter LBF, Sample Bending Percentage Error Results Calculation

	Percentage Error Calculation for Low parameter Settings Measurements for Samples								
Sample Length (mm)	**Sample Length (0mm)**	**Sample Length (25mm)**	**Sample Length (50mm)**	**Sample Length (75mm)**	**Sample Length (100mm)**	**Sample Length (125mm)**	**Sample Length (150mm)**	**Sample Length (175mm)**	**Sample Length (200mm)**
Max value	0	1,18	2,24	2,8	3	2,76	2,18	1,31	0,28
Ave value	0	1	1,768333	2,246667	2,428333	2,273333	1,838333	1,115	0,071667
Positive Error Value	0	0,18	0,471667	0,553333	0,571667	0,486667	0,341667	0,195	0,208333
Min value	0	0,75	1,37	1,79	1,95	1,84	1,48	0,9	-0,12
Ave value	0	1	1,768333	2,246667	2,428333	2,273333	1,838333	1,115	0,071667
Negative Error Value	0	0,25	0,398333	0,456667	0,478333	0,433333	0,358333	0,215	0,191667

Table 3.4-2 Medium Parameter LBF, Sample Bending Percentage Error Results Calculation

	Percentage Error Calculation for Medium parameter Settings Measurements for Samples								
Sample Length (mm)	**Sample Length (0mm)**	**Sample Length (25mm)**	**Sample Length (50mm)**	**Sample Length (75mm)**	**Sample Length (100mm)**	**Sample Length (125mm)**	**Sample Length (150mm)**	**Sample Length (175mm)**	**Sample Length (200mm)**
Max value	0	4,05	7,06	8,81	9,53	9,05	7,39	4,56	0,59
Ave value	0	3,633333	6,325	8,145	8,865	8,371667	6,696667	3,961666667	0,55
Positive Error Value	0	0,416667	0,735	0,665	0,665	0,678333	0,693333	0,598333	0,245
Min value	0	3,33	5,76	7,66	8,4	7,89	6,2	3,57	-0,02
Ave value	0	3,633333	6,325	8,145	8,865	8,371667	6,696667	3,961667	0.55
Negative Error Value	0	0,303333	0,565	0,485	0,465	0,481667	0,496667	0,391667	0,365

Table 3.4-3 High Parameter LBF, Sample Bending Percentage Error Results Calculation

	Percentage Error Calculation for High parameter Settings Measurements for Samples								
Sample Length (mm)	**Sample Length (0mm)**	**Sample Length (25mm)**	**Sample Length (50mm)**	**Sample Length (75mm)**	**Sample Length (100mm)**	**Sample Length (125mm)**	**Sample Length (150mm)**	**Sample Length (175mm)**	**Sample Length (200mm)**
Max value	0	9,57	15,22	20,56	22,7	20,71	15,95	9,86	0,93
Average value	0	8,01333	13,72	18,00167	19,80167	18,43333	14,95167	8,908333	0,55
Positive Error Value	0	1,556667	1,5	2,558333	2,898333	2,276667	0,998333	0,951667	0,38
Min value	0	7,18	12,43	16,66	17,92	16,6	13,47	7,65	0,32
Average value	0	8,01333	13,72	18,00167	19,80167	18,43333	14,95167	8,908333	0.55
Negative Error Value	0	0,833333	1,29	1,341667	1,881667	1,833333	1,481667	1,258333	0,23

Figure 3.3-5 is a line plot presenting three category LBF sample bending averages with positive and negative percentage errors from the results generated from Table 3.4-1, 3.4-2, and 3.4-3. The three sample bending plots in one chart as presented in Figure 3.3-5 follow similar parabolic profiles to those that are presented in Figure 3.4-1, 3.4-2, and 3.4-3. A 2nd order polynomial trend-line is found to be the best fit for the three sample bending curves as it provides better R^2 values that are close to 1.

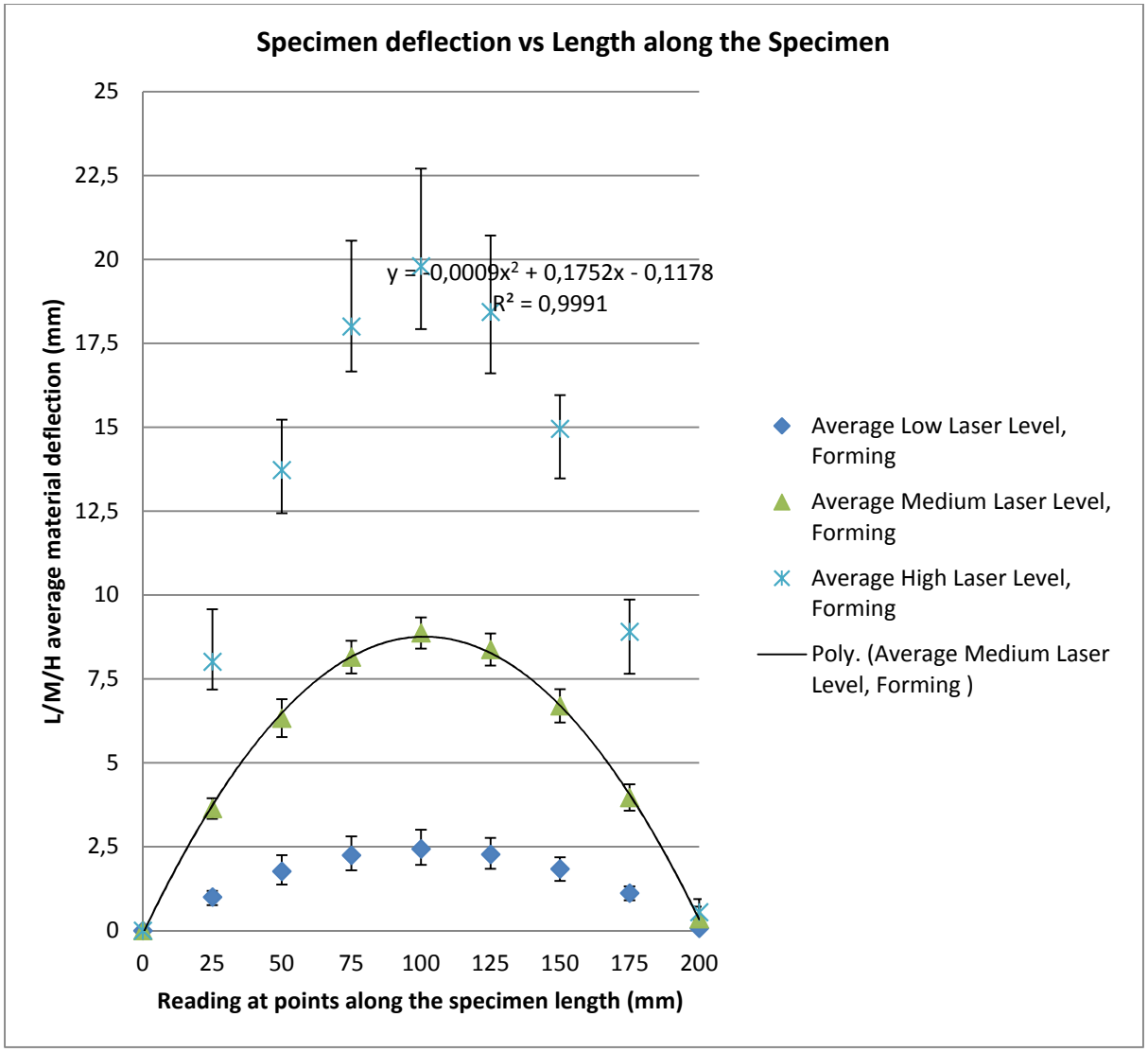

Figure 3.4-5 Three Sample Bending Averages vs Length, on Low, Medium, & High Parameter LBF line chart

The equation of the chart is shown in Figure 3.4-5 and the method used to determine it is presented using equation 22.

1. From the sample bending average curve, the equation for the low level LBF

$$Points\ on\ t\square e\ middle\ curve\ \ 100; 2.428\ ;\ \ 150; 1.838$$

$$Equation\ of\ a\ parabola\ y = \ a(x - \square)^2 + \ k \qquad \ldots\ldots\ldots\ldots\ldots\ldots\ (22)$$

$$w\square ere\ \square = \ 10, k = \ 2.428, x = \ 15, and\ y = \ 1.838$$

$$y = a(150 - 100)^2 + 2.428$$

$$1. \approx -0.000236x^2 + 0.05136x - 0.134$$

2. The equation of the medium bending average curve

$$Points\ on\ t\square e\ middle\ curve \quad 100; 8.865 \ ; \ 150; 6.69$$

$$w\square ere\ \square = 100, k = 8.865, x = 150, and\ y = 6.69 \quad substitute\ in\ eqn\ (22)$$

$$y = a(150 - 100)^2 + 8.865$$

$$\approx -0.00087x^2 + 0.174x - 0.165$$

3. The equation of the high bending average curve

$$Points\ on\ t\square e\ middle\ curve \quad 100; 19.8 \ ; \ 150; 15$$

$$w\square ere\ \square = 100, k = 19.85, x = 150, and\ y = 15 \quad substitute\ in\ eqn\ (22)$$

$$y = a(150 - 100)^2 + 19.8$$

$$\approx -0.00192x^2 + 0.384x - 19.78$$

It can be observed in all sample bending plots for this experiment that maximum bending for all samples was at the midpoint which is at 100 mm of the 200mm long sample. The results from Figure 3.4-1, 3.4-2, and 3.4-3 shows that samples machined using low/level 1 LBF parameters had the smallest bending and this observation was also witnessed by looking at the sample and by analysing the bending results. While samples machined using medium/level 2 LBF parameters have more bending than samples machined using low/level 1 LBF parameters. Maximum sample bending

results in the experiment were seen on samples machined using high/level 3 laser forming parameters.

3.5 Conclusion

This research was aimed at identifying LBF process parameters that would yield the maximum material bending with good material surface finishing. Samples machined using low/level 1 LBF parameters had negligible bending and relatively smooth surface finishing except visible laser forming scan tracks on sample surface [4, 57]. While on the other hand samples that are LBFormed using medium/level 2 LBF parameters have substantial bending with rough surfaces [57-58]. Also, samples that are LBFormed using high/level 3 LBF parameters have larger bending and surface roughness than samples LBFormed using the low/level1 and medium/level 2 LBF parameters [57-58]. The discussion and analysis of sample surface roughness is presented in Chapter 4 of this research report. It has been mentioned that this maximum bending and surface roughness in samples is mainly contributed by the fact that steel undergoes through material property changes when it is subjected to intense heat and that causes steel to be elastic [57].

All LBFormed samples in categories mentioned followed similar profiles irrespective of the LBF level parameter used as mentioned in the observations. This observation is seen as a confirmation of consistency on laser machine setup for determining bending. Non-overlapping of sample bending results i.e. the results derived from low LBF parameters do no coincides with those derived from samples LBF using medium

LBF parameters. The same behaviour is witnessed for level 2 sample bending results against level 3 LBFormed sample bending results. The results also provides evidence that samples were correctly grouped according to the LBF level parameters used to the samples

It can be concluded that the bending magnitude results have a direct proportionality with the average bending percentage error. This is derived from the observation that for smaller sample bending the average percentage error generated is also small and vice versa [9, 58].

The experimental results are in conjunction to the literature. The input parameters for the LBF process that is derived from the Taguchi selection matrix was able to generate the maximum bending results, however the objective for obtaining smooth surface roughness was not achieved by the input parameters derived from the experimental L_{27} OA so far. Further investigations will be done in subsequent Chapters to analyse the parameters in seeking to meet the objective. These investigations will be carried out by analysing LBFormed samples through microscopic analysis, micro-hardness testing, and RSM in Chapter 4 and 5.

.

Chapter 4

Microscopy and Microanalysis, Micro Hardness Test

This chapter covers experiment procedures and results for the experiments that were carried through at the MMU for LBFormed mild steel -AISI 1008 plates. In this chapter details of the microscopes used are shared as well as the procedure for carrying out the analysis. The details of the micro hardness test analysis carried out is also contained in this chapter.

4.1 Confocal Microscope

The confocal microscopy is an optical imaging technique that uses point illumination and a spatial pinhole in an optically conjugate plane in front of the detector to eliminate out-of-focus light in specimens that are thicker than the focal plane. This technique enables optical sectioning in sample depth direction. The achievable thickness of the focal plane is defined mostly by the wavelength of the used light divided by the numerical aperture of the objective lens, but also by the optical properties of the specimen. As only one point in the sample is illuminated at a time, 2D or 3D imaging requires scanning over a regular raster in the specimen. This illumination technique is often combined with fluorescence microscopy [59]. Hence the only light produced by fluorescence very close to the focal plane can be detected, and the image's optical

resolution, particularly in the sample depth direction, is much better than that of wide-field microscopes. However, as much of the light from sample fluorescence is blocked at the pinhole, this increased resolution is at the cost of decreased signal intensity – and long exposure times are often required. Besides increasing optical resolution, its optical sectioning capabilities allow for the reconstruction of three-dimensional structures from the obtained images. Thus, this technique proves particularly good for 3D imaging and surface profiling of samples, and typical applications are in life sciences and materials science. Yet, the individual set-up and microscope configurations are different for life sciences and the materials science applications [59].

4.2 Microscopic Analysis

Samples analysed under the light of a microscope were reduced from 200 x 50 x 3 mm^3 by cutting them to 75 x 20 x 3mm^3 size as shown in Figure 2.2-4 of Chapter 2. Each sample was analysed on its own and a step by step procedure on how the analysis was done including the demonstration on the controls of the microscope is discussed. The images contained in this chapter were taken from the University of Witwatersrand Microscopy and Microanalysis Unit (MMU) during investigation and pictures which are taken from the literature are referenced. The cover of the microscope was removed and the stage position was checked.

The Leica confocal microscope was started by following instructions;

1) All electronics were checked to be OFF, then the Hg arc power supply marked #1 in Figure 4.2-1 was switched on
2) The Microscope Controller power marked #2 also in Figure 4.2-1 was also switched on.
3) The PC Stand Power marked #3, which is a red toggle was switched on, and the CPU start key was switched on as shown in Figure 4.2-2
4) The Scanner Power #4 red toggle in Figure 4.2-2 was switched on.
5) The laser blower #5a red toggle in Figure 4.2-2 was switched on
6) Logged on Windows XP
7) Clicked LCS Confocal Icon

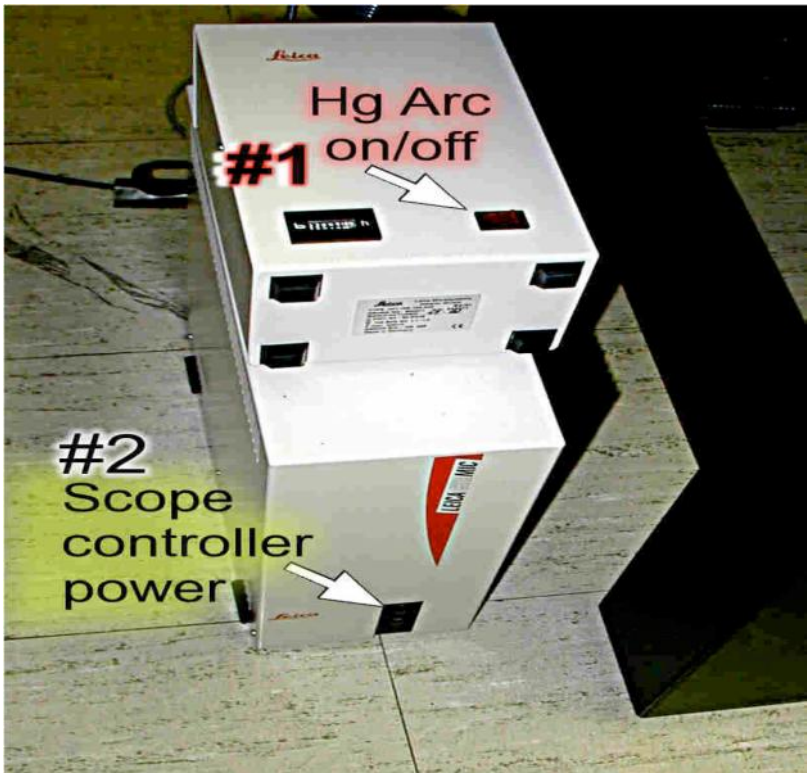

Figure 4.2-1 Hg Arc Microscope Power Supply and Power Controller

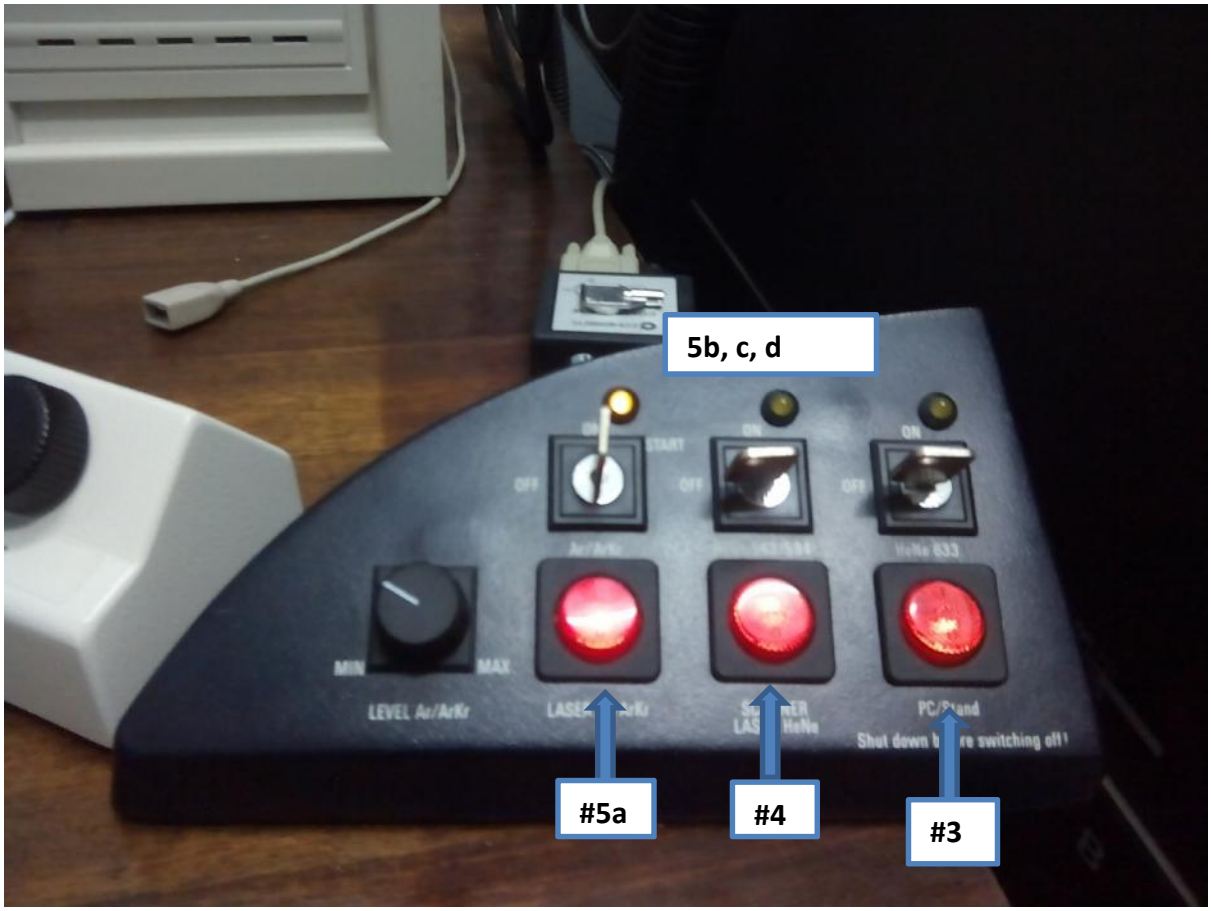

Figure 4.2-2 Microscope control panel (PC Stand, Scanner, Laser, and Ar Laser Blower)

After the above steps were completed, one sample was analysed at a time and was placed on top of the stage as shown in Figure 4.2-3. The knob on the right-hand side of the condenser was flipped to “VIS” to be able to see the samples when looking through oculars (see Figure 4.2-4).The DIC power light controller was turned on to shine on the sample. Intensity is increased by shifting up the power wheel which is on the left-hand side of the microscope in front of the focus knob.

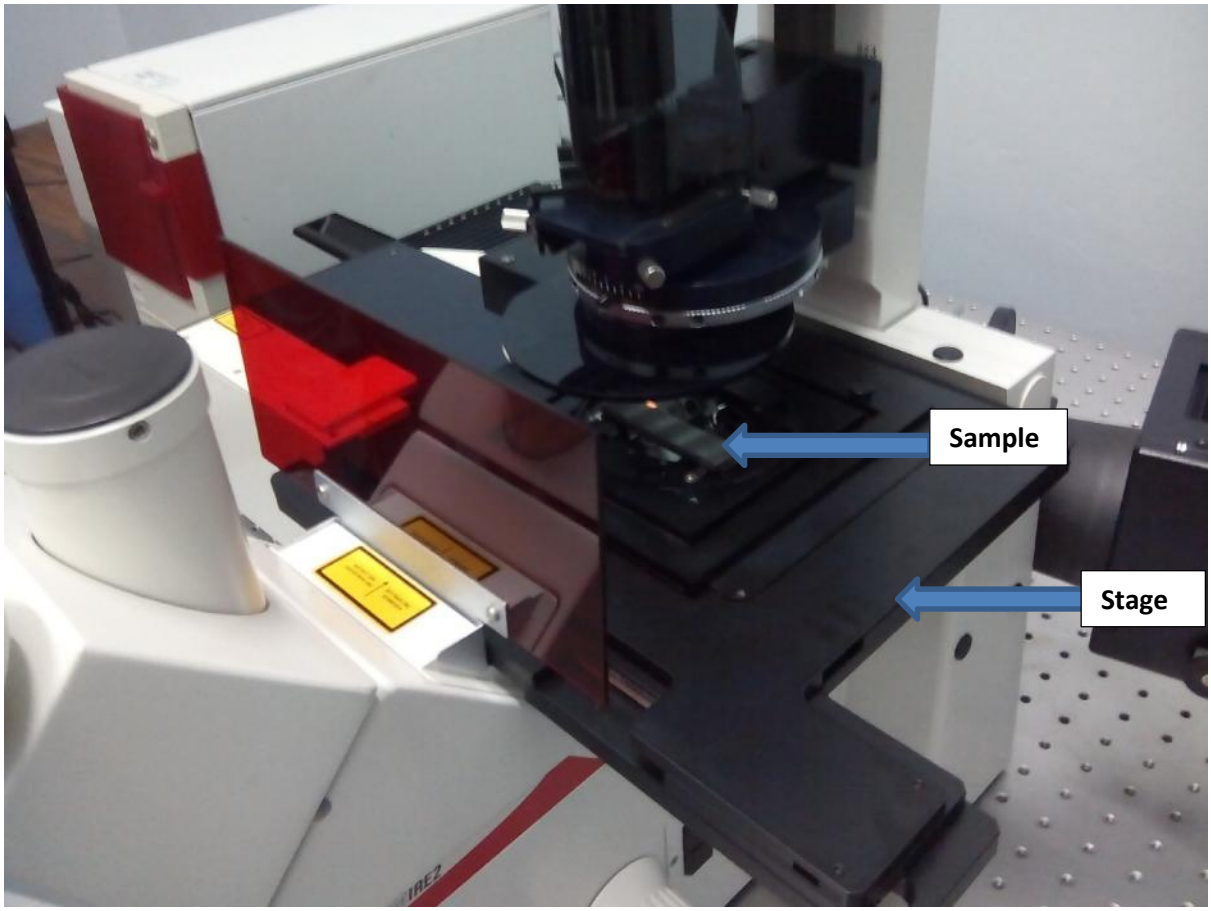

Figure 4.2-3 Steel sample to be tested placed on the stage of the microscope

The stage was moved in such a way that half the DIC power light beam shined on the sample to be able to focus the sample easily. The fast focus knob shown in Figure 4.2-4 was used to focus the sample. After the sample was focused, the knob on the right hand side of the condenser is flipped to “SCAN”.

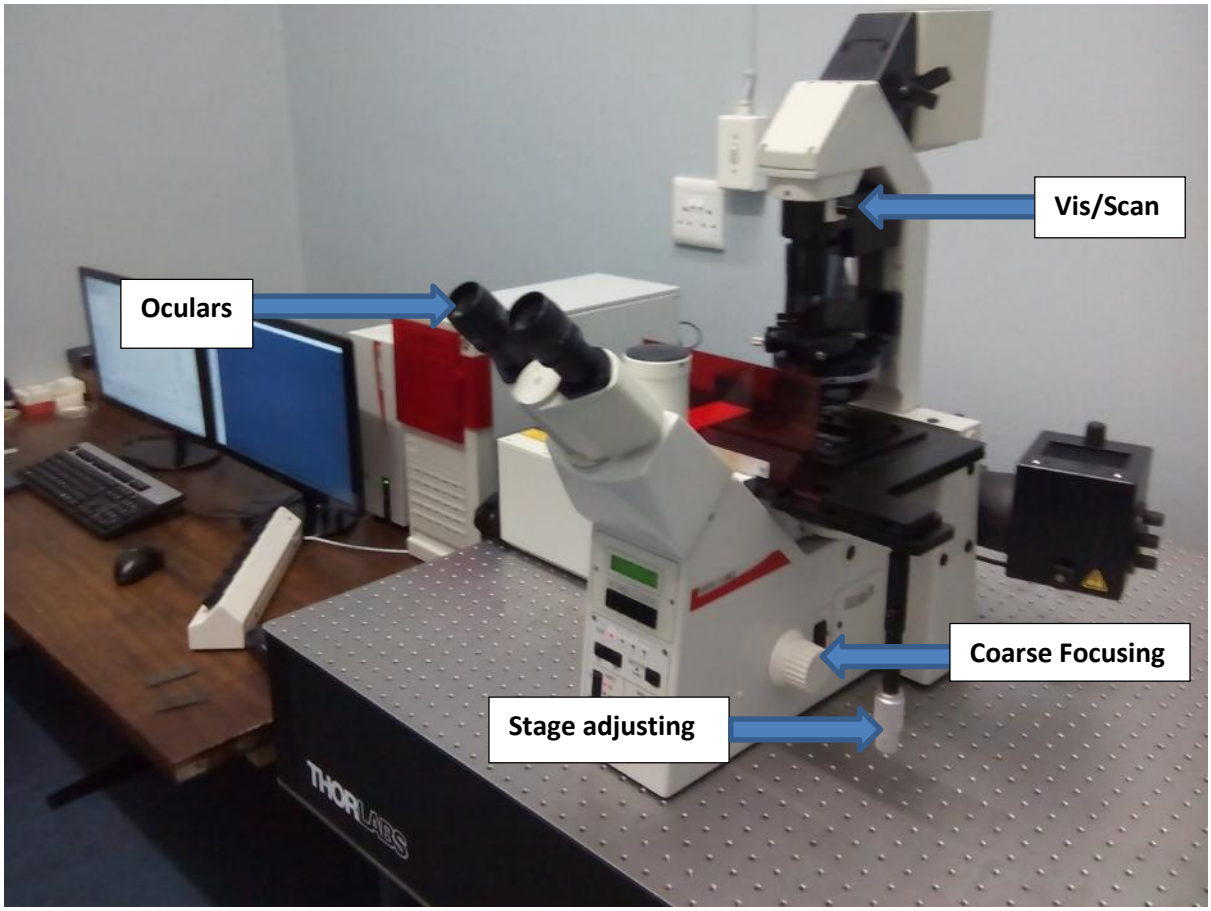

Figure 4.2-4 Leica Confocal components

4.3 The Leica LCS Software

To start the software, login to the CPU and choose the Leica Confocal Software icon: The software will open with a menu asking if you want “personal”, “company”, or “basic company” settings and “personal” was chosen, see Figure 4.3-1.

Figure 4.3-1 Leica Software Opening Window

After the software started, two screens as in Figure 4.3-2 appears. The black/image window on the right of Figure 4.3-2 initially appears on the top of the beam window which is shown on the left of Figure 4.3-2. The black/image window is then dragged to the right as shown in Figure 4.3-2.

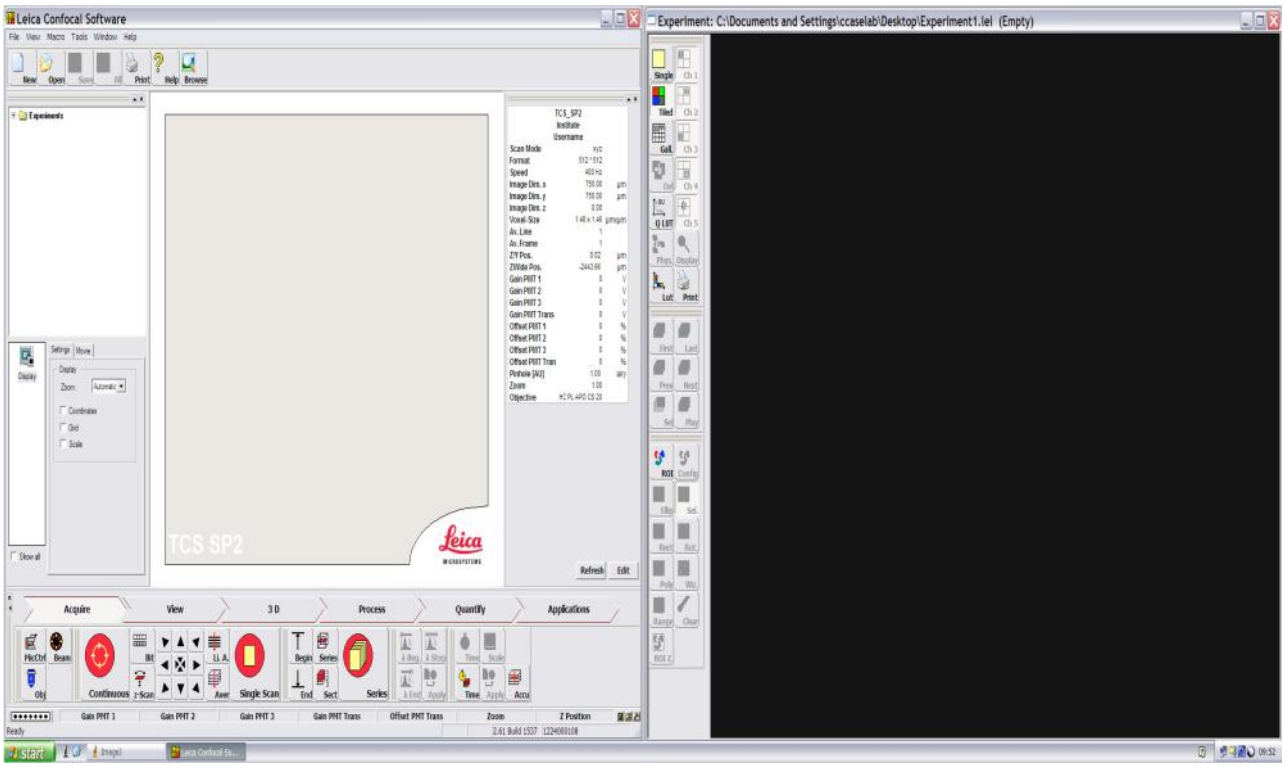

Figure 4.3-2 Beam Window and Black/Image Window

In the beam window under acquire; the microscope control (MicCtrl), beam, objective, and Z scan control panels appears. These windows are magnified in Figure 4.3-3.

Figure 4.3-3 Function of the control panel under acquire window

MicCtrl is selected to ensure that it is on “Scan”. The Obj function is clicked and the “HC x PL Fluotar 5 x 0.15 combi” is selected. Another click on Beam and scroll under user to select “Reflection” (see Figure 4.3-4 to 4.3-8). Z-Scan in Figure 4.3-3 is clicked

and “z wide” is selected to enable to cover the sample when the microscope is performing a sample scan.

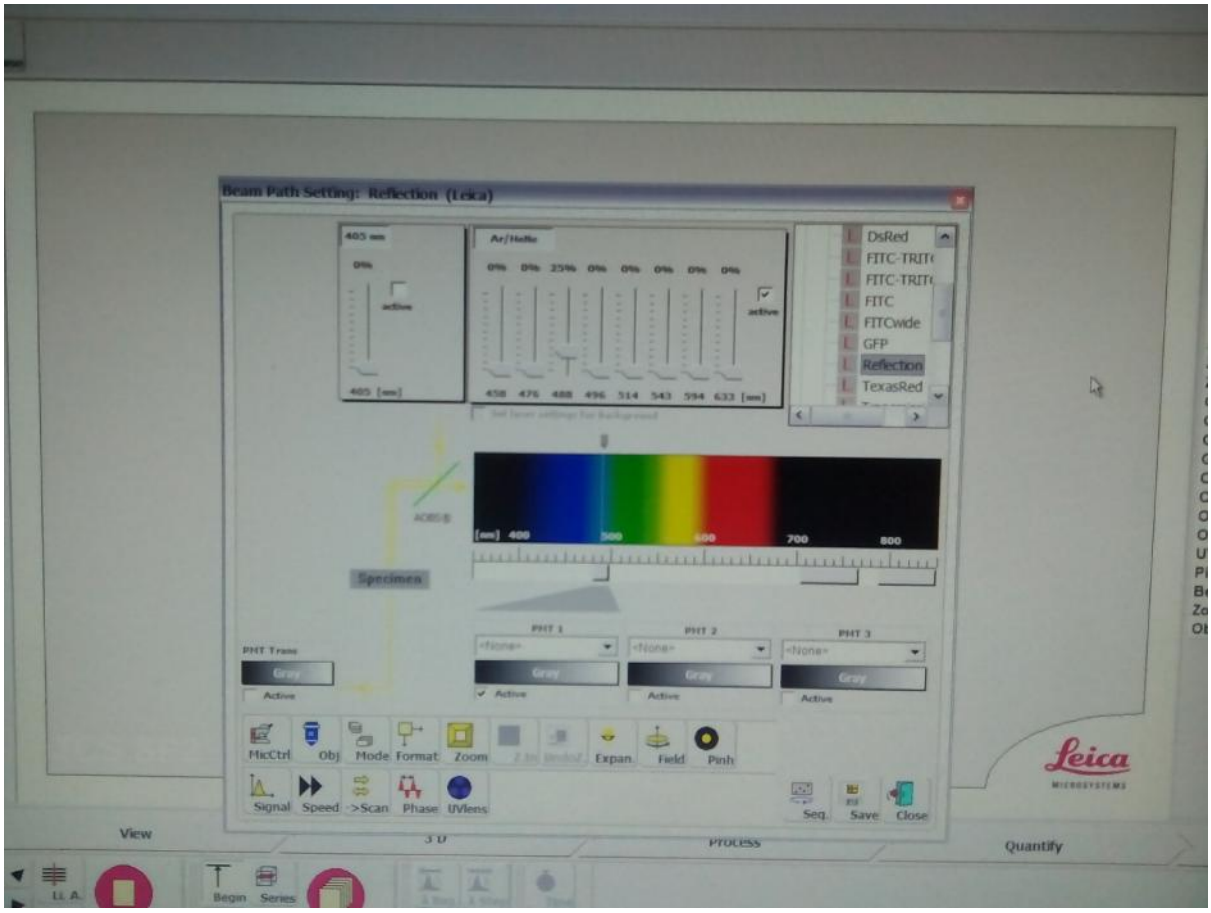

Figure 4.3-4 Beam Selection Window

- **Taking an Image**

Once the Beam window is set and the sample is in focus, it is finally time to capture an image. For capturing images, buttons along the bottom of the left-hand window and the dials on the control panel located below the monitors as in Figure 4.3-5 which is the magnification of the bottom left of Figure 4.3-2 are used.

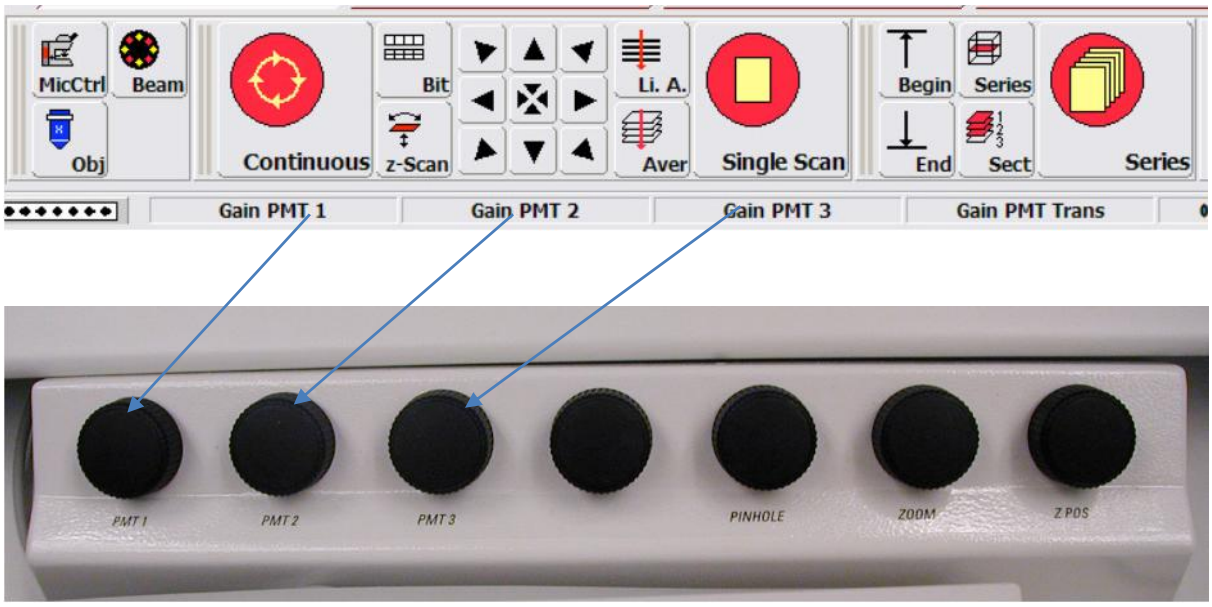

Figure 4.3-5 Images Capturing Buttons

The image is previewed by clicking the “Continuous’’ button. The laser light should come on and begin scanning over the sample. The smaller “Series” button is selected and then begin when the first focus of the image is obtained. When the second focus of the image is obtained, the end button is selected. After this action, the image in Figure 4.3-6 was observed.

Figure 4.3-6 Mild Steel – AISI 1008 Plate LBFormed Sample Image

4.4 Micro Hardness Test

After the microscopy and microanalysis on experimental samples, Vickers Hardness (HV) test was done for further analysis. One random sample per laser forming category i.e. low, medium, and high laser forming parameters were prepared for HV test. This was to further determine and validate the influence that laser parameters have on samples formed using the process parameter values discussed in Table 2.3-1 of this thesis i.e. verification on whether laser forming does alter material strength besides the surface roughness that is evident even with the naked eye on laser formed samples.

4.5 Performing Micro Hardness Test

The micro-hardness testing machine used to carry out the hardness test on experimental samples is the Future Tech FM-700 as mentioned in Chapter 2. Indentations were done on a scale of micrometres (µm) apart called width's and depth's created using a 0.5kg load at 15s dwell time. A total of 50 indentations were done per sample in order to get as much clarity and conclusiveness from the experiment as possible. Several indentations were done on LBFormed and non-LBFormed regions, also referred to as laser and non-laser scan tracks for samples machined using low, medium, and high laser forming parameters.

The width and the results for the corresponding HV number per micro-hardness tested area/indentation on the sample were recorded. The average HV values per indentation, on each region on the sample were determined. Furthermore; the total HV values which are the ultimate sum of HV values for laser and non-laser formed regions

per sample were also captured to compare the overall strength of each indented sample. The HV values from the indented samples were captured Table 4.7-3.

4.6 Observations

In Figure 4.6-1 a series arrangement function was selected to set the beginning and end of focus for the mild steel AISI 1008 plate being analysed. Figure 4.6-2 is a magnification of a series function from Figure 4.3-5. The intensity compensation and a linear gain option were checked. The option to scale the image was checked. Then the continuous button as in Figure 4.3-5 was clicked for the microscope to capture all images in the above selected series range as in 4.6-2.

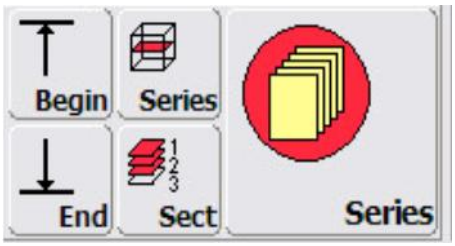

Figure 4.6-1 Microscope Series Function

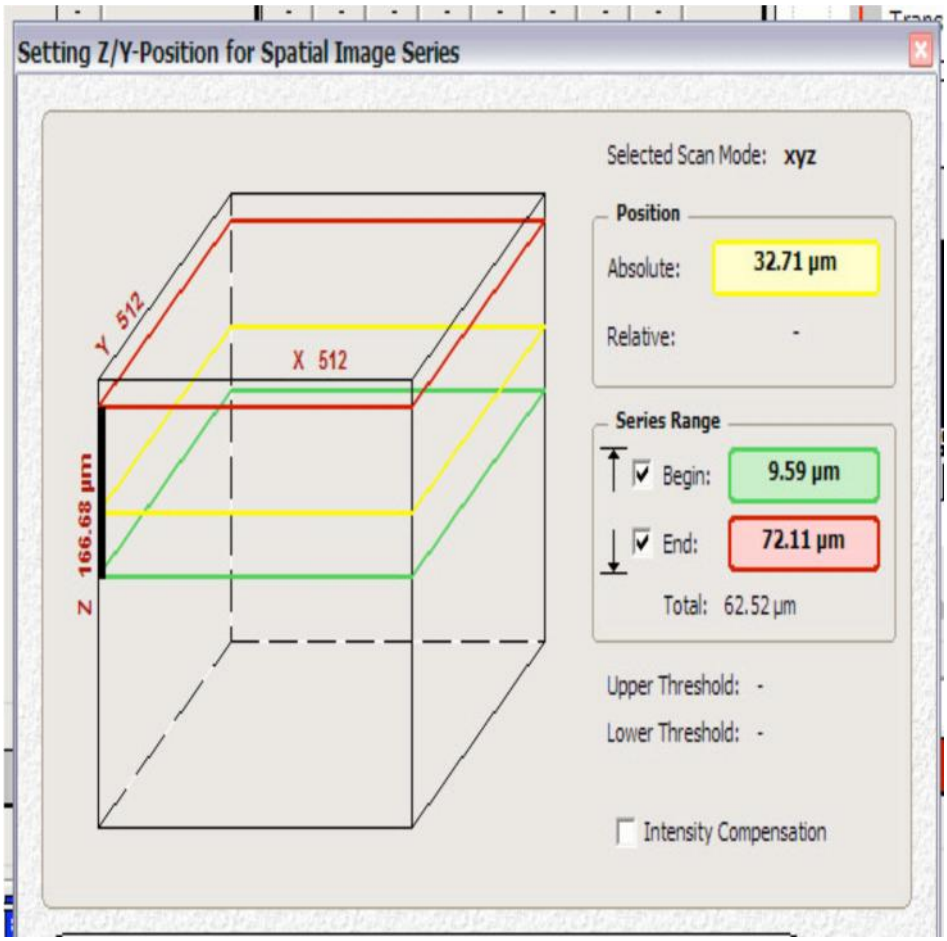

Figure 4.6-2 Series Range

After the selection of parameters listed above, the 3D function was selected to generate a Topographic image showing the surface roughness with the arrangement and limits of the sample. Figures 4.6-3, 4.6-4, and 4.6-5 are topographic images for low, medium, and high LBF parameter setting for the samples. In total nine samples were analysed and three from each laser forming category mentioned.

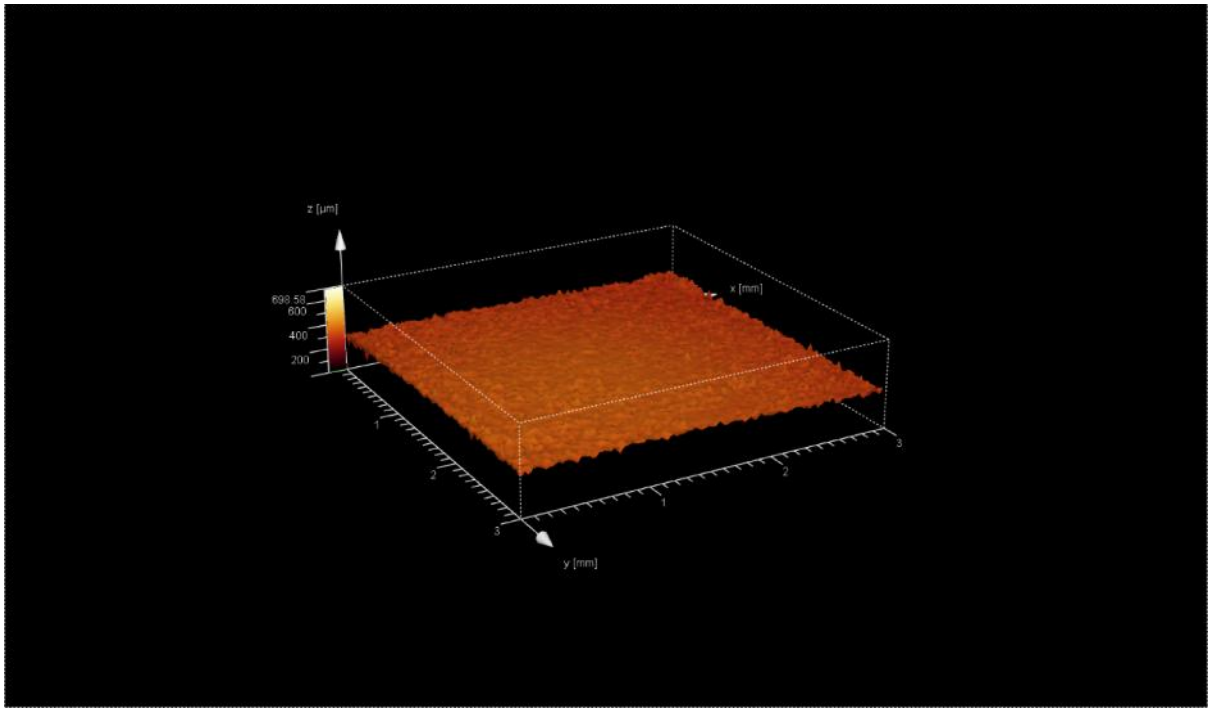

Figure 4.6-3 Topographic Image of Low Parameter Laser Formed Sample

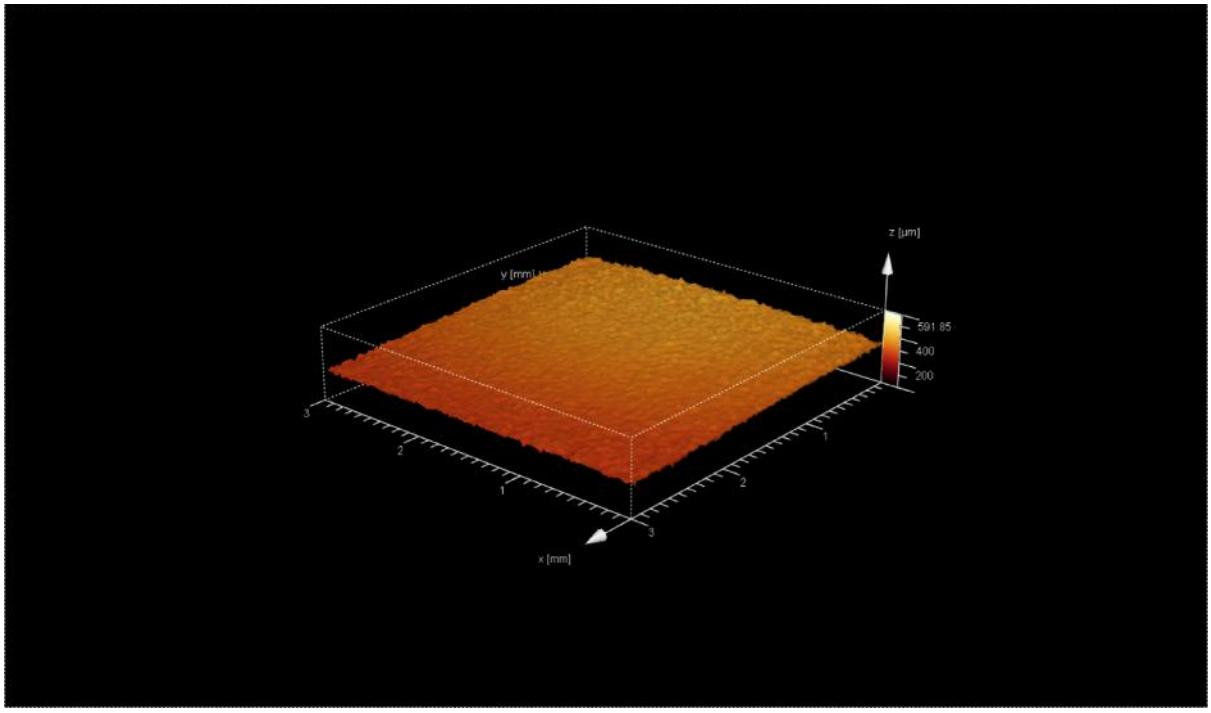

Figure 4.6-4 Topographic Image of Medium Parameter Laser Formed Sample

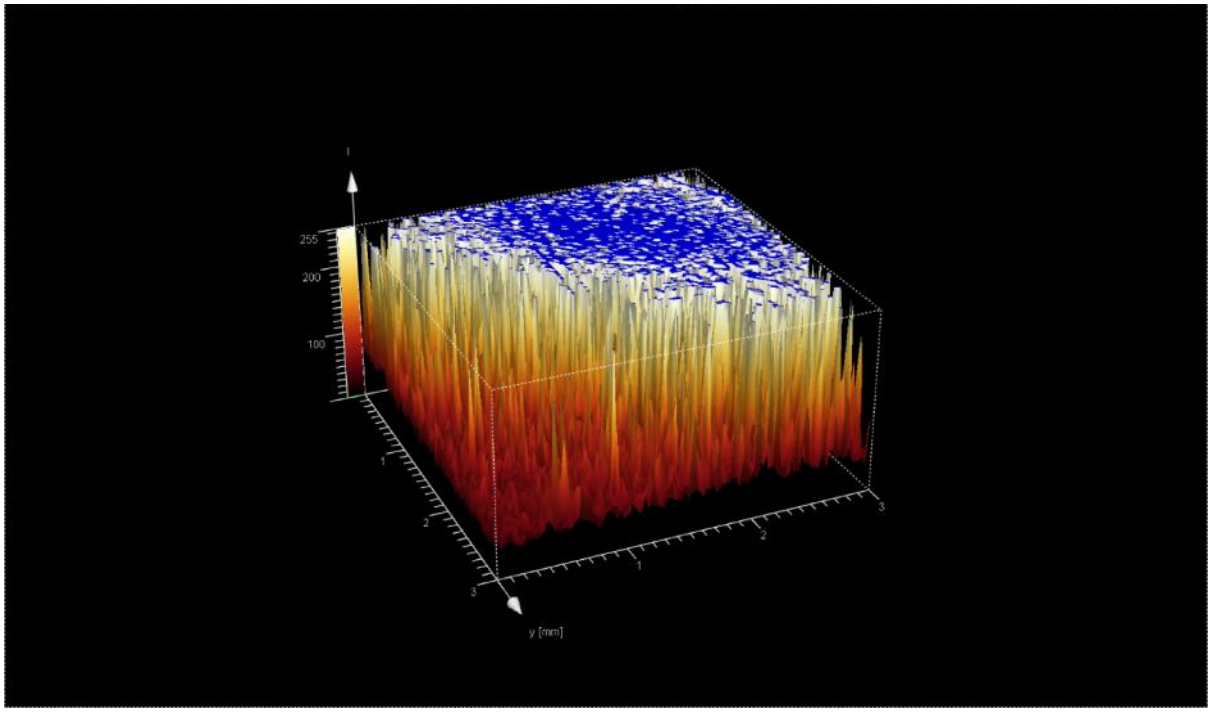

Figure 4.6-5 Topographic Image of High Parameter Laser Formed Sample

4.7 Results and Discussions

This section outlines the results and discussions which were generated from the experimental observations that were presented in the previous section.

1. Microscopic and Microanalysis

A report detailing the samples surface roughness parameters was acquired from the “quantify” tab. After selecting the quantify tab, a “draw line” and “generate report” tab appears. First select the “draw line” tab to draw two perpendicular lines on the image of the analysed samples. After performing this function, the image window then displays a green a purple line on the image of the sample. The green and the purple line on the image window indicates the sample area to be analysed. Three images for mild steel plates that are LBFormed using level 1, level 2, and level 3 LBF parameters are presented Figure 4.7-1, 4.7-2, and 4.7-3.

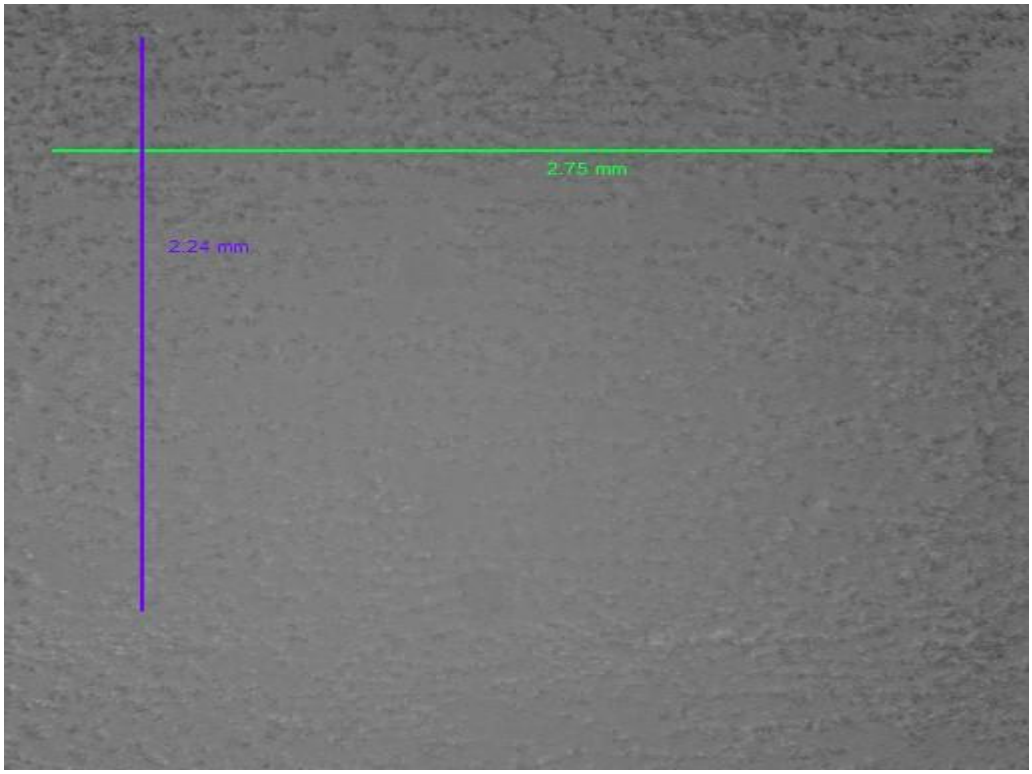

Figure 4.7-1 Perpendicular Lines on Low Parameter Laser Formed Sample Image

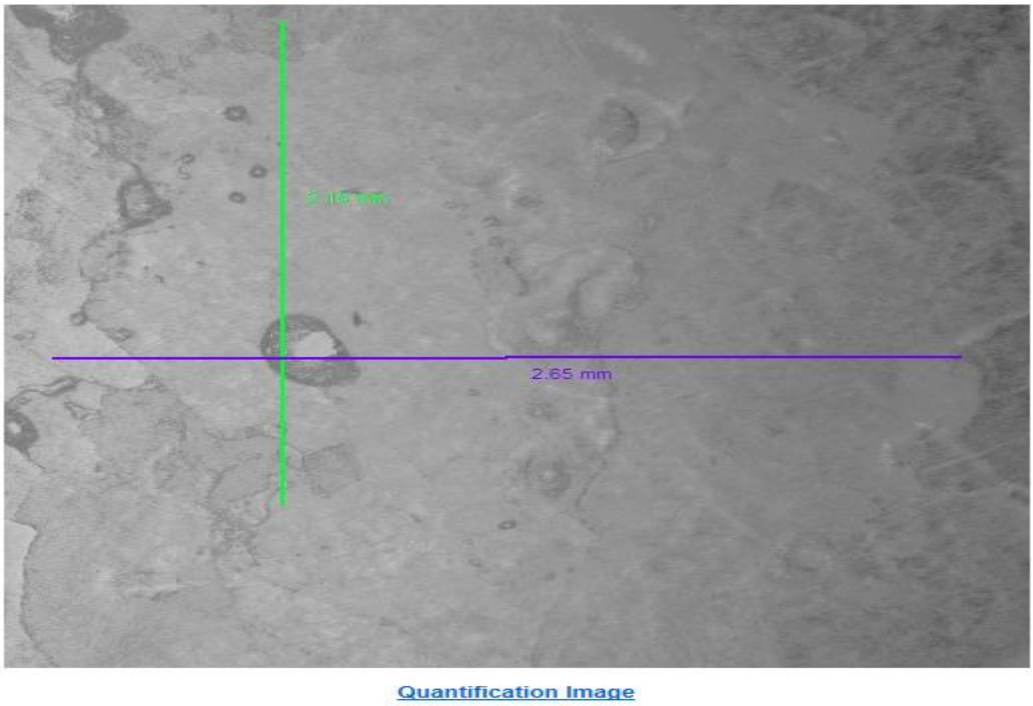

Figure 4.7-2 Perpendicular Lines on Medium Parameter Laser Formed Sample Image

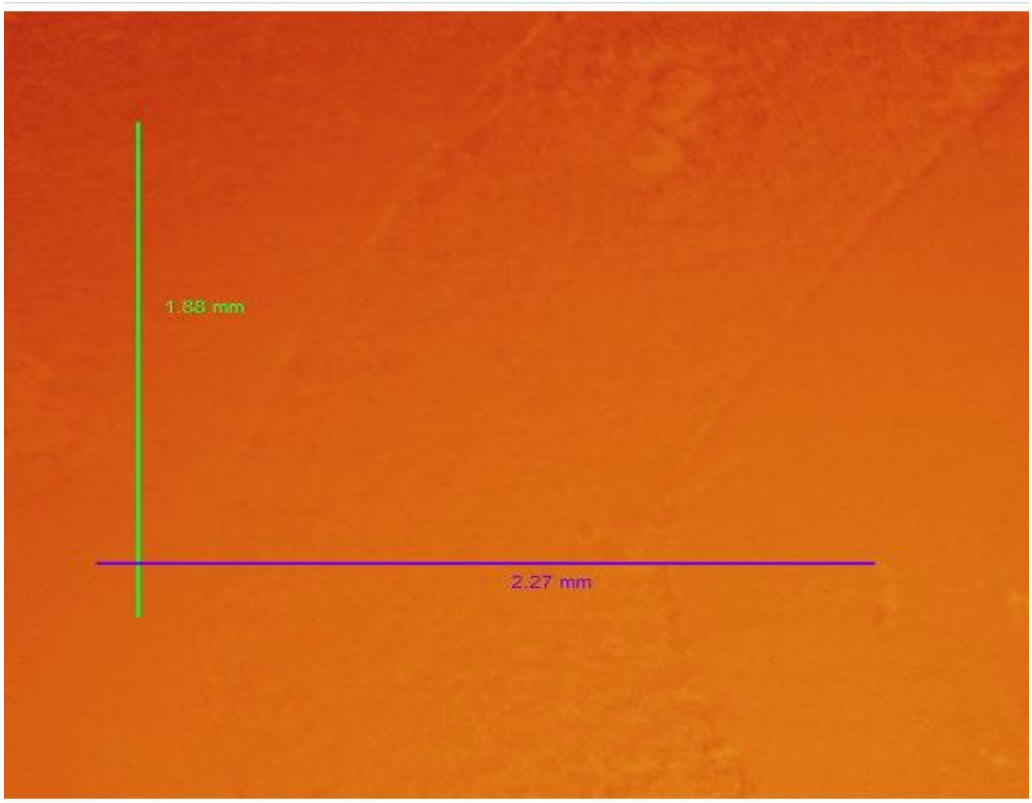

Figure 4.7-3 Perpendicular Lines on High Parameter Laser Formed Sample Image

To generate the report which analyses the sample, the following instruction were followed; select “generate report” ⟶ “Material” ⟶ “Create Topo Image” ⟶ “Preview” ⟶ “Apply”. After following this instruction the surface roughness over the area that is covered by the two perpendicular lines as shown in Figure 4.7-1, 4.7-2, and 4.7-3 is generated graphically and the results are shown in Figure 4.7-4, 4.7-5, and 4.7-6. The reason that the two lines are selected to run perpendicular to each other, is to enable the surface roughness to be analysed along the scan passages and across. Surface roughness is in micrometres and sample surface length being analysed for surface roughness is in millimeters.

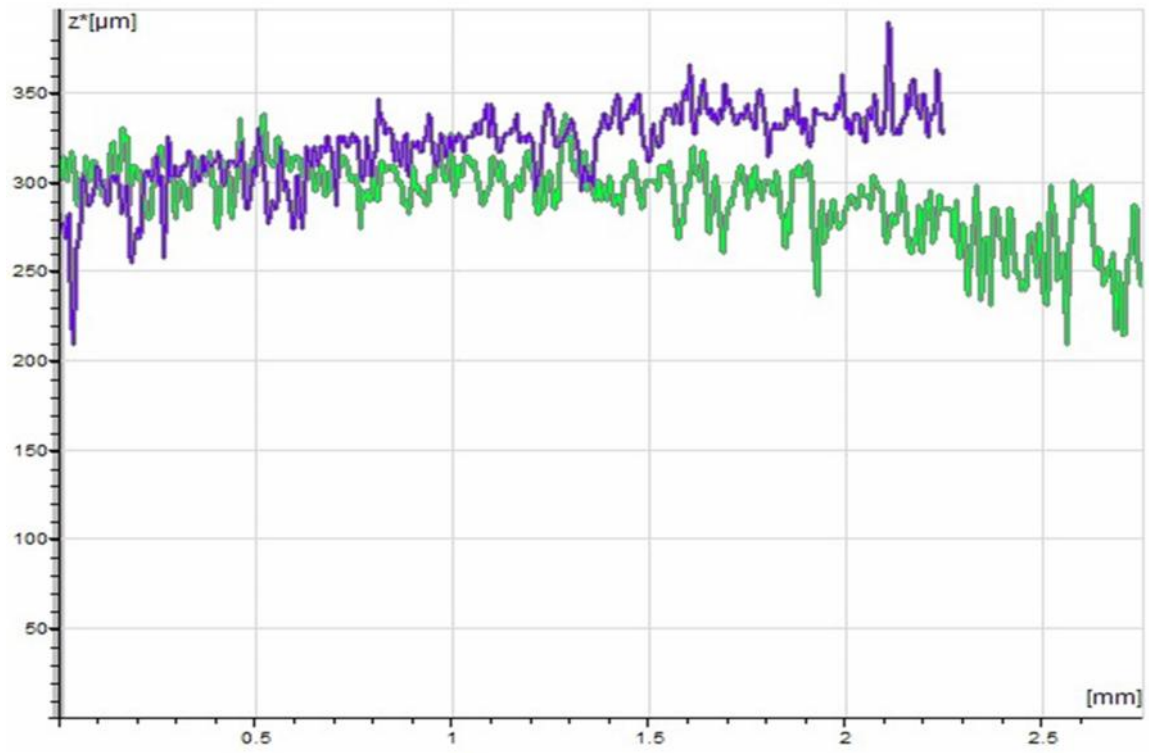

Figure 4.7-4 Graph of Surface Roughness for laser & non laser slots vs Length on Samples Formed using Low Laser Forming Parameters

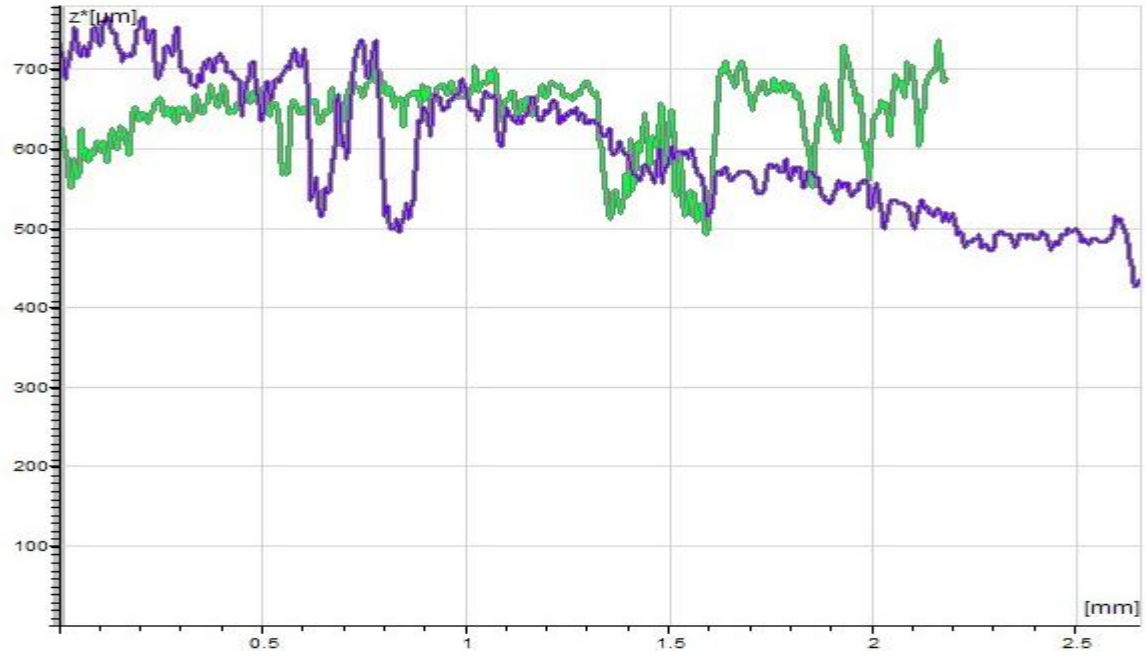

Figure 4.7-5Graph of Surface Roughness for laser & non-laser slots vs Length on Samples Formed using Medium Laser Forming Parameter

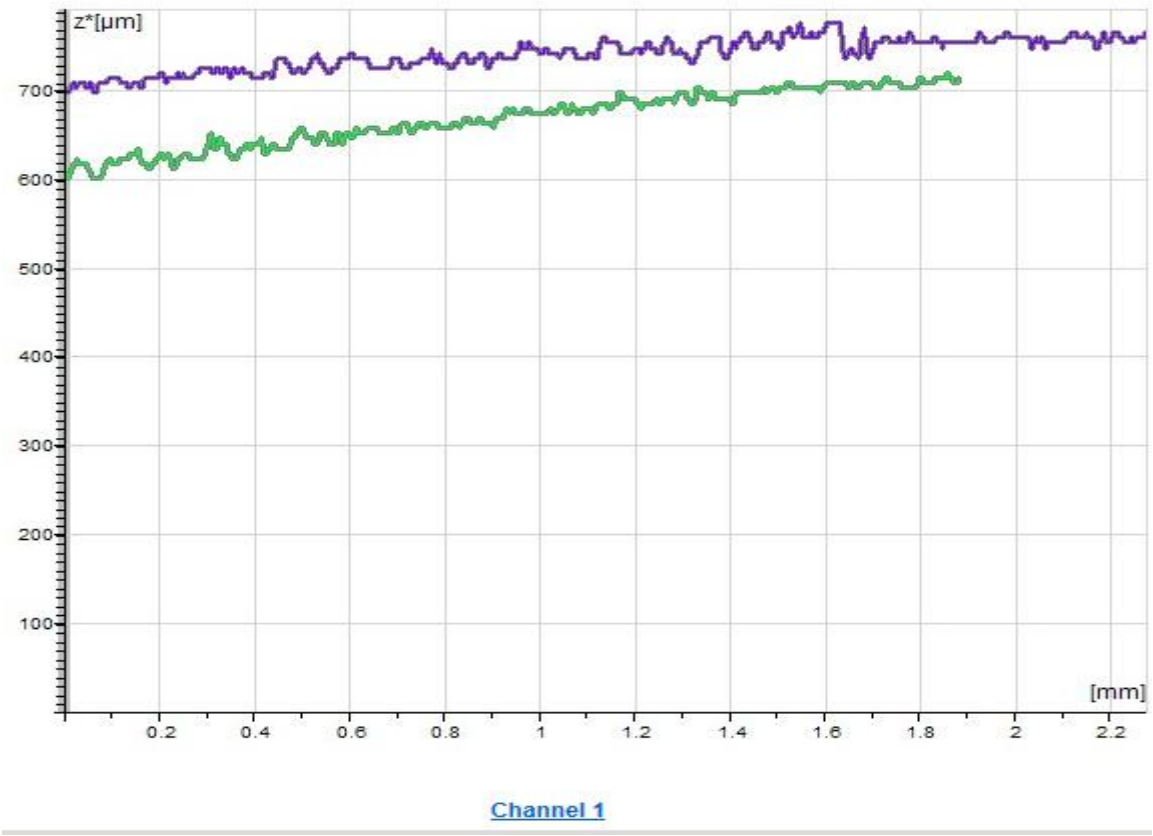

Figure 4.7-6 Graph of Surface Roughness for laser & non-laser slots vs Length on Samples Formed using High Laser Forming Parameter

In Figure 4.7-4 the green line on the curve starts by representing higher surface roughness results but decreases gradually. This is because the analysis on the green line begins on the LBFormed scan track and moves across, perpendicular to the non-LBFormed track. Whereas the purple line in the same Figure 4.7-4 continues to analyse the sample surface roughness along the laser scan track, hence the surface roughness it represents is high.

In Figure 4.7-5, the green line is analysing surface roughness along the LBFormed scanned track, hence the surface roughness results that is represented is high. On the other hand, the purple line in Figure 4.7-5 begins by showing higher surface roughness

but decreases gradually because the line is initially analysing the LBFormed scanned track, however; as it moves across or perpendicularly to a non-LBFormed track, it shows a decrease on surface roughness.

The purple line in Figure 4.7-6 gives sample surface roughness analyses along the LBFormed scan track, it is for this reason that the surface roughness results generated are higher compared to those analysed by the region covered by the green line. The green line is analysing the surface roughness along the non-LBFormed track. Similar characteristics to the surface roughness results that are generated by both the purple and the green line can be observed, although it is still clear that the purple line is analysing LBFormed scanned track. Due to the high laser beam intensity that is used to laser form mild steel AISI 1008 plates that are LBFormed using level 3 LBF parameters. It is this high laser beam intensity that causes damage even on non LBFormed scanned track, hence there are similarities on surface roughness [1, 5, 47, 49].

The results generated from Figure 4.7-4, 4.7-5, and 4.7-6 are further analysed in Tables 4.7-7, 4.7-8, and 4.7-9. The information that is generated in Tables 4.7-7, 4.7-8, and 4.7-9 was created by selecting the generate report window and then select table. In Table 4.7-7, 4.7-8, and 4.7-9 ROI 1 are the details of the surface roughness results generated by the area covered by the green line from Figure 4.7-4, 4.7-5, and 4.7-6, while ROI 2 are the details of the surface roughness results generated by the area covered by the purple line from the same Figure 4.7-4, 4.7-5, and 4.7-6. The columns in Tables 4.7-7, 4.7-8, and 4.7-9 are indicating the length that is analysed during the surface roughness analysis, the mean amplitude, max amplitude, min

amplitude, average deviation, standard deviation, and the variance for the surface roughness analysis. The standard deviation generated by each line is used as the average surface roughness analysis as indicated in each column of Tables 4.7-7, 4.7-8, and 4.7-9.

ROI	ROI 1	ROI 2
Length	2.75 mm	2.24 mm
Mean Amplitude	295.17 µm	326.38 µm
Max. Amplitude	345.18 µm	397.23 µm
Min. Amplitude	213.68 µm	213.68 µm
Average Deviation	15.99 µm	16.74 µm
Standard Deviation	20.81 µm	21.61 µm
Variance	433.13 µm²	467.16 µm²

Figure 4.7-7 Interpretation of Low Laser Parameter Sample Roughness from Figure 4.7-4

Channel 1

ROI	ROI 1	ROI 2
Length	2.18 mm	2.65 mm
Mean Amplitude	657.65 µm	812.31 µm
Max. Amplitude	732.00 µm	780.76 µm
Min. Amplitude	501.30 µm	435.58 µm
Average Deviation	34.48 µm	75.00 µm
Standard Deviation	45.36 µm	86.41 µm
Variance	2057.14 µm²	7466.23 µm²

Figure 4.7-8 Interpretation of Medium Laser Parameter Sample Roughness from Figure 4.7-5

Channel 1

ROI	ROI 1	ROI 2
Length	1.88 mm	2.27 mm
Mean Amplitude	681.73 µm	756.24 µm
Max. Amplitude	734.48 µm	792.33 µm
Min. Amplitude	613.04 µm	711.36 µm
Average Deviation	27.98 µm	16.21 µm
Standard Deviation	32.05 µm	18.03 µm
Variance	1027.05 µm²	326.75 µm²

Figure 4.7-9 Interpretation of High Laser Parameter Sample Roughness from Figure 4.7-6

Table 4.7-1 is the standard deviation for the three analysed samples from Tables 4.7-7, 4.7-8, and 4.7-9 which analyses the surface roughness results for mild steel AISI 1008 plate. The LBF parameters used to machine each sample are captured in Table 4.7-2 in Chapter 2. Each sample was marked to ensure that the corresponding LBF parameters used during its machining are not mixed with those of other samples. After LBF process, the sample bending measurement was done and the results were captured in Table 3.2-1, 3.2-2, and 3.2-3 in Section 3.2 of Chapter 3. The information for the sample surface roughness captured in Tables 4.7-7, 4.7-8, and 4.7-9 was done for the rest of the experimental samples. Both the information for bending measurement from Table 3.2-1, 3.2-2, and 3.2-3 and surface roughness results from Tables 4.7-7, 4.7-8, and 4.7-9 was recorded next to the corresponding LBF process parameter used to machine each samples and that information is consolidated in Table 4.7-2.

Table 4.7-1 Surface Roughness Standard Deviation Results

Laser Parameters	Scanned Track/ROI 1 (µm)	Non Scanned Track /ROI 2 (µm)
Low Laser Parameter Surface Roughness	20.81	21.61
Medium Laser Parameter Surface Roughness	45.36	86.41
High Laser Parameter Surface Roughness	32.05	18.08

Table 4.7-2 Taguchi L27 orthogonal array DOE used experimental parameter optimisation

Run #	Factors (Inputs)					Output 1	Output 2
	P (W)	B (mm)	V (m/s)	N	C (l/min)	Bending (mm)	Surface Roughness (µm)
1	1800	12	0,06	1	5	0,23	20,81
2	1800	12	0,06	3	10	1.01	10,31
3	1800	12	0,06	5	15	1,768333	10.11
4	2400	12	0,08	1	5	2,246667	16.84
5	2400	12	0,08	3	10	2,42833	21,61
6	2400	12	0,08	5	15	2,2733	40,55
7	3600	12	0,2	1	5	1,83833	41,63
8	3600	12	0,2	3	10	1,115	20,25
9	3600	12	0,2	5	15	0,07167	14,52
10	1800	15	0,08	1	5	0,34	29,37
11	1800	15	0,08	3	10	3,633333	18,08
12	1800	15	0,08	5	15	6,325	22,41
13	2400	15	0,2	1	5	8,145	12,73
14	2400	15	0,2	3	10	8,865	7,7
15	2400	15	0,2	5	15	8,37167	32,08
16	3600	15	0,06	1	5	6,69667	47,33
17	3600	15	0,06	3	10	3,96167	20,19
18	3600	15	0,06	5	15	0,345	20,65
19	1800	18	0,2	1	5	0,18	86,41
20	1800	18	0,2	3	10	8,013333	19,54
21	1800	18	0,2	5	15	13,72	17,83
22	2400	18	0,06	1	5	18,00167	10,6
23	2400	18	0,06	3	10	19,8017	45,36
24	2400	18	0,06	5	15	18,4333	35,86
25	3600	18	0,08	1	5	14,9517	25,27
26	3600	18	0,08	3	10	8,90833	13,29
27	3600	18	0,08	5	15	0,55	33,6

The FEI Quanta FEG-SEM microscope for this experiment was used to analyse sample surfaces and material composition for LBFormed samples. The point to point incremental function of the microscope was used to see material chemical composition. Material composition was compared to observe material property changes exists between samples LBFormed using the low, medium, and high laser

forming parameters. Figures 4.7-10, 4.7-11, and 4.7-12 are sample images that are machined using the low, medium, and high parameters taken with the Quanta microscope.

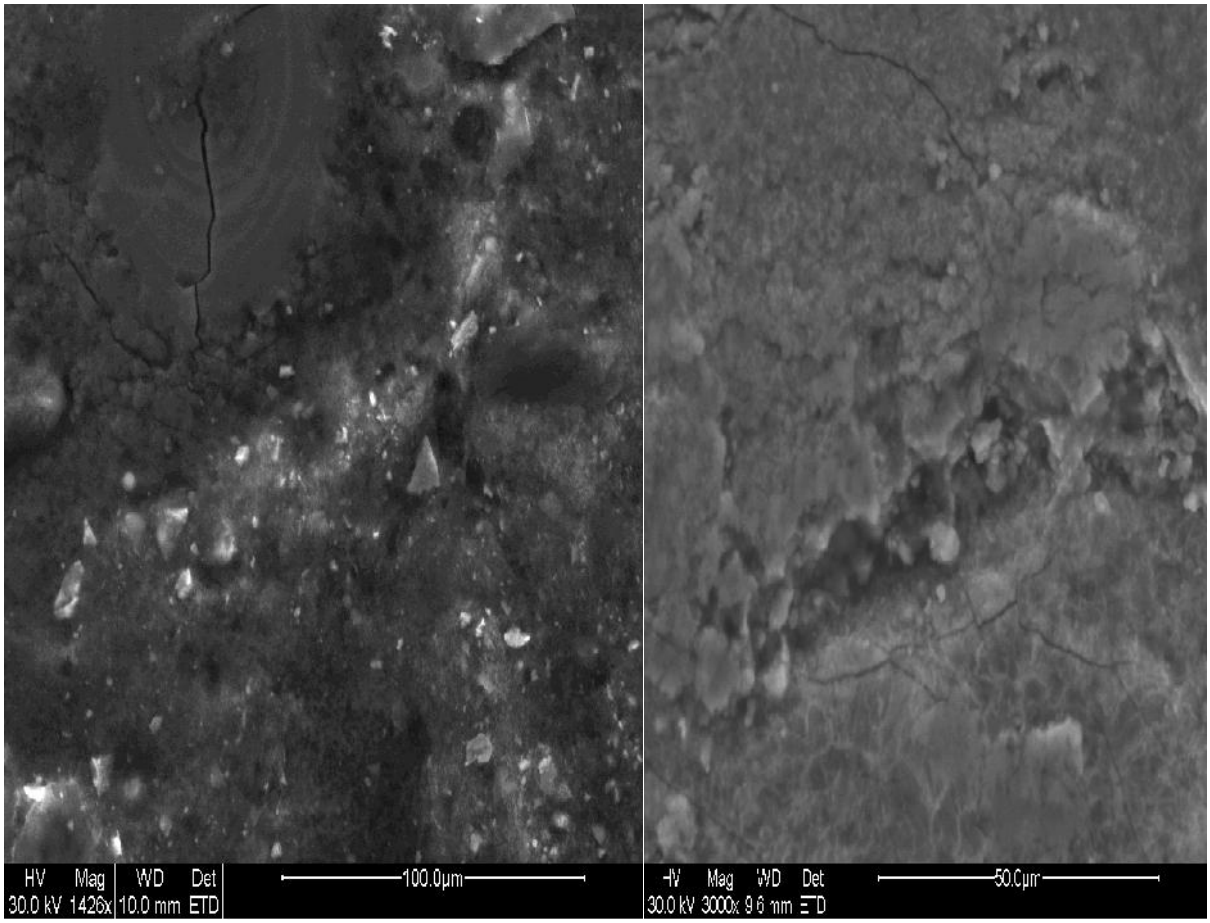

Figure 4.7-10 Low Parameter Laser Formed Sample Image from the Quanta Microscope

.

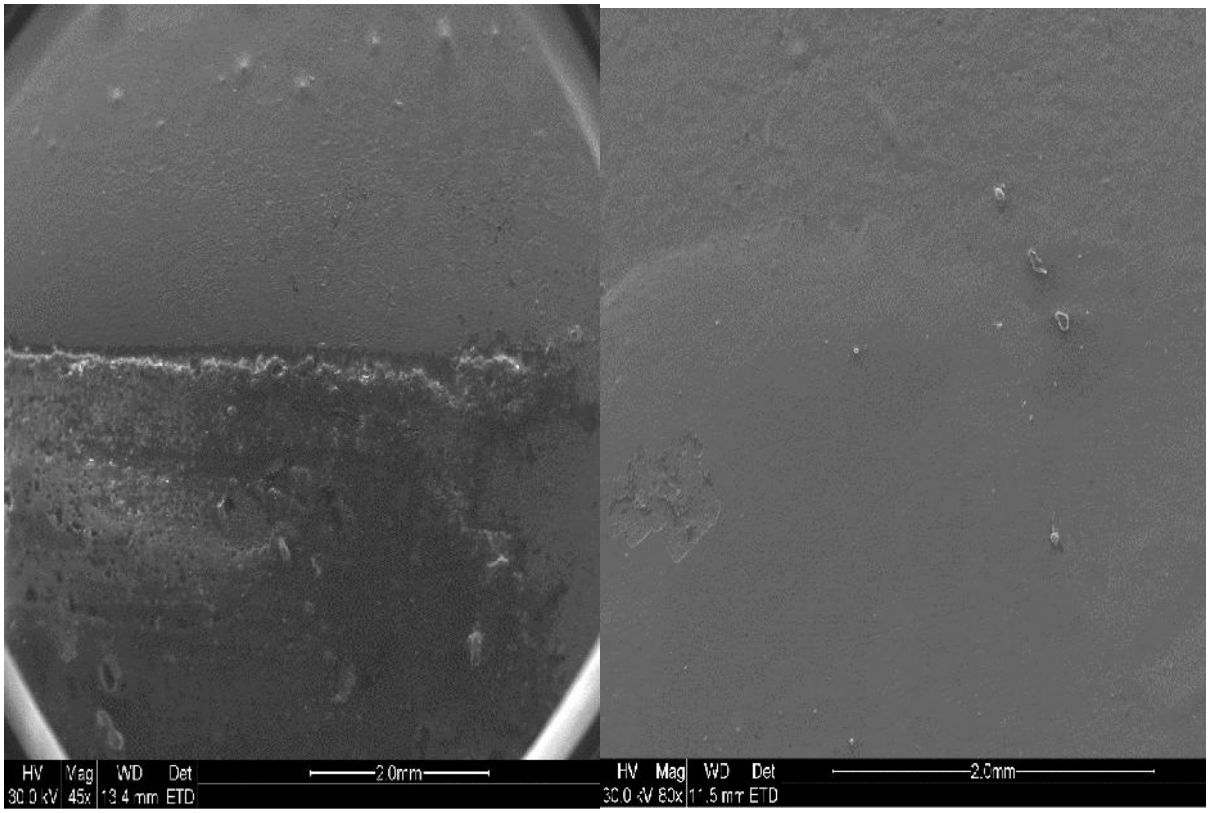

Figure 4.7-11 Medium Parameter Laser Formed Sample Image from the Quanta Microscope

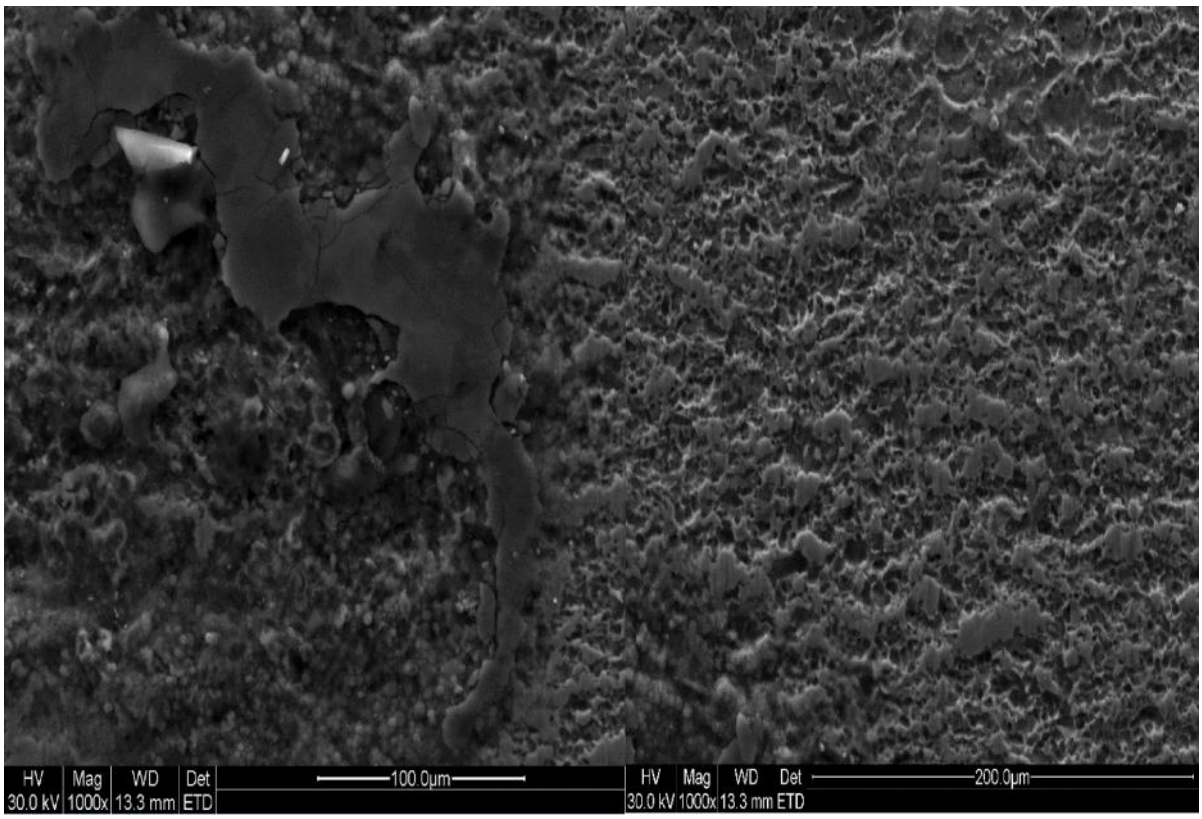

Figure 4.7-12 High Parameter Laser Formed Sample Image from the Quanta Microscope

The image displayed in Figure 4.7-10 is achieved under high magnification because of the smooth surface generated on samples LBFormed using low laser parameters. While the image presented in Figure 4.7-11 is achieved under very small magnification because of the clear non smooth surface. Magnification had to be increased to be more than that used for obtaining the image in Figure 4.7-11 for the image displayed in Figure 4.7-12 to be able to display rough surface on samples machined using high laser forming parameters. Therefore; it must be noted that the scale of the above results is not a primary factor, however the focus was of interest.

Figure 4.7-13 is the material chemical composition for random samples that were analysed using the Quanta SEM 200 microscope. The point to point incremental function of the microscope was selected for this function. The function comes up with the option to select the type of plot that is required by the user and whether or not the user wants to amplify to see clearly some of the elements which are present in smaller quantities on the samples.

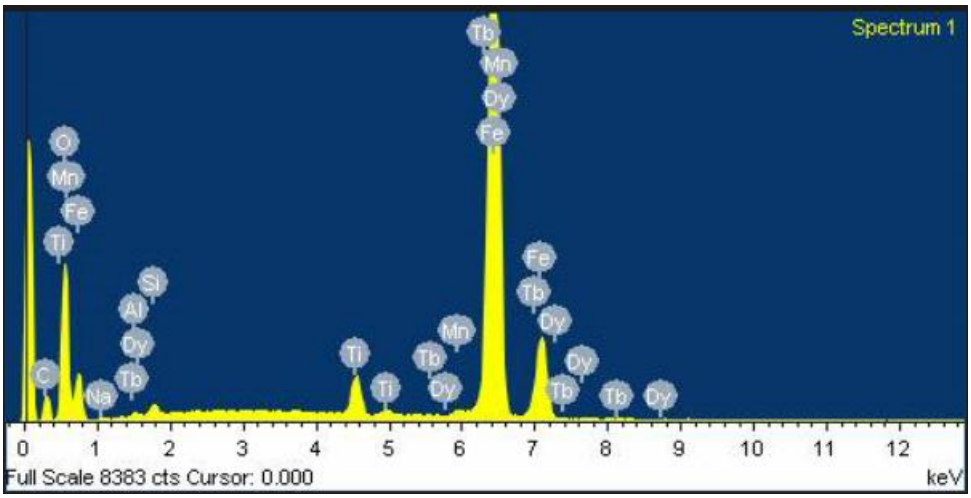

Figure 4.7-13 Sample Material Chemical Composition

An unrealistic presence of certain elements like Sodium Na, Chlorine Cl, etc. are noted in Figure 4.7-13. It is suspected that Sodium Chloride had fallen into the container where samples were stored in the lab.

2. Micro Hardness Test

Test on experimental samples were performed to determine the Vickers Hardness Number on LBFormed scanned and non-scanned track. The purpose for performing the micro-hardness test is to analyse if LBF has an impact on material micro-hardness as mentioned in Chapter 2. Fifty indentations were created on the surfaces of three mild steel AISI1008 plates that are LBFormed using level 1, level 2, and level 3 LBF parameters, using 0.5kg load with a dwell time of 15s. Spacing's between indentations that are called widths are left to create space between indentations. The widths are meant to avoid double indentation on top of other, which may result in inaccuracies in the results.

The width and the corresponding Vickers Hardness Number which is obtained after an indentation are recorded, and this information is presented in Table 4.7-3. An average of ten indentations on each LBFormed scanned and non- scanned track are performed and recorded in Table 4.7-3. This information is plotted in Vickers Hardness as function of Width in Figures 4.7-14, 4.7-15, and 4.7-16. It is important to note that the Vickers Hardness number does not have a scale and the width is in micro-meters. Also, the average Vickers Hardness Number for a scanned or non-scanned track is determined and recorded in Table 4.7-3 as well. Ten indentations per region selected for Vickers Hardness Test were carried out. This information was used to determine and compare the average percentage Vickers Hardness Numbers between LBFormed

scanned track and non-scanned track. The Vickers Hardness number is a measure of material hardness, therefore the greater the Vickers Hardness Number the harder it is the material.

Table 4.7-3 Results for Vickers Hardness Test Values for Samples LBFormed using Level 1, 2, & 3

				Load applied = 0.5kg							
				dwell time = 15s							
Sample 1				**Sample 2**				**Sample 3**			
Initial Width from the Edge of the Sample (µm)	**Width (µm)**	**Hardness (HV)**	**Batch Average for Column ©**	**Initial Width from the Edge of the Sample (µm)**	**Width (µm)**	**Hardness (HV)**	**Batch Average for Column (G)**	**Initial Width from the Edge of the Sample (µm)**	**Width (µm)**	**Hardness (HV)**	**Batch Average for Column**
Depth 84,38		142,8		**124.88**		181,1		**Depth 102,97**		180,20	
	182,14	139,4			272,08	181			203,78	168,50	
	283,65	139,4			350,96	167,1			328,04	177,80	
	410,62	145,5			431,62	171,6			443,22	176,50	
Non-Laser Formed Region	532,15	140,9	**140,681818**		611,92	174,6		**Laser Formed Region**	571,62	173,00	**165,57**
	652,92	143		**Non-Laser Formed Region**	737,72	178,3	**179,90909**		678,69	171,10	
	769,55	135,7			899,52	180,9			789,88	162,30	
	902,32	142,2			1023,22	184,3			901,42	163,50	
	1041,62	144,1			1238,44	178,7			1011,95	154,40	
	1167,96	141,5			1363,04	192,3			1141,78	128,40	
	1292,39	133			1482,59	189,1		Add	1200		
	1400			Add	700			**1st Jump to the new region on the material**	2341,78	177,40	
1st Jump to the new region on the material	2692,39	128,1		**1st Jump to the new region on the material**	2182,59	186,8			2464,01	169,90	
	2820,22	127			2312,94	184,8			2583,9	175,30	
	2941,73	135,7			2480,09	185,3			2709,81	182,00	
	3072,51	134,8			2596,18	181		**Laser Formed Region**	2834,4	140,10	**161,76**
Non-Laser Formed Region	3200,6	141,7	**133,93**	**Non-Laser Formed Region**	2725,07	176,8	**181,48**		2963,21	158,40	
	3326,53	132			2822,25	180,2			3077	156,70	
	3455,37	132,5			2962,11	169,3			3189,93	145,80	
	3560,64	135,4			3123,77	180,7			3302,53	136,40	
	3715,93	130			3283,5	179,9			3421,39	175,60	
	3858,11	142,1			3453,78	190		Add	1100		
	1100			Add	1250			**2nd Jump to the new region on the material**	4521,39	180,40	
2nd Jump to the new region on the material	4958,11	140,9		**2nd Jump to the new region on the material**	4703,78	184			4633,96	177,60	
	5096,19	139,2			4852,06	178,4		**Laser Formed Region**	4760,61	154,00	**167,88**
	5223,35	139,4			4989,82	172,8			4873,17	169,20	
	5346,04	138,7			5138,45	172,6			5000,88	158,20	
Non-Laser Formed Region	5454,04	139	**136,34**	**Non-Laser Formed Region**	5278,95	185,7	**180,7875**	Add	700		
	5581,17	141,7			5431,45	185,2		**3rd Jump to the new region on the material**	5700,88	183,70	
	5707,16	136,6			5588,34	184,9			5807,69	186,50	
	5817,05	141,1			5740,62	182,7		**Non-Laser Formed Region**	5896,56	192,90	**187,52**
	5944,37	136,6		Add	6840,62				5992,6	187,20	
	6070,44	110,2		**3rd Jump to the new region on the material**	7940,62	171,9			6092,15	187,30	
Add	1500				8082,73	161,5		Add	500		

3rd Jump to the new region on the material	7570,44	108,6			8235,64	162,2		**4th Jump to the new region on the material**	6592,15	174,30	
	7703,7	113,5			8406,52	159,3			669,3	183,50	
	7815,06	107,6			8553,5	152,8		**Non-Laser Formed Region**	6785,09	183,90	**180,64**
	7940,83	108,3		**Laser Formed Region**	8708,94	149,7	**159,73636**		6893,12	185,70	
	8061,7	112,2			8877,74	156,6			6992,54	175,80	
	8170,75	112,3			9036,33	156,4		Add	400		
Laser Formed Region	8293,77	107,7	**109,515385**		9180,18	164,8		**5th Jump to the new region on the material**	7392,54	182,70	
	8416,01	104,9			9337,72	159,9			7512,57	181,60	
	8536,59	109,6			9478,85	162		**Non-Laser Formed Region**	7615,79	181,70	**181,43**
	8650,44	109,9		Add	900				7735,31	179,70	
	8762,56	109,8		**4th Jump to the new region on the material**	10378,85	167,9		Add	450		
	8880,7	109,7			10552,35	161,7		**6th Jump to the new region on the material**	8185,31	176,60	
	9003,61	109,6		**Laser Formed Region**	10719,93	157,4	**162,18**		8298,31	174,00	
	700				10874,71	157		**Non-Laser Formed Region**	8424,84	178,70	**178,44**
4th Jump to the new region on the material	9703,61	107,7			11036,09	166,9			8542,93	175,60	
	9860,06	109,5		Add	700				8657,63	187,30	
	9995,15	103,2		**6th Jump to the new region on the material**	11736,09	166,6		Add	420		
Laser Formed Region	10125,4	104,7	**105,866667**		11882,12	166,9		**7th Jump to the new region on the material**	9077,63	175,60	
	10250,2	105,2		**Laser Formed Region**	12036,35	158,9	**164,06**		9185,38	184,70	
	10383,4	104,9			12194,38	166,3			9309,48	185,80	
Total HV Average		**126,182**			12346,76	161,6		**Non-Laser Formed Region**	9426,45	186,90	**187,52**
				Total HV Average		**172,568**			9552,11	196,30	
									9674,91	195,80	
								Total HV Average		**173,93**	

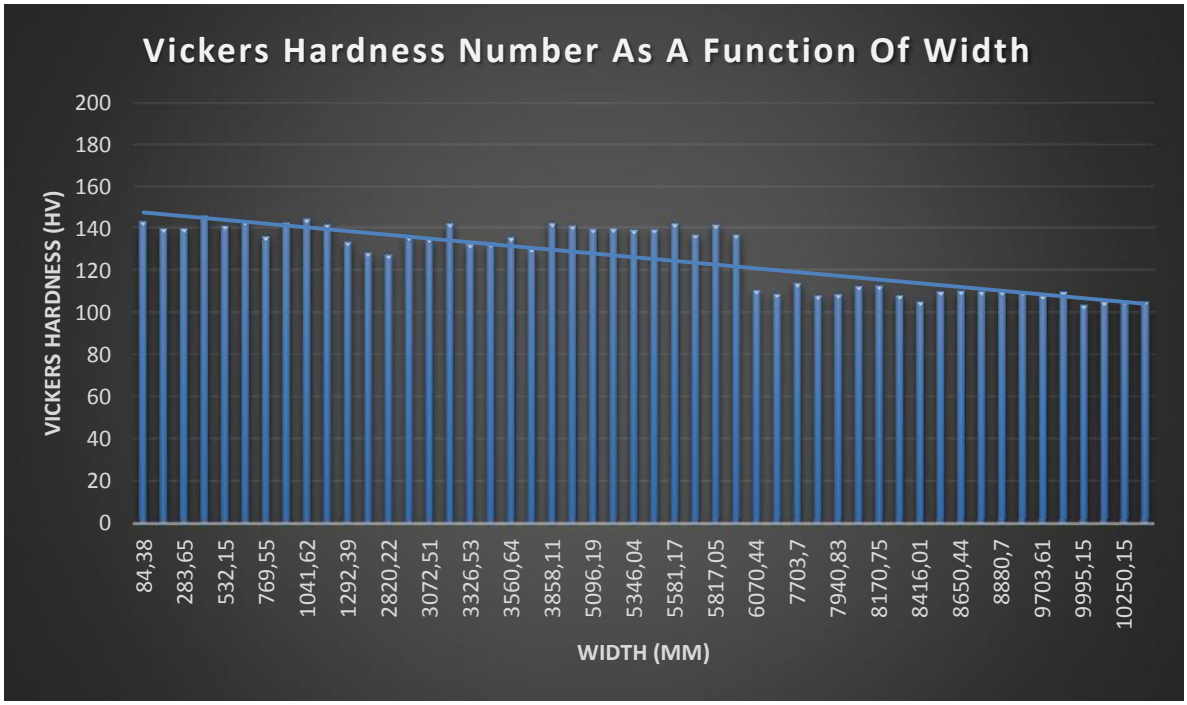

Figure 4.7-14 Vickers Hardness Number as A Function of Width (µm) for Sample LBFormed using Level 1 LBF Parameters (Sample 1)

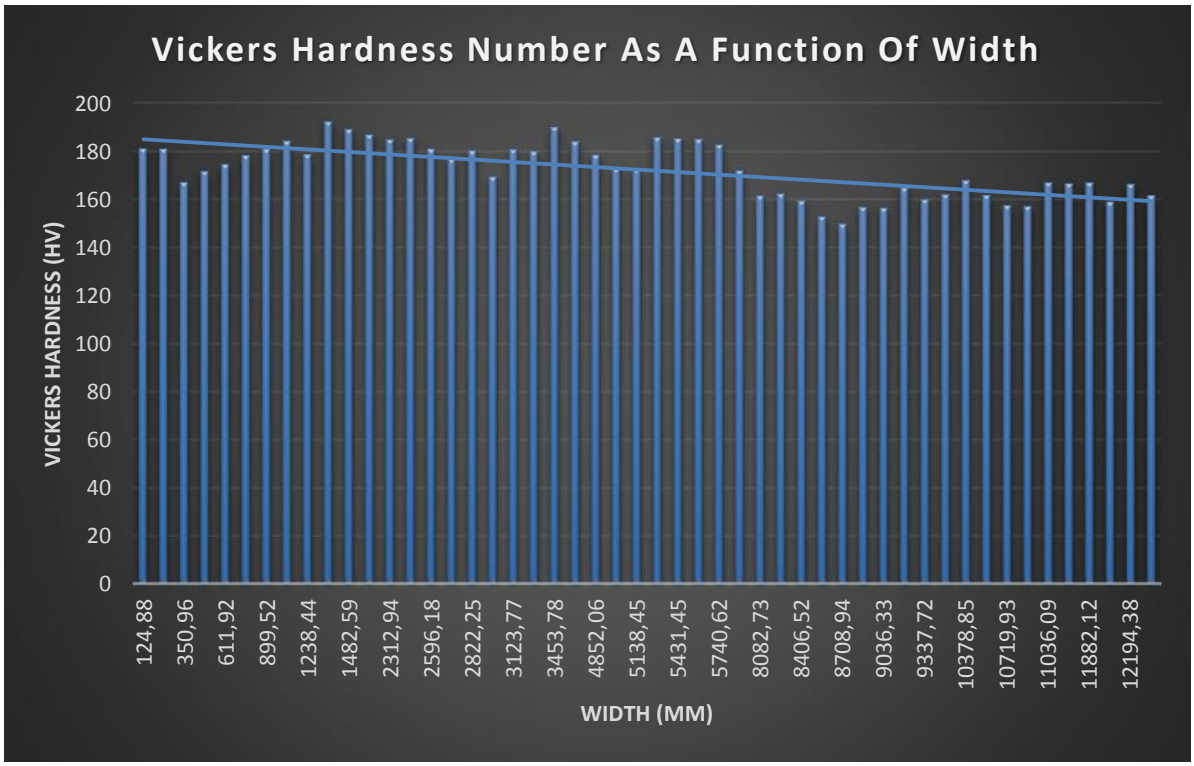

Figure 4.7-15 Vickers Hardness Number as A Function of Width µm) for Sample LBFormed using Level 2 LBF Parameters (Sample 2)

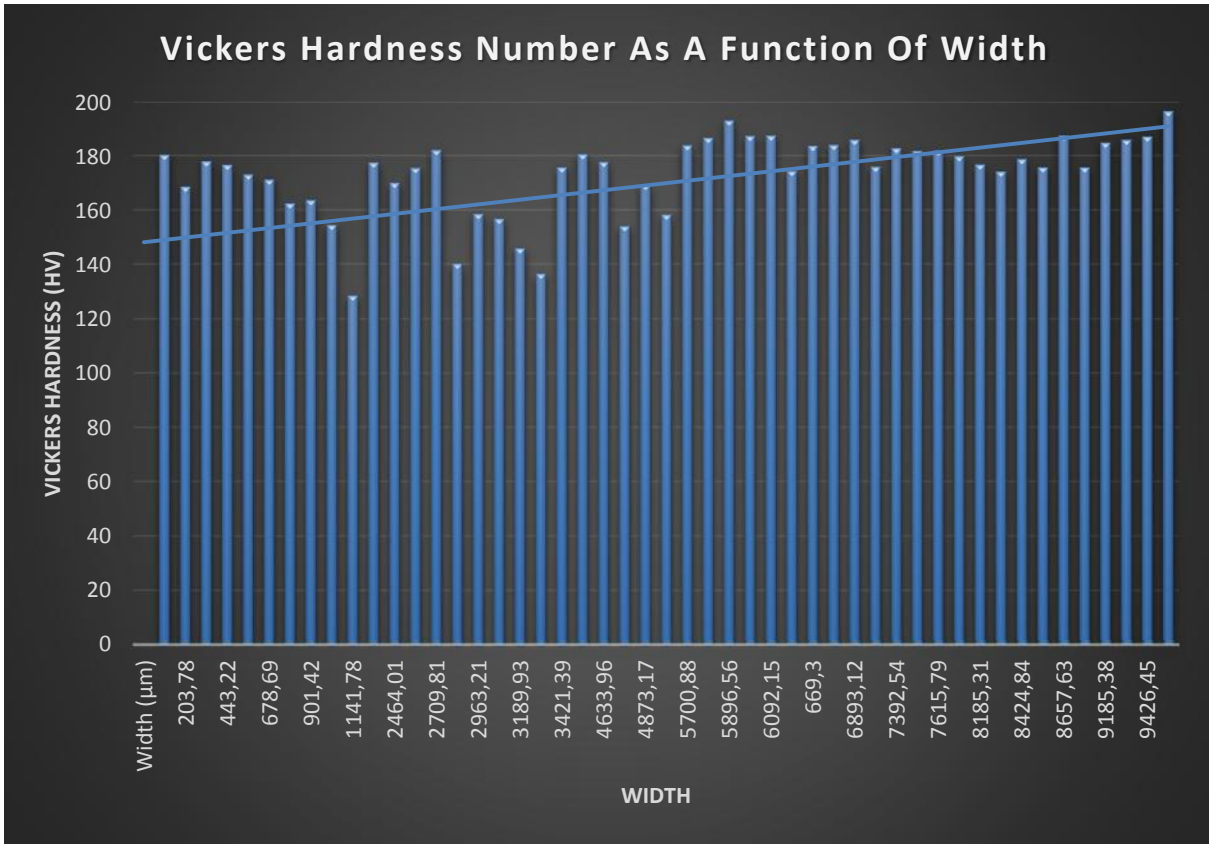

Figure 4.7-16 Vickers Hardness Number as A Function of Width (µm) for Sample LBFormed using Level 3 LBF Parameters (Sample 3)

Figures 4.7-14 is the Vickers Hardness Number as a function of Width plot for a sample machined using level 1 LBF parameters. Indentations on the LBFormed scanned track are on the widths which are from 84.38 µm – 6070.44 µm as recorded while performing the experiment. While corresponding indentations taken on LBFormed scanned track are on the widths which are from 7703.7µm – 10250.15µm.

Figures 4.7-15 is also the Vickers Hardness Number as a function of Width plot for a sample machined using level 2 LBF parameters. Indentations on the LBFormed scanned track are on the widths which are from 124.88 µm – 5740.62µm. While corresponding indentations taken on LBFormed scanned track are on the widths which are from 8082.73µm – 12194.38µm.

Figures 4.7-16, is also the Vickers Hardness Number as a function of Width plot for a sample machined using level 3 LBF parameters. Indentations on the LBFormed scanned track are on the widths which are from 203.78 µm – 487.31µm in width. While corresponding indentations taken on LBFormed scanned track are on the widths which are from 5700.88 – 9426.45µm. Reference to his information can be referenced in Table 4.7-3.

Variation in Vickers Hardness Number between the LBF scanned and non-scanned paths is visible in Figure 4.7-14. This is suspected to be caused by the high laser heat intensity that the laser introduced in the scanning path [59]. Whereas slight variation is evident in Figure 4.7-15 between the LBF scanned and non-scanned path. This is caused by the similar effect to that discussed with the results achieved from Figure 4.7-14. The damage on surface roughness on the mild steel plate for both the LBFormed scanned and non-scanned track has created the Vickers Hardness results in Figure 4.7-15 to be similar for both the scanned and non-scanned track [59]. This is caused by the high LBF parameters used, which then high LBF heat intensity of the beam introduced to the material affects the neighbouring region which is called the non-scanned track [59].

Equation 5.1 illustrates how the averages for Vickers Hardness Numbers for LBFormed scanned and non-scanned tracks were obtained for samples machined using level 1, level 2, and level 3 LBF categories. While equation 23 illustrates how percentage averages were being determined for the sum of each region. The results for the average percentage Vickers Hardness Numbers are compared analysed between regions tested for micro-hardness.

For Sample 1

The averages HV values for Laser & Non LBFormed regions for sample 1 *is* HV_{aveLF1}

$$HV_{aveLF1} = \frac{(110+106)}{2} = 108 \quad \ldots (5.1)$$

& Average HV value for non – laser formed slots for sample 1 *is* $HV_{aveNLF1}$

$$HV_{aveNLF1} = \frac{(141 + 134 + 136)}{3} = 137$$

$$\therefore \%\ average\ for\ average\ HV_{aveLF1} = \frac{HV_{aveLF1}}{HV_{aveLF1}+HV_{aveNLF1}} = \frac{108}{(108+137)} = 44\% \ldots\ldots\ldots (23)$$

$$\&\ \%\ average\ for\ average\ HV_{aveNLF1} = \frac{HV_{aveNLF1}}{HV_{aveLF1} + HV_{aveNLF1}} = \frac{137}{(108 + 137)} = 56\%$$

NB *This means the* $HV_{aveNLF1}$ *is* 15% *more than* HV_{aveLF1}

For Sample 2

Use 5.1 *to get the average for Laser & Non – Laser formed regions*

$$\therefore HV_{aveLF2} = 161{,}99$$

$$\& HV_{aveNLF2} = 180.72$$

Use (5.2) *to get* $\%\ average\ for\ HV_{aveLF2} = 47\%$

$$\%\ for\ HV_{aveNLF2} = 53\%$$

NB *This means the* $HV_{aveNLF2}$ *is* 6% *more than* HV_{aveLF2}

$For\ Sample\ 3$

$$Again\ \ 5.1\ \ is\ used\ to\ get\ HV_{aveLF3} = 126$$

$$\&\ HV_{aveNLF3} = 174$$

$$W\square ile\ \ 5.2\ \ is used\ to\ get\ t\square e\ \%\ average\ for\ HV_{aveLF3} = 42\%$$

$$\&\ \%\ for\ HV_{aveNLF3} = 58\%$$

NB This means the $HV_{aveNLF3}$ is 16% more than HV_{aveLF3}

The total average Vickers Hardness $HV_{avetotal}$ is the combination of all the average HV values for sample and that value is reflected at the bottom of Table 9.1-1.

$$\therefore T\square e\ total\ average\ Vickers\ Hardness\ \ HV_{avetotal1}\ for\ sample\ 1\ HV_{avetotal1} = 126$$

$$\&\ t\square e\ total\ average\ Vickers\ Hardness\ \ HV_{avetotal2}\ for\ sample\ 3\ HV_{avetotal2} = 173$$

$$\&\ t\square e\ total\ average\ Vickers\ Hardness\ \ HV_{avetotal3}\ for\ sample\ 3\ HV_{avetotal3} = 174$$

$$\boldsymbol{NB}: HV_{avetotal2}\ is\ \ 47\ more\ HV\ number\ t\square an\ HV_{avetotal1}$$

$$\&\ HV_{avetotal3}\ is\ \ 48\ more\ HV\ number\ t\square an\ HV_{avetotal1}$$

The average percentages for Vickers Hardness Numbers is determined using equation 23. The average percentage values obtained for Vickers Hardness Numbers using equation 23 between LBFormed scanned and non-scanned track are put in Table 4.7-4 and Figure 4.7-17 for sample LBFormed using level 1 LBF parameters. The corresponding average percentage values that are obtained using equation 23 for

samples LBFormed using level 2 and level 3 LBF parameters are captured in Tables 4.7-2 and 4.7-3, whilst the information is plotted in Figure 4.7-18 and 4.7-19 respectively. The use of pie charts in Figures 4.7-17, 4.7-18 and 4.7-19 is meant to give better analyses for the information presented from Tables 4.7-4, 4.7-2 and 4.7-3.

Table 4.7-4 Table 5.1 Average percentage HV on Low Laser Formed Sample Parameter

Ave percentage HV on Non-Laser Scanned Track	Ave percentage HV on Laser Scanned Track
56	44

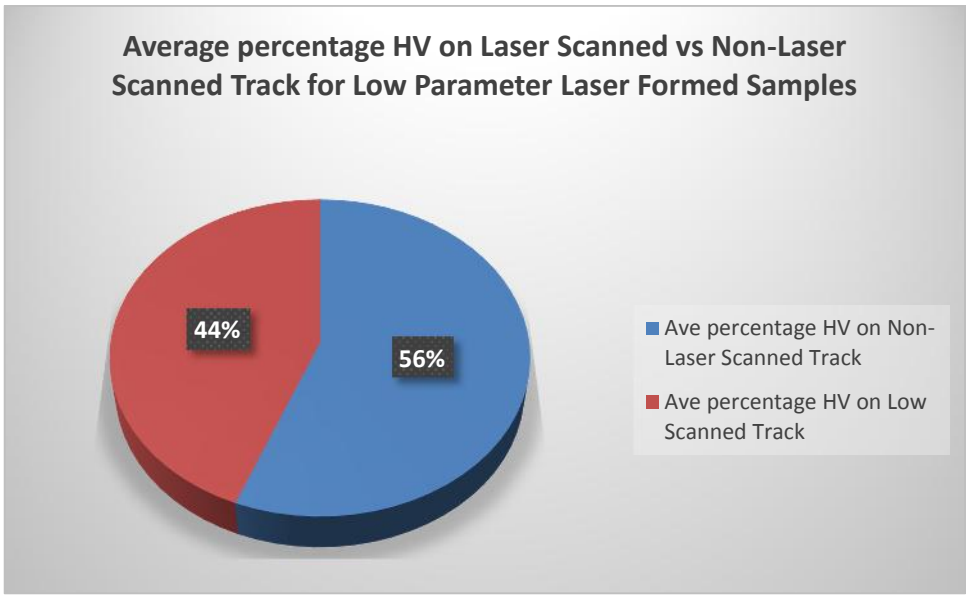

Figure 4.7-17 Average percentage HV on Laser Scanned vs Non-Laser Scanned Track for Low Parameter Laser Formed Samples

Table 4.7-5 Table 5.2 Average percentage HV on Medium Laser Formed Sample Parameter

Ave percentage HV on Non-Laser Scanned Track	Ave percentage HV on Laser Scanned Track
53	47

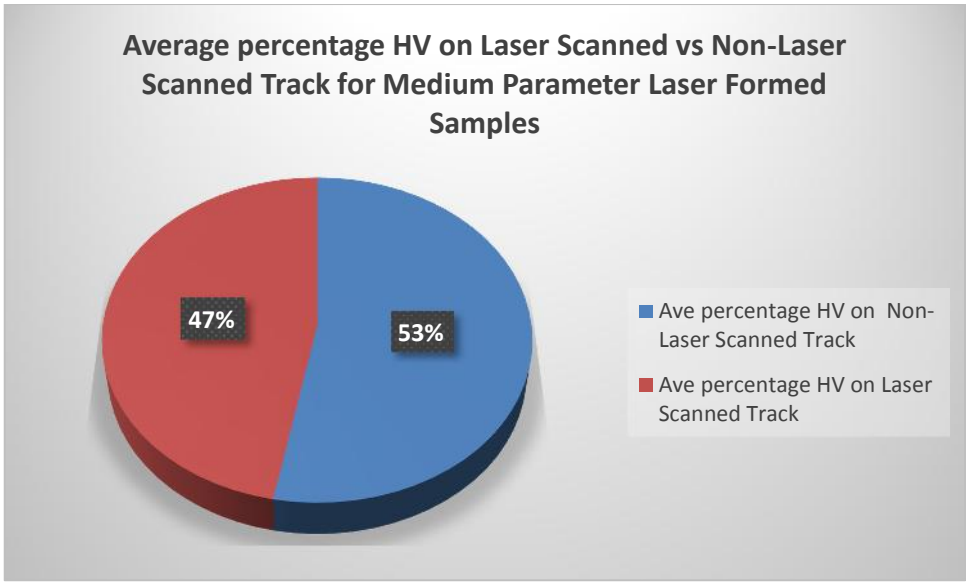

Figure 4.7-18 Average percentage HV on Laser Scanned vs Non-Laser Scanned Track for Medium Parameter Laser Formed Samples

Table 4.7-6 Table 5.3 Average percentage HV on Low Laser Formed Sample Parameter

Ave percentage HV on Non-Laser Scanned Track	Ave percentage HV on Laser Scanned Track
58	42

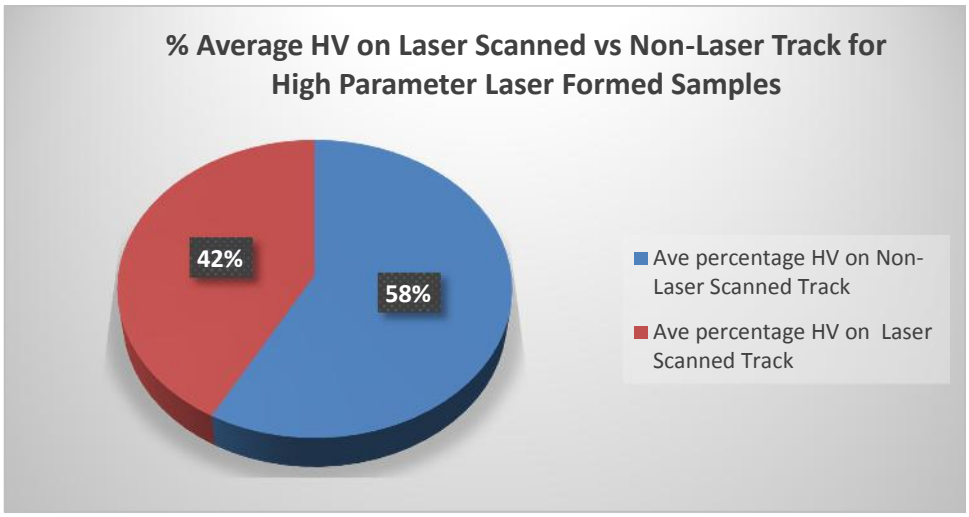

Figure 4.7-19 Average percentage HV on Laser Scanned vs Non-Laser Track for High Parameter Laser Formed Samples

4.8 Conclusion

The conclusions in this section are drawn from the results of the microscopic analysis using the two microscopes on samples being investigated, as well as from the micro hardness testing. The Confocal microscope is good in analysing material surface roughness and material profile [57]. The topographic images are presented in Figures 4.6-3, 4.6-4, and 4.6-5 in Section 4.6. Figures 4.6-3, 4.6-4, and 4.6-5 of Section 4.6 shows a slight difference on sample analysis between samples which are LBFormed using level 1 and level 2 LBF parameters. The topographic images for samples LBFormed using level 3 LBF parameters are displaying a high pitched image when compared to those derived from level 1 and level 2.

More analysis was done by creating virtual images generated using the microscope to enable to quantify and detail the surface roughness on LBFormed samples. The purple and the green lines were observed to be starting more or less at the same point from the plots in Figure 4.7-4, 4.7-5, and 4.7-6. The reason for this behaviour is that the starting point is where the two lines intersect in Figure 4.7-4, 4.7-5, and 4.7-6. This means that the surface roughness analysis is started at the same region which is the point of intersection, hence the behaviour of the two lines on the curves starts more or less at the same point. Thereafter, the pattern of the two lines begins to change as they branch as one line will be analysing LBFormed scanned track and the other will be analysing non-scanned track. The purple line is giving analysis on the LBFormed scan track, while the green line branches to give analysis to the non-scanned track.

The following conclusion can be drawn from the plots presented in Figure 4.7-4, 4.7-5, and 4.7-6. The surface damage caused by LBF on the material is not only limited to the LBF scanned track. This is concluded by the observations made from the damage on the immediate non-scanned tracks of LBFormed samples. The damage on the non-scanned track is observed to be proportional to the rate of the LBF parameters used when LBF on the scan track occurred [58, 59]. The damage in the non-scanned region on the sample surface is clearly observed in the analysis shown in Figure 4.7-6, which is the sample surface roughness results for samples machined using high LBF parameters. The results shown in Figure 4.7-7, 4.7-8, and 4.7-9 verifies previous discussion about Figure 4.7-4, 4.7-5, and 4.7-6. The standard deviation for surface roughness results in Table 4.7-1 illustrates correlation between LBFormed scanned and non-scanned track.

Figure 4.7-10, 4.7-11, and 4.7-12 are sample surface images taken using a Quanta microscope. Figure 4.7-10 is an image of a sample that is LBFormed using level 1 LBF parameters. The image focus for Figure 4.7-10 was obtained under high magnification as expected due to the relatively smooth sample surface. Figure 4.7-11 is an image obtained under relatively low focused magnification. The image is showing a fairly rough surface for samples machined using level 2 LBF parameters. On the other hand, Figure 4.7-12 is the image for a sample that was LBFormed using level 3 LBF parameters. Figure 4.7-12 is presenting a rough surface when compared those presented in Figures 4.7-10 and 4.7-11.

The effectiveness of SEM very narrow electron beam has an ability to generate images that have a large depth. Its three-dimensional appearance is useful in picking up

material composition for samples as in Figures 4.7-13 [60]. The scanning of the material for this microscope is a point to point incremental scanning, where the microscope selects certain points on the sample to analyse elements which are available in those selected points [60]. It is for this reason why some of the elements are not appearing in small quantities in in Figure 4.7-13. Furthermore; certain elements makes a very small percentage of the elements present in the chemical composition of the sample. Therefore, it is for this reason that some of the elements are amplified, to enable them to appear on the point to point charts.

Micro hardness results demonstrated that laser effects do not only influence material surface roughness, but also affects material hardness [61]. The evidence from the Vickers Hardness Test shows that LBFormed scanned tracks have lower Vickers Hardness Numbers, compared to those analysed in non-LBFormed scanned tracks. It is observed from the analysis done Section 4.7 that LBF reduced the average Vickers Hardness Number on LBFormed scanned track/region by 15.5% when compared to a non-scanned track/region for sample 1, which is the sample that is LBFormed using level 1 LBF parameters. A 6% reduction on Vickers Hardness Number is recorded for samples machined using level 2 LBF parameters and 16% reduction in Vickers Hardness Number is recorded for samples machined using level 3 LBF parameters. The small difference in Vickers Hardness Number between LBFormed scanned and non-scanned track is found on sample LBFormed using level 2 LBF parameters. This is suspected to be contributed by similarities on the surface areas on both the LBFormed scanned track and non-scanned track for sample 2. Meaning that the beam effects is not only limited on laser scan track, but it also effects the non-laser scan track because of its intensity [59-61].

The plot of Vickers Hardness Number as a function of Width in Figures 4.7-14, 4.7-15, and 4.7-16 follow the same trend for all samples tested and only differ in magnitude of the Vickers Hardness Number that is achieved. Where a sample machined using level 1 LBF parameters have the smallest overall Vickers Hardness Number. On the other hand, sample machined using level 2 LBF parameters have an overall medium Vickers Hardness Number. While sample machined using level 3 LBF parameters demonstrates the overall highest Vickers Hardness Number respectively. A conclusion that can be drawn from this analysis is that, samples machined using level 3 LBF parameters are harder and more brittle. These results also illustrates that, LBFormed samples follow the same behaviour irrespective of the proportion of the LBF parameters used and the only difference is in the magnitude of the parameters used, which then have an effect on sample bending, surface roughness, and micro-hardness structure [59-61]. In summary, when laser forming parameters are increased, there is a reduction on material hardness [61].

Chapter 5

Response Surface Method (RSM)

This chapter focuses in processing the results obtained in previous chapters, where the Taguchi DOE was used in a selection of a combination of initial input process parameters. The RSM is used to interpolate the derived input process parameters and to provide a graphical representation of the behaviour of the final results. The main tool which was used is an algorithm called modeFRONTIER. A step by step process in using modeFRONTIER is presented in this chapter.

5.1 modeFRONTIER

The response surface was created using modeFRONTIER v4.3.1 multi-objective optimisation software. The procedure that was used to generate the response surface, and the new set of 'virtual' full-factorial results, is explained. The same procedure was repeated numerously throughout the remainder of the thesis using the step-by-step format that follows. Note that items which are written in bold font refer to actions within the software.

1. Create a spreadsheet using Microsoft Excel that has the Taguchi OA and the response values (such as Table 2.3-2).

2. Open modeFRONTIER.
3. Under the Assessment toolbar choose **Open Table Creation Tool**.

   The following three steps are illustrated in Figure 5.1-1:

4. Import the data from the spreadsheet that was created.
5. modeFRONTIER then asks the user to define which of the columns, from the imported data table, are the inputs (factors) and the outputs (responses). In this case the inputs are the power, beam diameter, velocity, number of scans, and cooling flow. The outputs are the bending and surface roughness.
6. **Next** was selected on the following prompts until the software was directed to the 'Design Space' window of the software. The imported data should show as a table within the 'Design Space'.

Table 5.1-1 Screenshots to show the modeFRONTIER table creation tool; the definition of the inputs (factors) and outputs (response) and the table that is generated in the Design Space

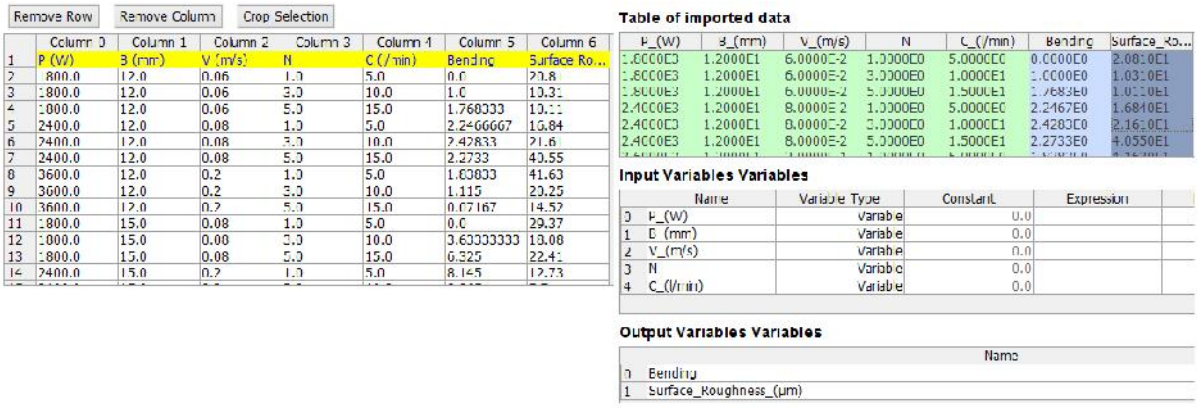

   a. Once again the Assessment toolbar was chosen, but this time choose **Open RSM Panel** of the software.

The three steps that will follow are illustrated in Figure 5.1-1

b. Within the RSM Panel **Multiple RSM** and the imported table were selected

c. The next window prompted the user to make a selection on the inputs and outputs to include in the response surface. In this case, all of them. It also asks to select which algorithm to use in order to generate the response surface. For all of the response surfaces that were generated for this research the Kriging algorithm was used. The reason for this is that it consistently produced the curve fit with the lowest residuals, refer to Figure 5.2-2 [62]

d. Generate the Flood Power Kriging response surface using the default algorithm settings. Once the response surface is created the user is re-directed to the ’Design Space’. In the ’Explorer’ window, within the ’Design Space’, there should now be a response surface icon.

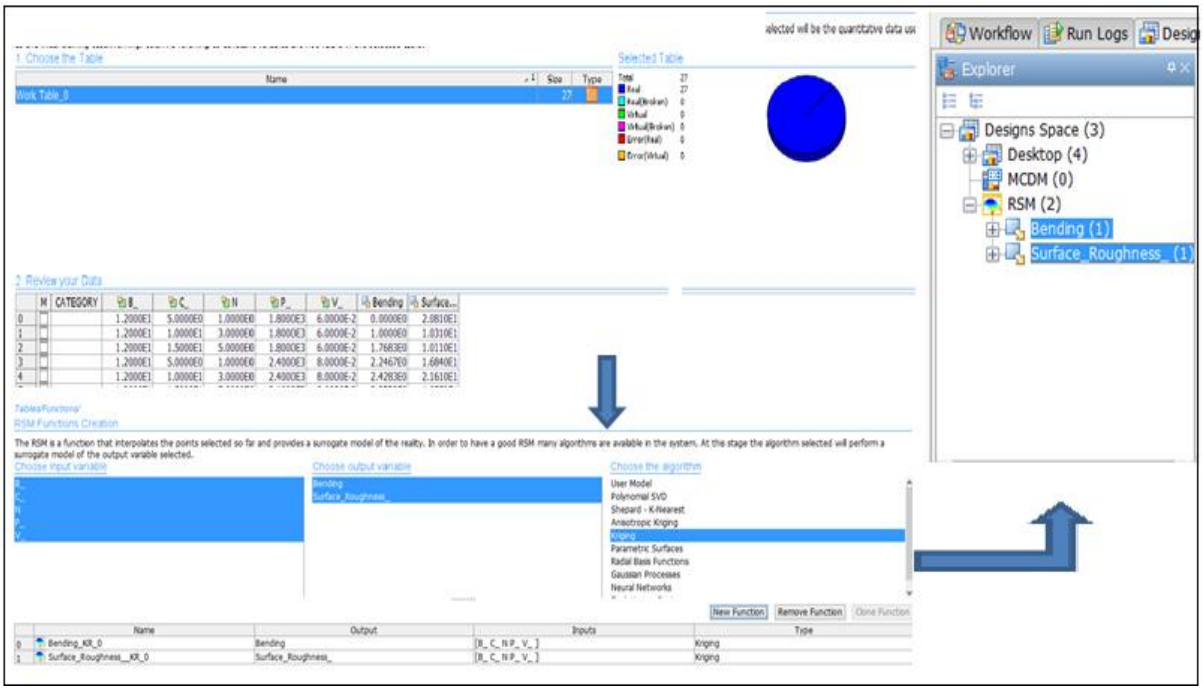

Figure 5.1-1 Screenshots to show the modeFRONTIER response surface creation tool; the definition of the inputs, outputs, algorithm and the response surface that is generated in the Design Space

After the response surface was generated, the **Workflow** tab was selected. The user had to create the flowchart to represent the relationship between the inputs, outputs, and response surface as in Figure 5.1-2.

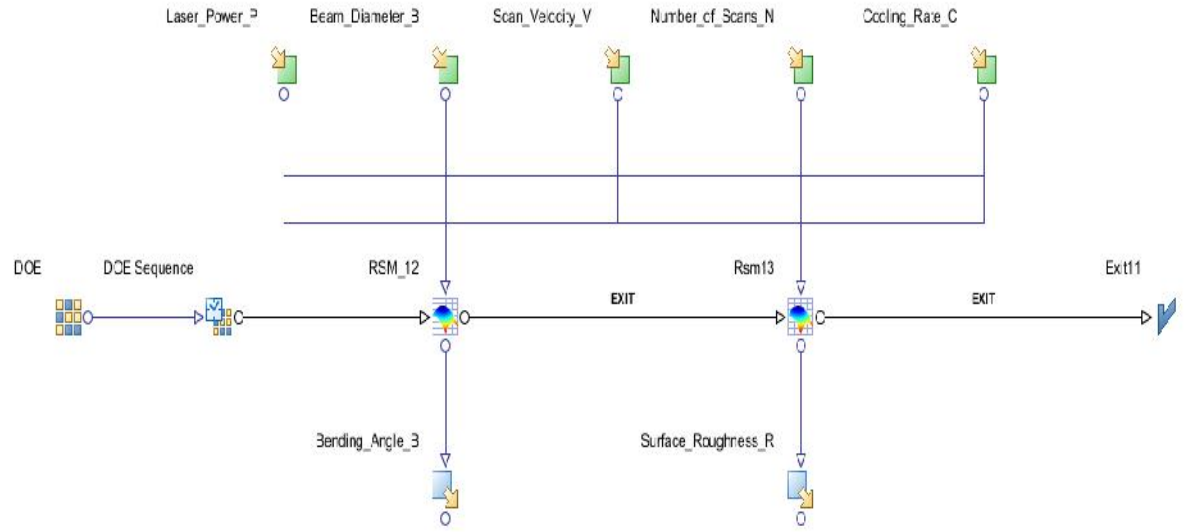

Figure 5.1-2 modeFRONTIER Workspace created flowchart used to generate the full-factorial 'virtual' RSM results

The explanations of each of the elements of the flowchart are explained in the proceeding steps.

1. The first step in initialising the flowchart is to set the upper and lower limits of each of the input parameters. This is done by double-clicking on each of the input icons and specifying the values. This step sets the upper and lower limits of the DoE.

2. After the limits are specified the DoE can be created by selecting the **DoE** icon. There are abundance of available DoE options. However, for this case, the full-factorial option is chosen. The user then has the option to choose any number of levels for each of the factors. In this case, 10 levels were chosen for each of the three machining parameters as shown in Table 5.1-1. This amounts to a total of 1000 solutions whose input values are distributed between the upper and lower limits that were specified in the previous step. This large sample set, of 1000 solutions, ensures that the requirements of the central limit theorem will be satisfied.

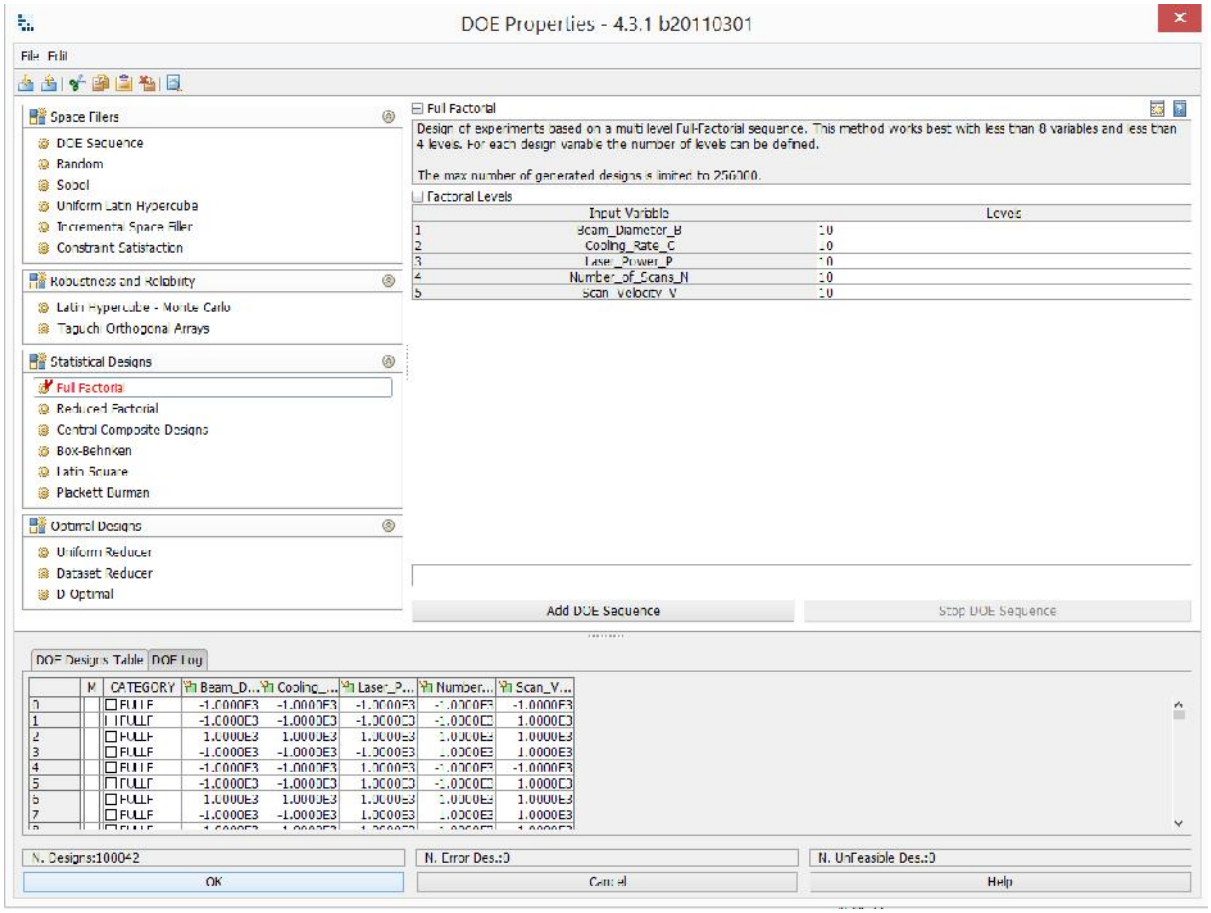

Figure 5.1-3 DOE options window from the modeFRONTIER Workflow

3. A solver is an option which is critical for a common optimisation routine. This is where the user specifies the optimisation algorithm that modeFRONTIER would use to find an optimised solution. For this case, however, the only values that need to be assessed are the values within the full-factorial DOE table. Therefore, the **scheduler** which is chosen, is the basic 'DOE Sequence'. This means that the only parametric design scenarios which modeFRONTIER will assess are the values in the DoE table and no optimisation algorithm is initialised.

4. The **RSM** icon is then selected as shown in Figure 5.1-1. The user has to specify the link between this node and the response surface which

was created within the 'Design Space'. The input and output parameters from the workflow also need to be related to the input and output parameters from the table which was imported to create the response surface. The reason for this is that often people will provide different labels in the input table and the flowchart. Therefore, the user needs to manually tell modeFRONTIER the connection between the various parameters.

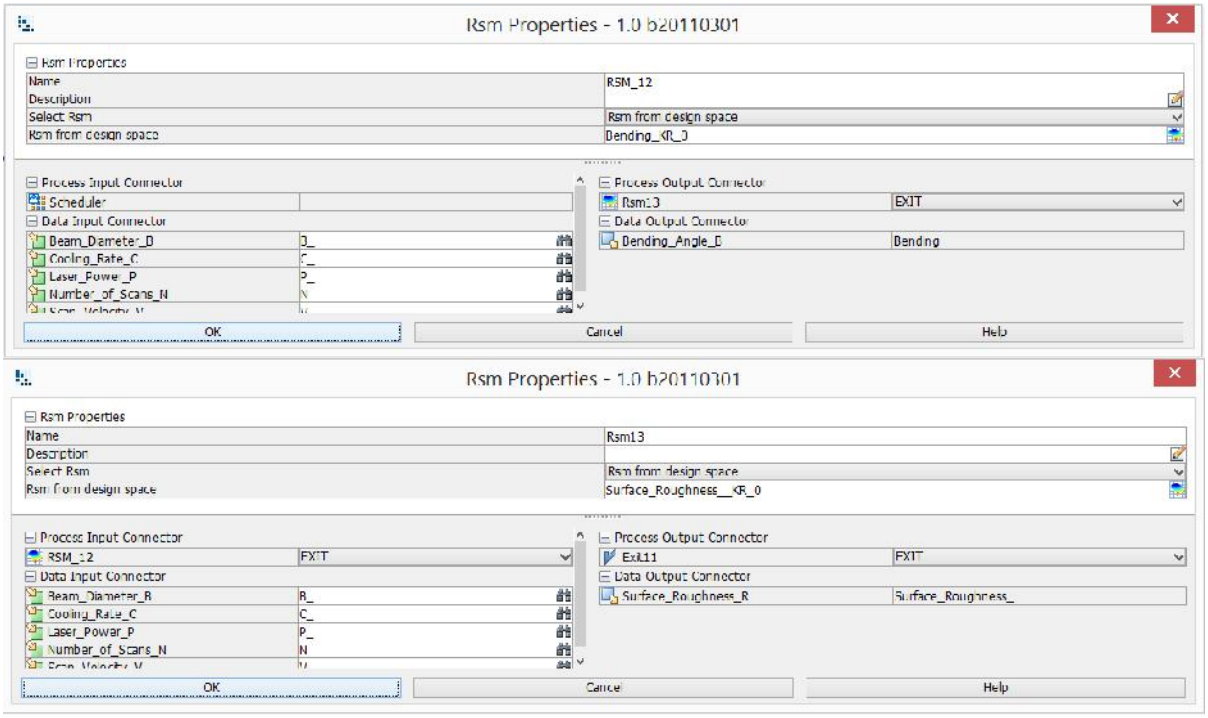

Figure 5.1-4 The RSM options window from the modeFRONTIER Workflow

5. The **Logic End** icon is specified to indicate that the results from the response surface don't need to be passed into any other software. For example, one could pass the solutions into another program such as Ansys, Excel or Matlab.

6. The **objective** icon is a requirement to allow modeFRONTIER to begin its processing. For this case, no objective is required since only the DOE table is being assessed. Therefore, once the icon is connected to the output the user can simply double-click on the icon to open the options window and un-check the ’enable’ button.

7. The final step is to choose the **Run/Stop** button to initialise the command for modeFRONTIER to begin assessing the response surface with the values from the DOE. The results are saved in the ’Design Space’ in the ’Design Table’.

5.2 Results and Discussions

The summary of the Bending Angle and the Surface Roughness Kriging response surface is shown in Figure 5.2-1 and 5.2-2. It indicates how the difference between the points of the fitted Kriging curve, and the experimental points, are always to at least 13 decimal places difference. This shows that the Kriging algorithm produces an excellent fit. Figure 5.2-3 and 5.2-4 indicates the Bending Angle and the Surface Roughness Kriging response surface drawn with a different combination of axes with parameters.

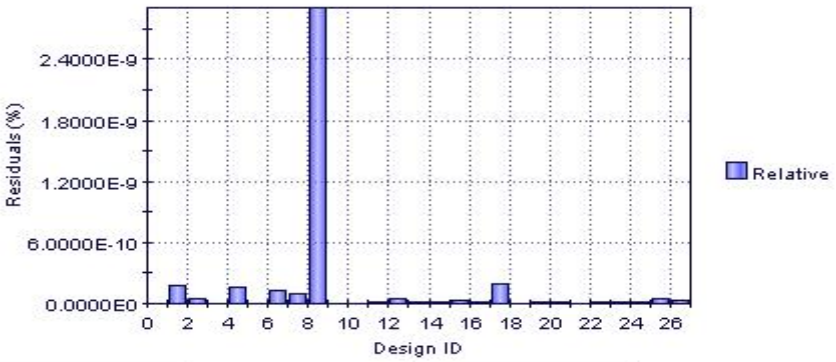

Max Abs. Error	4.3450E-12	Max Rel. Error	2.9062E-9
Mean Abs. Error	1.7231E-12	Mean Rel. Error	1.5056E-10
Regression	1.0000E0	Error Mean	1.1121E-12

Figure 5.2-1 Bending Angle Kriging RSM summary

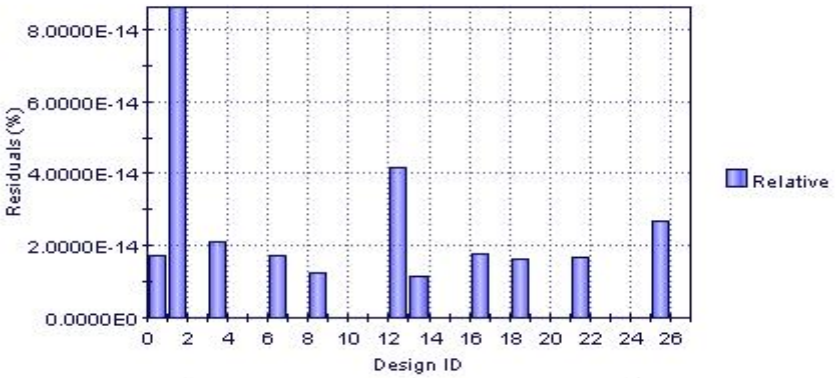

Max Abs. Error	1.4211E-14	Max Rel. Error	8.6147E-14
Mean Abs. Error	2.0066E-15	Mean Rel. Error	1.0539E-14
Regression	1.0000E0	Error Mean	-1.0198E-15

Figure 5.2-2 Surface Roughness Kriging RSM summary

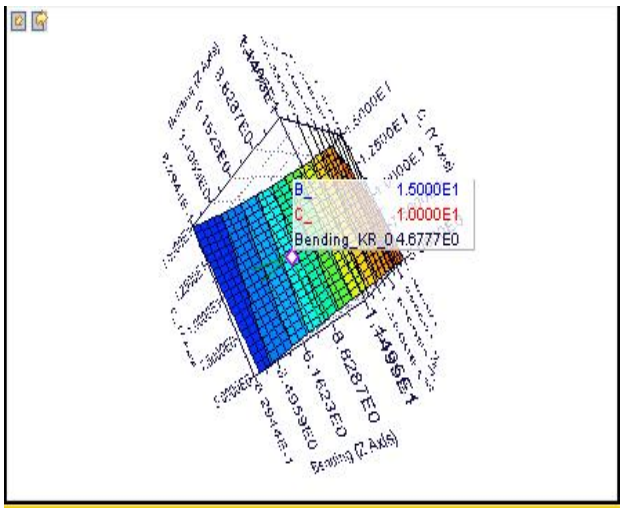

(a)

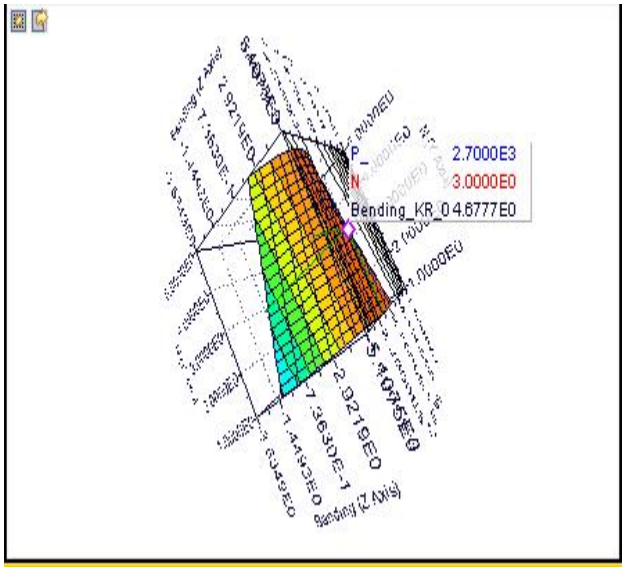

(b)

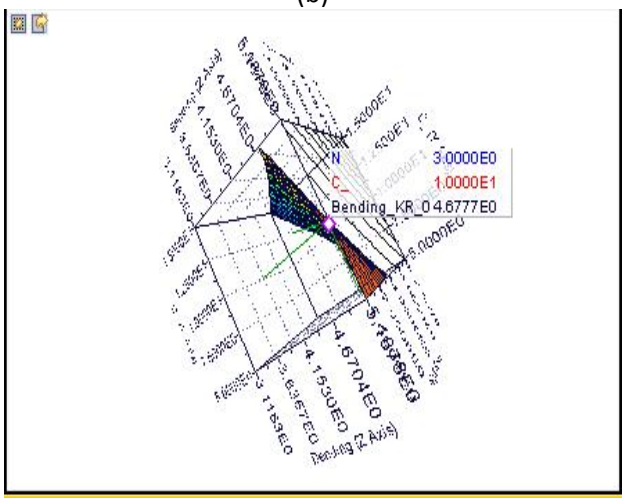

(c)

Figure 5.2-3 Contours indicating the Bending Angle Kriging response surface drawn with a different combination of axes

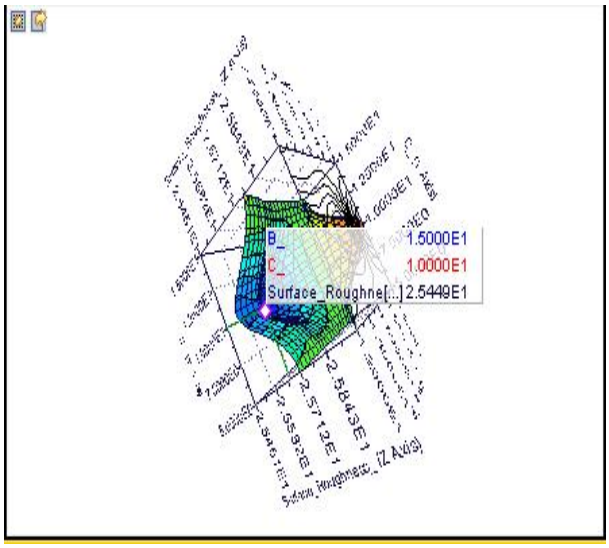

(a)

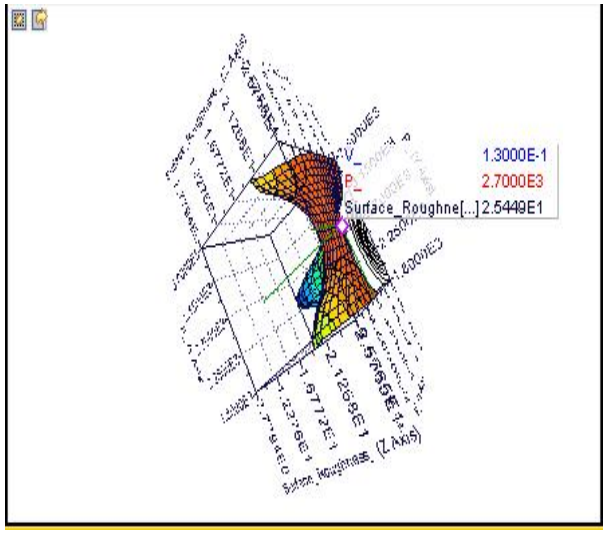

(b)

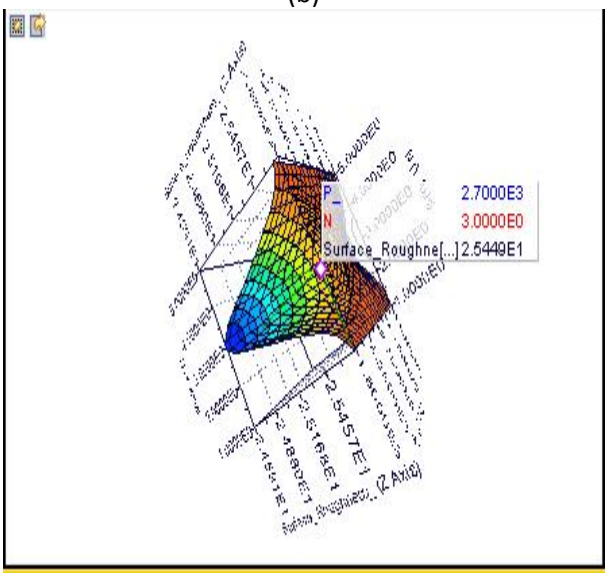

(C)

Figure 5.2-4 Contours indicating Surface Roughness Kriging response surface drawn with a different combination of axes

Figure 5.2-3 and 5.2-4 show the simulation combination for both the bending and surface roughness of the samples that are LBFormed using the level 1, level 2, and level 3 LBF process parameters, adapting the Kriging response surface from modeFRONTIER. Each figure in Figure 5.2-3 and 5.2-4 from top to bottom analysis are starting by displaying simulations derived from low, medium, and high laser forming parameters.

5.3 Conclusion

The summary of sample bending and the surface roughness Kriging response simulation, intensify that both the bending and surface roughness is low on samples machined using level 1 LBF parameters. While the bending and the surface roughness is high on samples machined using level 2 LBF parameters and higher on samples LBFormed using level 3 LBF parameters. The above conclusion is derived from the bending angle Kriging surface response analysis in Figure 5.2-3 and the surface roughness Kriging response analysis in Figure 5.2-4. Figure 5.2-3 and 5.2-4 are broken down in three analysis per figure, and with Figure 5.2-3 (a) and Figure 5.2-4 (a) analysing the results for samples machined using level 1 LBF parameters. While Figure 5.2-3 (b) and Figure 5.2-4 (b) is the results for level 2 LBFormed analyses. Figure 5.2-3 (c) and Figure 5.2-4 (c) is the results for level 3 LBFormed analyses. However, the combination of parameters that yield maximum bending and smooth surface roughness is not being determined.

Chapter 6

Concluding Remarks

This chapter provides a combined overview of the various results that have been derived from this research. It also lays the groundwork for future work with regard to laser beam forming optimisation on AISI 1008-mild steel.

6.1 Summary

Sample bending is the primary focus in this research report, because the surface roughness is what is compromised in the process of trying to achieve maximum sample bending. It is this poor surface roughness on LBFormed samples which makes LBF an unpopular forming process when it comes to mass production in industry. These concerns are currently restricting LBF from being employed in many industrial applications. This investigation is carried to optimise LBF processing parameters with the purpose of finding parameters that will yield the desired bending with smooth surface roughness.

Previously published work on LBF process has demonstrated that by only adjusting the laser beam diameter and the number of scans, does affect the bending angle and surface roughness without making any adjustments on other LBF process parameters. [1-5]. It is also known from literature that the scan speed have an influence in sample bending. Also the fact that different materials behave differently when LBFormed, even if LBF process parameters are kept constant [1-5]. Therefore, this brings into attention that material properties i.e. thermal conductivity, coefficient of thermal expansion, heat capacity, density of the material, elastic modulus and yield strength have influence on the behaviour of the material during LBF process [1-5].

The lack of knowledge on the influence which certain parameters have on LBF process is the most challenging aspect in getting the process right.

6.2 Conclusion and Recommendations

It is outlined in the literature that the laser power, scan speed, and the number of scans have a high impact on the material bending angle and surface roughness [21, 55]. The Taguchi DoE is one of the many problem-solving quality tools that was used for investigations, ranging from finding significant parameters (known as factors) with various possible settings (known as levels) [22, 57]. The purpose of the overall investigations carried out in this research is optimisation, which focused on investigating laser parameter interactions in terms of how they affect the desired outcome [8, 58]. The response surface was created using modeFRONTIER v4.3.1 multi-objective optimisation software. The Kriging algorithm is used in modeFRONTIER for this investigation.

It has been observed on this experiment that a small surface roughness is generated when the sample bending is negligible. It has also been observed that rough surface is on samples with the most bending or samples LBFormed using level 3 LBF parameters. These observations are seen to be in line with what is available in the literature, that maximum bending is achieved at the expense of surface roughness [3, 59]. The results showed that maximum sample bending is only attained when samples are machined using high/ level 3 LBF parameters. The following remarks are drawn from the data that is analysed from experiments carried throughout the research. The

aim of this research is to optimise LBF parameters which will yield maximum bending and smooth surface finishing of mild steel – AIS 1008 plates. However, currently the results achieved only satisfies maximum sample bending at the expense of rough surface finishing.

A material profile analysis on LBFormed samples was also done using a Confocal and Quanta microscopes. The microanalysis results were quantified to analyse the tested samples surface roughness. The results from the microanalysis illustrated that an unwanted relationship between high/level 3 LBF parameters and high surface roughness exists. Unfortunately a required solution to eliminate high surface roughness on LBFormed samples when the maximum bending angle is required could not be determined, except an understanding that samples machined using medium/level 2 and high/level 3 LBF parameters are prone to rough surfaces. This is because there seems to be linearity between the bending angle and material surface roughness [48]. This is observed from obtained results, where samples with small bending angle have small surface roughness and vice versa.

The influence of LBF parameters on experimental samples was further analysed using material hardness testing. The micro hardness results revealed that LBF has an effect on material hardness [52]. It has been determined that the material hardness on the immediate area next to the LBFormed scanned track also gets affected by the laser beam intensity, where a reduction on micro-hardness results is witnessed [52-53]. The conclusions that can be drawn from generated results are; when maximum material bending is the only requirement, then maximum/level 3 LBF parameters can be used. Otherwise low/level 1 to medium/level 2 LBF parameters should be used when

minimum material bending and moderate surface finish are required. The problem lies when both maximum bending and good surface finish are required, which this research was aimed to contribute and that objective was not achieved because the parameters that yield these results were could not be determined at the time of writing this report.

modeFRONTIER, which is the RSM discussed in Section 5.1 of Chapter 5 was used to perform further analysis on LBF parameters used to LBF experimental samples. LBF input parameters derived from the L_{27} orthogonal array were used to feed into modeFRONTIER to simulate and analyse best possible combinations for LBF parameters that have the ability to generate maximum bending and smooth surface roughness. Again, it was observed from both Bending and Surface Roughness Kriging response surface simulation, that bending and surface roughness are low on samples machined using low/level 1 LBF parameters and high on samples LBFormed using medium/level 2 to high/level 3 LBF parameters. Also, in the RSM analysis the optimum parameters required to produce maximum bending and low surface roughness were not achieved.

6.3 Future Work

Now that the influence and the effects of LBF parameters for mild steel AISI 1008 plate has been tested and understood. A research to develop ways to manage material property changes when samples are LBFormed using medium/level 2 and high/level 3 LBF parameters to achieve maximum bending with smooth surface finish is something to be considered. This is considered important to avoid unwanted surface

roughness on LBFormed samples. The research will have to look in a wide range of factors that influence LBF process, including material properties for particular samples that will be LBFormed, laser beam heat intensities produced by certain parameter combinations, etc. This should be considered in the DoE as part of the parameters selection.

References

1. E.T. Akinlabi, M Shukla, and S.A. Akinlabi. “Laser Forming of Titanium and Its Alloys– An Overview”. World Academy of Science, Engineering and Technology International Journal of Mechanical, Industrial Science and Engineering Vol:6 No:11, 2012, Pages 5-20
2. E.C Santos, M Shiomi, K. Osakada, T. Laoui. Rapid manufacturing of metal components by laser forming. Original Research Article: *International Journal of Machine Tools and Manufacture*, *Volume 46, Issues 12–13*, *October 2006*, *Pages 1459-1468.*
3. Optimization of Beam Mode for High Efficiency Laser Thermal Forming within Metallurgical Constraints. Original Research Article *Physics Procedia*, *Volume 56*, *2014*, *Pages 1392-1399.* Stuart P. Edwardson, J Griffiths, GSheikholeslami, G Dearden
4. S.P. Edwardson, J. Griffiths, G. Dearden and K.G.” Watkins. Towards Controlled Three Dimensional Laser Forming”. *Laser Group, School of Engineering, University of Liverpool, Liverpool, L69 3GH, UK. Lasers in Eng.*, Vol. 22, pp. 393–399, 2011.
5. S. P. Edwardson, J. Griffiths, G. Dearden, K. G. Watkins, “Temperature Gradient Mechanism: Overview of the Multiple Pass Controlling Factors”. *Laser Group, Department of Engineering, University of Liverpool, L69 3GQ, UK,* LANE 2010
6. M.S. Che Jamil1, M.A. Sheikh1 and L. Li. Laser Processing Research Centre (LPRC), School of Mechanical Aerospace and Civil Engineering, University of

Manchester, Manchester, M60 1QD, UK 2 School of Mechanical Engineering, University Saints Malaysia, Pulau Pinang 11800, Malaysia

7. J.D. Majumdara, A.K. Nath, I. Mannaa. Studies on laser bending of stainless steel. *Department of Metals & Materials Engineering, Indian Institute of Technology, Kharagpur* 25 May 2004
8. P.J. Cheng, S.C. Lin, J. Mater. Proc. Technol. 108 (2001) 314.
9. W. Shichun, Z. Jinsong. An experimental study of laser bending for sheet metals. Journal of Material Processing Technology 2001; 110:160–3.
10. P. Cheng, Y.L Yao, C. Liu, D. Pratt, Fan Y. Analysis and prediction of size effect on laser forming of sheet metal. Journal of Manufacturing Processes 2005. Page 28–41.
11. Shen H, Shi Y, Yao ZQ. Laser forming of plates using two sequent scans of different intervals. Proceedings of the Institution of Mechanical Engineers, Part C: Journal of Mechanical Engineering Science 2006.
12. H. Shen, Y. Shi, Z.Q. Yao. Study on overlapping of two sequential scans in laser forming. Proceedings of the Institution of Mechanical Engineers, Part C: Journal of Mechanical Engineering Science 2007.
13. J. Bao, Y.L. Yao. Analysis and prediction of edge effects in laser bending. Journal of Manufacturing Science and Engineering 2011; Page 53–62.
14. S.P. Edwardson, J. Griffiths, K.R. Edwards, G. Dearden, K.G. Watkins. Laser forming overview of the controlling factors in the temperature gradient mechanism. Proceedings of the Institution of Mechanical Engineers, Part C: Journal of Mechanical Engineering Science 2010; 224:1031–40.
15. J.H Shen, Z. Yao. Analysis and control of edge effects in laser bending. Journal of Optics and Lasers in Engineering 2010; 48:305–15.

16. Q. Cao, H. Shen. Experimental study on edge effects in laser bending. Journal of Laser Applications 2010; 22:144–50.
17. H. M. Gollo, S.M. Mahdavian, N.H. Moslemi. Statistical analysis of parameter effects on bending angle in laser forming process by pulsed Nd: YAG laser. Journal of Optics and Laser Technology 2011; 43:475–82.
18. X.B. Zhang, Y.J. Liu. Design of convex hull plate forming by pure line heating. Journal of Marine Science and Application 2004; 3:17–23.
19. Y.G. Modelling of shell forming by line heating. PhD thesis. USA: Mussu-chusetts Institute of Technology; 2000.
20. W. Li, Y.L. Yao. Laser forming with constant line energy. International Journal of Advanced Manufacturing Technology 2001; 17:196–203.
21. G.C. Jha, A.K. Nath, S.K. Roy. Study of edge effect and multi-curvature in laser bending of AISI 304 stainless steel. Journal of Material Processing Technology 2008; 197:434–8. [17]
22. S. Yongjun, S. Hong, Y. Zhenqiang, H. Jun. Temperature gradient mechanism in laser forming of thin plates. School of Mechanical and Power Engineering, Shanghai Jiao Tong University, Shanghai 200030, China. March 2006
23. J. Jeswiet, F. Micari, G. Hirt, A. Bramley, J. Duflou, J. Allwood. Asymmetric single point incremental forming of sheet metal, CIRP Annals—Manufacturing Technology 54, 2005. Page 623–649.
24. J. Cao, Y. Huang, N.V. Reddy, R. Malhotra, Y. Wang, Incremental sheet metal forming: advances and challenges, in :Proceedings of the International Conference on Technology of Plasticity, ICTP 2008, pp.1967–1982.

25. W.C. Emmens, G. Sebastiani, A.H. vanden Boogaard. The technology of incremental sheet forming—a brief review of the history, Journal of Materials Processing Technology 210(2010)981–997.
26. R. Malhotra, L. Xue, T. Belytschko, J. Cao, Mechanics of fracture in single point incremental forming, Journal of Materials Processing Technology 212(2012) 1573–1590.
27. M. Dittrich, T. Gutowski, J. Cao, J. Roth, Z. Xia, V. Kiridena, F. Ren, H. Henning. Energy analysis of incremental sheet forming. Production Engineering 6(2012) 169–177.
28. G. Ingarao, G. Ambrogio, F. Gagliardi, and R. DiLorenzo. A sustainability point of view on sheet metal forming operations: Material wasting and energy consumption in incremental forming and stamping processes, Journal of Cleaner Production (29–30) (2012)255–268.
29. A. Governale, A. Lo Franco, A. Panzeca, L. Fratini, F. Micari, Incremental forming process for the accomplishment of automotive details. Key Engineering Materials 344(2007) 559–566.
30. G. Ambrogio, L. DeNapoli, L. Filice, E. Gagliardi, M. Muzzupappa. Application of incremental forming process for high customised medical product manufacturing, Journal of Materials Processing Technology 162 (2005)156–162.
31. G. Hussain, L. Gao. A novel method to test the thinning limits of sheet metals in negative incremental forming, International Journal of Machine Tools & Manufacture 47 (2007)419–435.

32. E.L. Odenberger, R. Pederson, M. Oldenburg. Thermomechanical material response and hot sheet metal forming of Ti-6242, Materials Science and Engineering A489 (2008) 158–168.
33. E.L. Odenberger, R. Pederson, M. Oldenburg. Thermomechanical material response and hot sheet metal forming of Ti-6242. Materials Science and Engineering A489 (2008)158–168.
34. K.F. Zhang, D.L. Yin, D.Z. Wu. Formability of AZ31 magnesium alloy sheets at warm working conditions, International Journal of Machine Tools & Manufacture 46 (2006) 1276–1280.
35. K. Iwanaga, H. Tashiro, H. Okamoto, K. Shimizu. Improvement of formability from room temperature to warm temperature in AZ-31 magnesium alloy, Journal of Materials Processing Technology 155 (2004) 1313–1316.
36. M. Skjoedt, N. Bay, B. Endelt, G. Ingarao, Multistage strategies for single point incremental forming of a cup, International Journal of Material Forming 1 (2008)1199–1202.
37. J.R. Duflou, J. Verbert, B. Belkassem, J. Gu, H. Sol, C. Henrard, A.M. Habraken, Process window enhancement for single point incremental forming through multi-step tool paths, CIRP Annals—Manufacturing Technology 57 (2008) 253–256.
38. R. Malhotra, A. Bhattacharya, A. Kumar, N.V. Reddy, J. Cao, A new methodology for multi-pass single point incremental forming with mixed tool paths ,CIRP Annals—Manufacturing Technology60 (2011)323–326.
39. D. Xu, R. Malhotra, N.V. Reddy, J. Chen, J. Cao. Analytical prediction of stepped feature generation in multi-pass single point incremental forming, Journal of Manufacturing Processes 14 (2012)487–494.

40. M. Otsu, H. Matsuo, M. Matsuda, K. Takashima, Friction stir incremental forming of aluminium alloy sheets, Steel Research International 81(2010) 942–945.
41. M. Otsu, T. Ichikawa, M. Matsuda, K. Takashima, Improvement of formability of magnesium alloy sheets by friction stir incremental forming, steel research international, special edition, in: Proceedings of 10th International Conference on Technology of Plasticity, ICTP 2011, 2011, pp.537–541.
42. G. Buffa, D. Campanella, L. Fratini, On the improvement of material formability in SPIF operation through tool stirring action, International Journal of Advanced Manufacturing Technology 66 (2012)1–9.
43. M. Durante, A. Formisano, A. Langella, F.M.C. Minutolo, The influence of tool rotation on an incremental forming process, Journal of Materials Processing Technology 209 (2009) 4621–4626.
44. K. Hamilton, J. Jeswiet, Single point incremental forming at high feed rates and rotational speeds: Surface and structural consequences, CIRP Annals—Manufacturing Technology 59(2010)311–314.
45. J. Jeswiet, J.R. Duflou, A. Szekeres, Forces in single point and two point incremental forming, Advanced Materials Research (6–8) (2005) 449–456.
46. L. Filice, G. Ambrogio, F. Micari, On-line control of single point incremental forming operations through punch force monitoring, CIRP Annals—Manufacturing Technology 55 (2006) 245–248.
47. G. Ambrogio, L. Filice, F. Micari, A force measuring based strategy for failure prevention in incremental forming, Journal of Materials Processing Technology 177 (2006) 413–416.

48. J. Duflou, Y. Tunckol, A. Szekeres, P. Vanherck, Experimental study on force measurements for single point incremental forming, Journal of Materials Processing Technology 189 (2007) 65–72.
49. D Xu, W. Wu, R. Malhotra, J. Chen. Mechanism investigation for the influence of tool rotation and laser surface texturing (LST) on formability in single point incremental forming. Department of Plasticity Technology, Shanghai Jiao Tong University, Shanghai 2003.
50. J. Magee, K.G. Watkins, W.M. Steen. Advances in laser forming. Journal of laser applications 10(6) (1998), 235-246.
51. S. Dejardin, S. Thibaud, J.C. Gelin. Finite element analysis and experimental investigations for improving precision in single point incremental sheet forming process. Springer/ESAFORM 2008 1:121 –124,
52. M. Kutz. Handbook of material Selection. New York: John Wiley & Sons; 2002
53. M.S. Che Jamil, M.A. Sheikh, and L. Li. Laser Processing Research Centre (LPRC), School of Mechanical Aerospace and Civil Engineering, University of Manchester, Manchester, M60 1QD, UK 2 School of Mechanical Engineering, University Saints Malaysia, Pulau Pinang 11800, Malaysia
54. K. P Shah. Iron-carbon equilibrium diagram. Cited 2015 June 21. Available from: http://practicalmaintenance.net/?p=1315
55. E.T. Akinlabi, S. A. Akinlabi, F. Pietra. Experimental Data Analysis of LBF Steel Samples. Transformation of L-27 Taguchi to Full Factional. International Journal of Management & Computing Sciences Vol -3 No. 3(2013) PP 34-47

56. S. Fraley, M. Oom, B. Terrien, J. Zalewski http://www.freequality.org/documents/tools/Tagarray_files/ tamatrix.htm - Last accessed on the 20 May 2015.

57. J. Magee, K.G. Watkins, W.M. Steen, N.J. Calder, J. Sidhu, J. Kirby, J. Laser App. 10 (1998) 149.

58. N.S. Bailey, W. Tan, Y.C. Shin. Predictive modelling and experimental results for residual stresses in laser hardening of AISI 4140 steel by a high power diode laser. Original Research Article. *Surface and Coatings Technology*, *Volume 203, Issue 14*, *15 April 2009*, *Pages 2003-2012.*

59. D.A. Lesyka, S. Martinezb, V.V. Dzhemelinskyya, A. Lamikizb, B.N. Mordyukc, G.I. Prokopenkoc .Surface micro relief and hardness of laser hardened and ultrasonically peened AISI D2 tool steel. Original Research Article: *Surface and Coatings, Ukraine 2015*

60. E.T. Akinlabi, S.A. Akinlabi. Experimental Investigation of Laser beam forming of Titanium and Statistical Analysis of the Effects of Parameters on Curvature. Proceedings of the International Multi Conference of Engineers and Computer Scientists 2013 Vol II, IMECS 2013, March 13 - 15, 2013, Hong Kong

61. Esther T. Akinlabi, Stephen A. Akinlabi, Francesco Pietra. Experimental Data Analysis of LBF Steel Samples. Transformation of L-27 Taguchi to Full Factional. International Journal of Management & Computing Sciences Vol -3 No. 3(2013) PP 34-47

62. W. Li, Y. L. Yao. Numerical and Experimental Investigation of Convex Laser Forming Process. Dept. of Mechanical Engineering, Columbia University, New York, New York, USA. E-mail: yly1@columbia.edu

63. M.H. Gollo , S.M. Mahdavian, H.M. Naeini Statistical analysis of parameter effects on bending angle in laser forming process by pulsed Nd: YAG laser. Optics & Laser Technology Volume 43, Issue 3, April 2011, Pages 475–482. http://www.wits.ac.za/research/mmu/microscopy%20and%20microanalysis%20unit/techniques/22234/light_optical_and_flourescence_microscope.html#CM – Last assessed 8th September 2015.
64. J. Lawrence, M.J.J. Schmidt, L. Li. The forming of mild steel plates with a 2.5 kW high power diode laser. Volume 41, Issue 7, May 2001, Pages 967–977.
65. J. Go¨ttmann, J. Diettrich, G. Bergweiler, M. Bambach, G. Hirt, P. Loosen, R. Poprawe. Laser-assisted asymmetric incremental sheet forming of titanium sheet metal parts. Received: 25 July 2010 / Accepted: 2 February 2011 / Published online: 18 February 2011. German Academic Society for Production Engineering (WGP) 2011
66. W. Li, Y. L. Yao. Laser bending of tubes: Mechanisms, Analysis and Prediction. Transaction of the ASME, Vol 123, November 2001.
67. D. J. Chen, S. C. Wu. Studies on laser forming of Ti -6Al-4V alloy sheet. Journal of Materials Processing Technology, Vol. 152, 2004.
68. S. Poles. Bench-marking MOGA-II. Technical report 2004-001, ESTECO, Trieste, 2003, http://www.esteco.com. Last accessed 15 November 2014
69. L. Sullivan. http://www.isixsigma.com/tools-templates/analysis-of-variance-anova/using-anova-find-differences-population-means/ -Last accessed 31 February 2015
70. D.C. Montgomery. Design, analyses of experiments. Third ed., John Wiley & Sons, 1997.

71. P. Ross. Taguchi techniques for quality engineering. New York: McGraw-Hill, 1996

72. R. Roy. *A Primer on the Taguchi Method*. Society of Manufacturing Engineers, http://www.freequality.org/documents/tools/Tagarray_files/tamatrix.htm -Last accessed on the 13th May 2015.

73. S.P. Edwardson, J. Griffiths, G. Sheikholeslami, G. Dearden. Optimization of Beam Mode for High Efficiency Laser Thermal Forming within Metallurgical Constraints. Original Research Article, *Physics Procedia*, *Volume 56*, *2014*, *Pages 1392-1399.*

74. B.S. Yilbas, A.F.M. Arif, B.J. Abdul Aleem. Laser bending of AISI 304 steel sheets: Thermal stress analysis. Optics & Laser Technology Volume 44, Issue 2, March 2012, Pages 303–309.

75. R. Kant, S.N. Joshi, U.S. Dixit. *Materials Forming and Machining*, *2016*, *Pages 73-97.*

76. S.S. Akhtar, B.S. Yilbas. *Reference Module in Materials Science and Materials Engineering, from Comprehensive Materials Processing*, *Volume 9*, *2014*, *Pages 25-46*, Current as of 28 October 2015.

77. A. Alaswad, K.Y. Benyounis, A.G. Olabi. Optimization Techniques in Material Processing. *Reference Module in Materials Science and Materials Engineering*, *2016*, Current as of 28 October 2015.

78. A.K. Dubey, V. Yadava. Experimental study of Nd: YAG laser beam machining - An overview. Review Article. *Journal of Materials Processing Technology*, *Volume 195, Issues 1–3*, *1 January 2008*, *Pages 15-26*.

79. M. Kang, Y. Kim, C. Kim. Effect of heating parameters on laser welded tailored blanks of hot press forming steel. Original Research Article. *Journal of Materials Processing Technology*, *Volume 228*, *February 2016*, *Pages 137-144*.

80. M. Launhardt, A. Wörz, A. Loderer, T. Laumer, D. Drummer, T. Hausotte, M. Schmidt. Detecting surface roughness on SLS parts with various measuring techniques. Original Research Article: *Polymer Testing*, *Volume 53*, *August 2016*, *Pages 217-226.*

81. Z. Zhang, L. Ren, T. Zhou, Z. Han, H. Zhou, L. Chen, Y. Zhao. Optimization of Laser Processing Parameters and Their Effect on Penetration Depth and Surface Roughness of Biomimetic Units on the Surface of 3Cr2W8V Steel. Original Research Article: *Journal of Bionic Engineering*, *Volume 7, Supplement*, *September 2010*, *Pages 67-76.*

82. F. Cordovilla, Á. García-Beltrán, P. Sancho, J. Domínguez, L. Ruiz-de-Lara, J. L. Ocaña. Numerical/experimental analysis of the laser surface hardening with overlapped tracks to design the configuration of the process for Cr-Mo steels. Original Research Article: *Materials & Design*, *Volume 102*, *15 July 2016*, *Pages 225-237.*

Appendix A

A.1 Equipment and Sample Data

Table A.1 Experimental Equipment Data

Laser	
Maximum Power	3600 W
Maximum Beam Diameter	18 mm
Maximum Scan Velocity	0.2 m/s
Maximum Number of Scans Tracks	5
Maximum Cooling Flow	15l/min
Original Sample Size	
Length	200 mm
Width	50 mm
Thickness	3 mm
Smaller Sample Size for Microscopic Analysis	
Length	75 mm
Width	20 mm
Thickness	3 mm
Dial Indicator	
Range	10 mm
Scale	0.01mm
Steel Ruler	
Range	300 mm
Scale	1 mm

Appendix B

B.1 Experimental Procedure Data

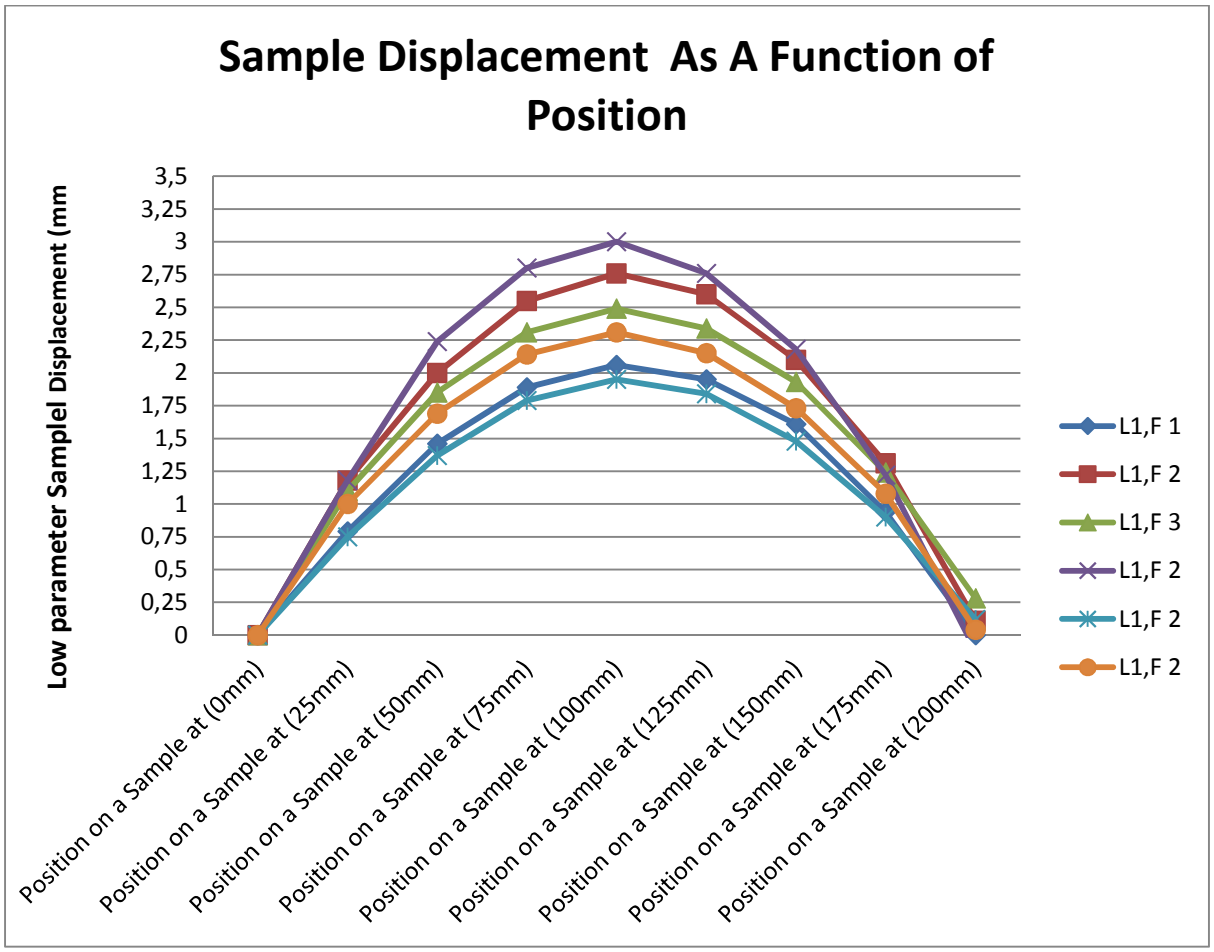

Figure B.1 Line Chart of Sample Displacement as a Function of Position, on Low/Level 1 LBF Parameters

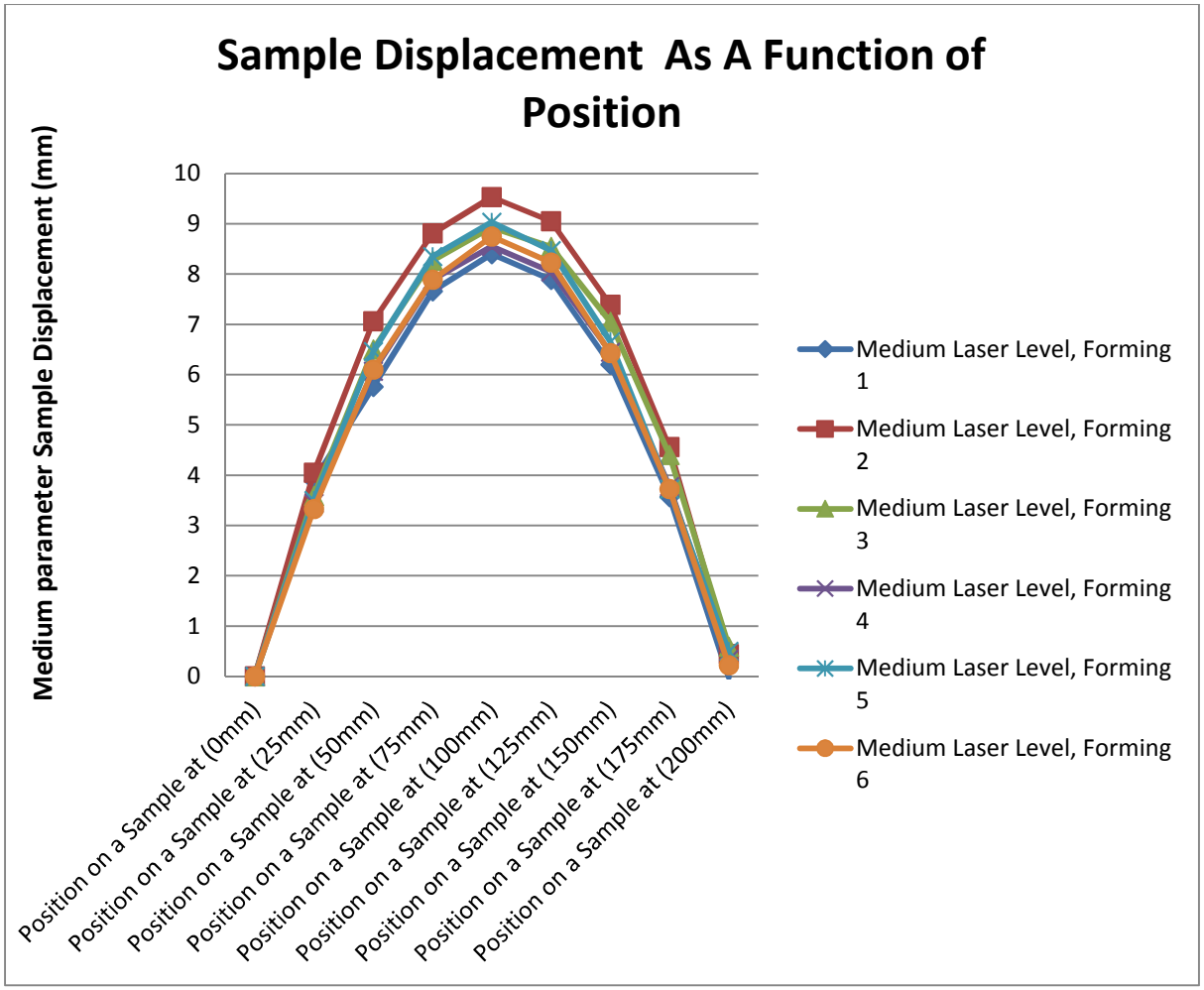

Figure B.2 Line Chart of Sample Displacement as a Function of Position, on Medium/Level 2 LBF Parameters

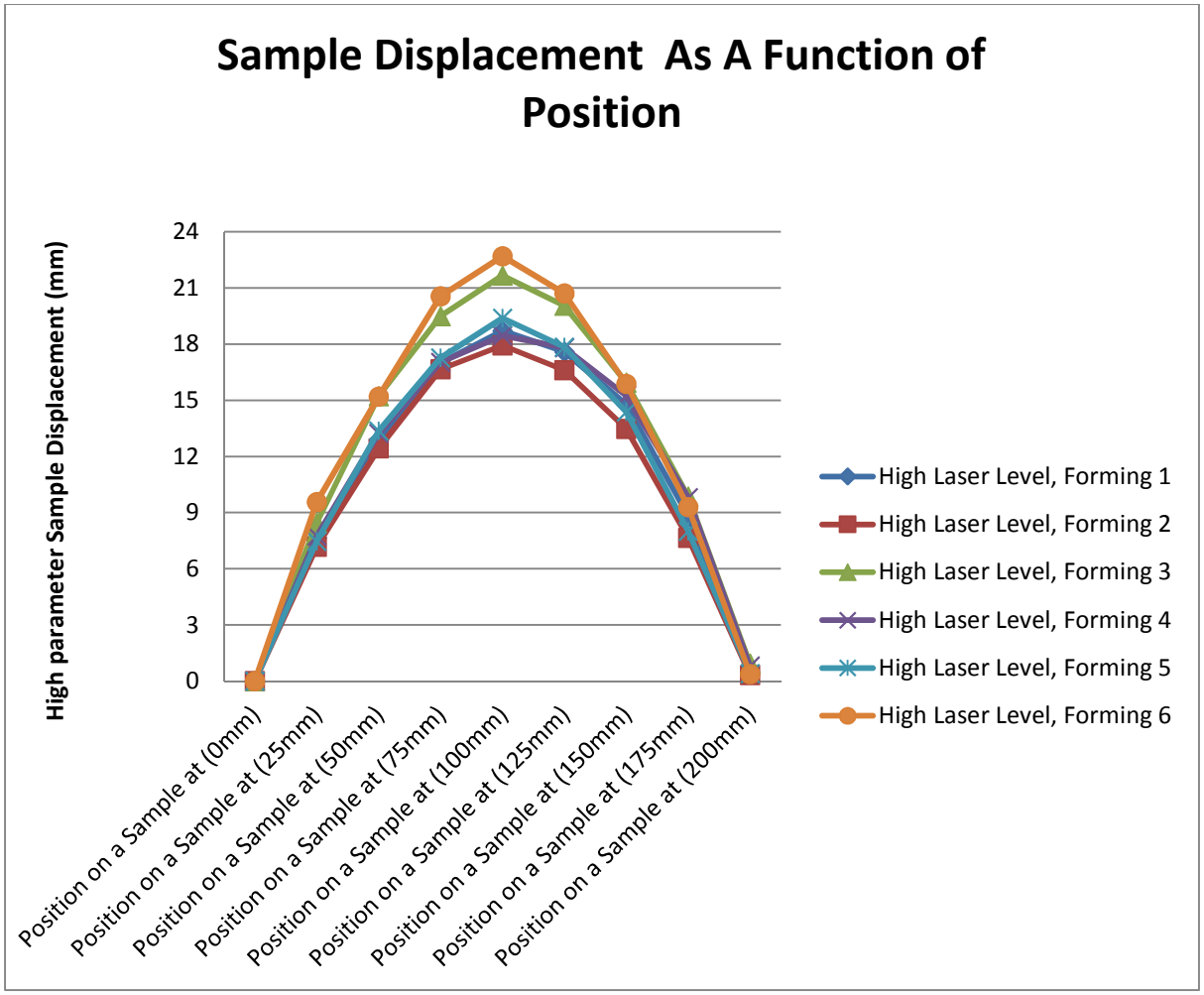

Figure B.3 Line Chart of Sample Displacement as a Function of Position, on High/Level 3 Parameters

Appendix C

C.1 Micro Hardness Test Data

Table C.1 Results for Vickers Hardness Test Values for Samples 1, 2, & 3 (HLFP, MLFP, & LLFP)

Load applied = 0.5kg											
dwell time = 15s											
Sample 1				**Sample 2**				**Sample 3**			
Initial Width from the Edge of the Sample (µm)	**Width (µm)**	**Hardness (HV)**	**Batch Average for Column ©**	**Initial Width from the Edge of the Sample (µm)**	**Width (µm)**	**Hardness (HV)**	**Batch Average for Column (G)**	**Initial Width from the Edge of the Sample (µm)**	**Width (µm)**	**Hardness (HV)**	**Batch Average for Column (K)**
Depth 84,38	84,38	142,8		**124.88**	124,88	181,1		**Depth 102,97**	102,97	180,20	
	182,14	139,4			272,08	181			203,78	168,50	
	283,65	139,4			350,96	167,1			328,04	177,80	
	410,62	145,5			431,62	171,6			443,22	176,50	
Non-Laser Formed Region	532,15	140,9	**140,6818**		611,92	174,6		**Laser Formed Region**	571,62	173,00	**165,57**
	652,92	143		**Non-Laser Formed Region**	737,72	178,3	**179,9091**		678,69	171,10	
	769,55	135,7			899,52	180,9			789,88	162,30	
	902,32	142,2			1023,22	184,3			901,42	163,50	
	1041,62	144,1			1238,44	178,7			1011,95	154,40	
	1167,96	141,5			1363,04	192,3			1141,78	128,40	
	1292,39	133			1482,59	189,1		**1st Jump to the new region on the material**	2341,78	177,40	
1st Jump to the new region on the material	2692,39	128,1		**1st Jump to the new region on the material**	2182,59	186,8			2464,01	169,90	
	2820,22	127			2312,94	184,8			2583,9	175,30	
	2941,73	135,7			2480,09	185,3			2709,81	182,00	
	3072,51	134,8			2596,18	181		**Laser Formed Region**	2834,4	140,10	**161,76**
Non-Laser Formed Region	3200,6	141,7	**133,93**	**Non-Laser Formed Region**	2725,07	176,8	**181,48**		2963,21	158,40	
	3326,53	132			2822,25	180,2			3077	156,70	
	3455,37	132,5			2962,11	169,3			3189,93	145,80	
	3560,64	135,4			3123,77	180,7			3302,53	136,40	
	3715,93	130			3283,5	179,9			3421,39	175,60	
	3858,11	142,1			3453,78	190		**2nd Jump to the new region on the material**	4521,39	180,40	
2nd Jump to the new region on the material	4958,11	140,9		**2nd Jump to the new region on the material**	4703,78	184			4633,96	177,60	
	5096,19	139,2			4852,06	178,4		**Laser Formed Region**	4760,61	154,00	**167,88**
	5223,35	139,4			4989,82	172,8			4873,17	169,20	
	5346,04	138,7			5138,45	172,6			5000,88	158,20	
Non-Laser Formed Region	5454,04	139	**136,34**	**Non-Laser Formed Region**	5278,95	185,7	**180,7875**	**3rd Jump to the new region on the material**	5700,88	183,70	
	5581,17	141,7			5431,45	185,2			5807,69	186,50	
	5707,16	136,6			5588,34	184,9		**Non-Laser Formed Region**	5896,56	192,90	**187,52**
	5817,05	141,1			5740,62	182,7			5992,6	187,20	
	5944,37	136,6		**3rd Jump to the new region on the material**	7940,62	171,9			6092,15	187,30	
	6070,44	110,2			8082,73	161,5		**4th Jump to the new region on the material**	6592,15	174,30	

3rd Jump to the new region on the material	7570,44	108,6			8235,64	162,2			669,3	183,50	
	7703,7	113,5			8406,52	159,3		Non-Laser Formed Region	6785,09	183,90	**180,64**
	7815,06	107,6			8553,5	152,8			6893,12	185,70	
	7940,83	108,3		Laser Formed Region	8708,94	149,7	**159,7364**		6992,54	175,80	
	8061,7	112,2			8877,74	156,6		5th Jump to the new region on the material	7392,54	182,70	
	8170,75	112,3			9036,33	156,4			7512,57	181,60	
Laser Formed Region	8293,77	107,7	**109,5154**		9180,18	164,8		Non-Laser Formed Region	7615,79	181,70	**181,43**
	8416,01	104,9			9337,72	159,9			7735,31	179,70	
	8536,59	109,6			9478,85	162		6th Jump to the new region on the material	8185,31	176,60	
	8650,44	109,9		4th Jump to the new region on the material	10378,85	167,9			8298,31	174,00	
	8762,56	109,8			10552,35	161,7		Non-Laser Formed Region	8424,84	178,70	**178,44**
	8880,7	109,7		Laser Formed Region	10719,93	157,4	**162,18**		8542,93	175,60	
	9003,61	109,6			10874,71	157			8657,63	187,30	
4th Jump to the new region on the material	9703,61	107,7			11036,09	166,9		7th Jump to the new region on the material	9077,63	175,60	
	9860,06	109,5		6th Jump to the new region on the material	11736,09	166,6			9185,38	184,70	
	9995,15	103,2			11882,12	166,9			9309,48	185,80	
Laser Formed Region	10125,36	104,7	**105,8667**	Laser Formed Region	12036,35	158,9	**164,06**	Non-Laser Formed Region	9426,45	186,90	**187,52**
	10250,15	105,2			12194,38	166,3			9552,11	196,30	
	10383,38	104,9			12346,76	161,6			9674,91	195,80	
Total HV Average		**126,182**		Total HV Average		**172,568**		Total HV Average		**173,93**	

Appendix D

D.1 Response Surface Data

This appendix contains information relating to the Kriging response surface which was used to determine the full factorial ANOVA results based on the original Taguchi L_{27} orthogonal array.

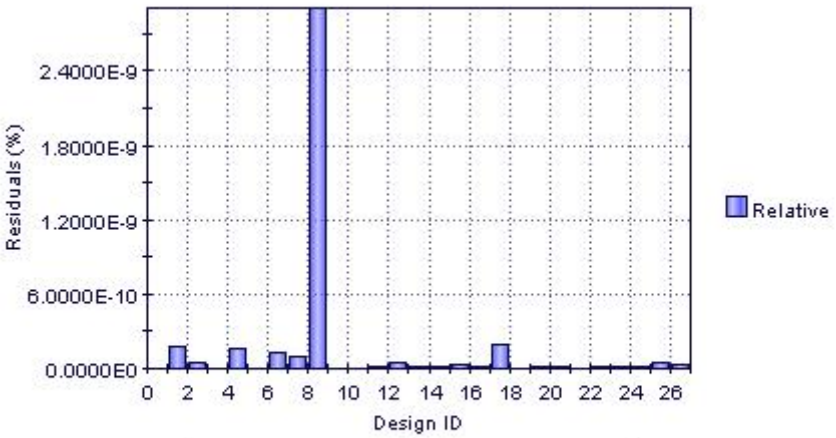

Max Abs. Error	4.3450E-12	Max Rel. Error	2.9062E-9
Mean Abs. Error	1.7231E-12	Mean Rel. Error	1.5056E-10
Regression	1.0000E0	Error Mean	1.1121E-12

Figure D.1 Bending residual Kriging RSM summary

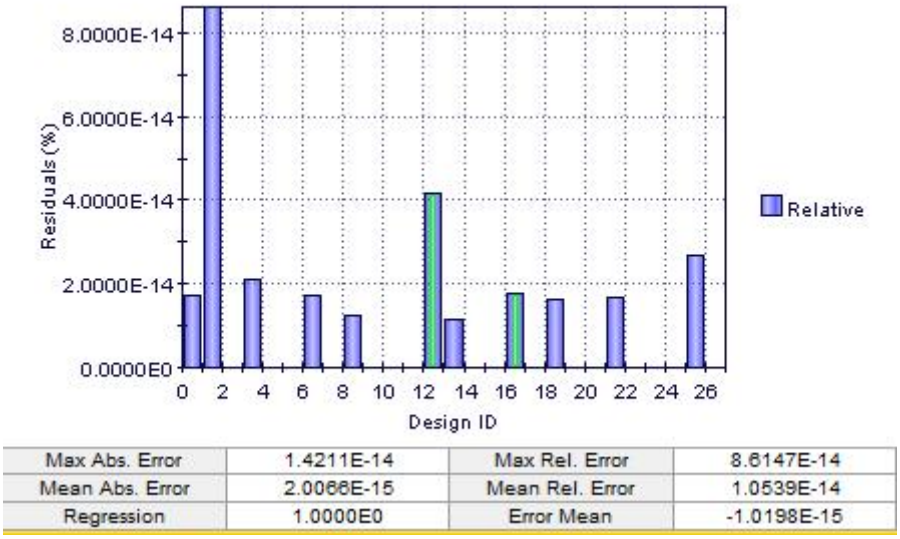

Max Abs. Error	1.4211E-14	Max Rel. Error	8.6147E-14
Mean Abs. Error	2.0066E-15	Mean Rel. Error	1.0539E-14
Regression	1.0000E0	Error Mean	-1.0198E-15

Figure D.1 Surface Roughness Residual Kriging RSM summary

The distance plot below illustrates the points where the real, and virtual values in the plot, which the desired bending can be obtained. The same is for the surface roughness distance plot which illustrates the area in the plot where the desired surface roughness can be obtained.

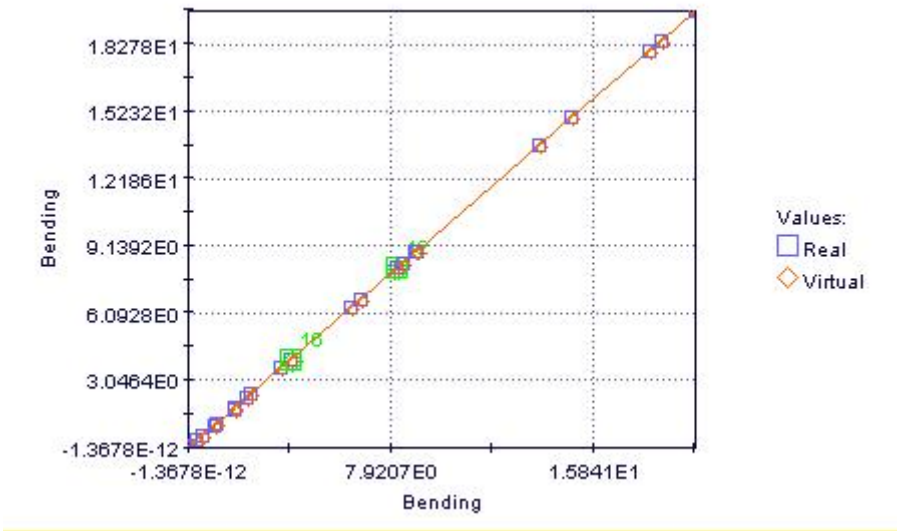

Figure D.2 Bending/Displacement Plot

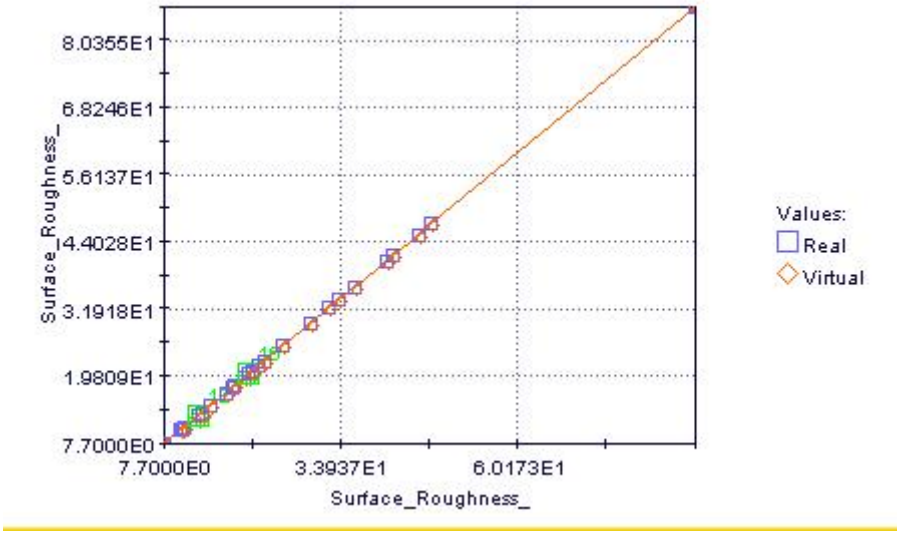

Figure D.3 Surface Roughness as a Function of Displacement Plot

The 3D functions charts which are representing bending and surface roughness are below.

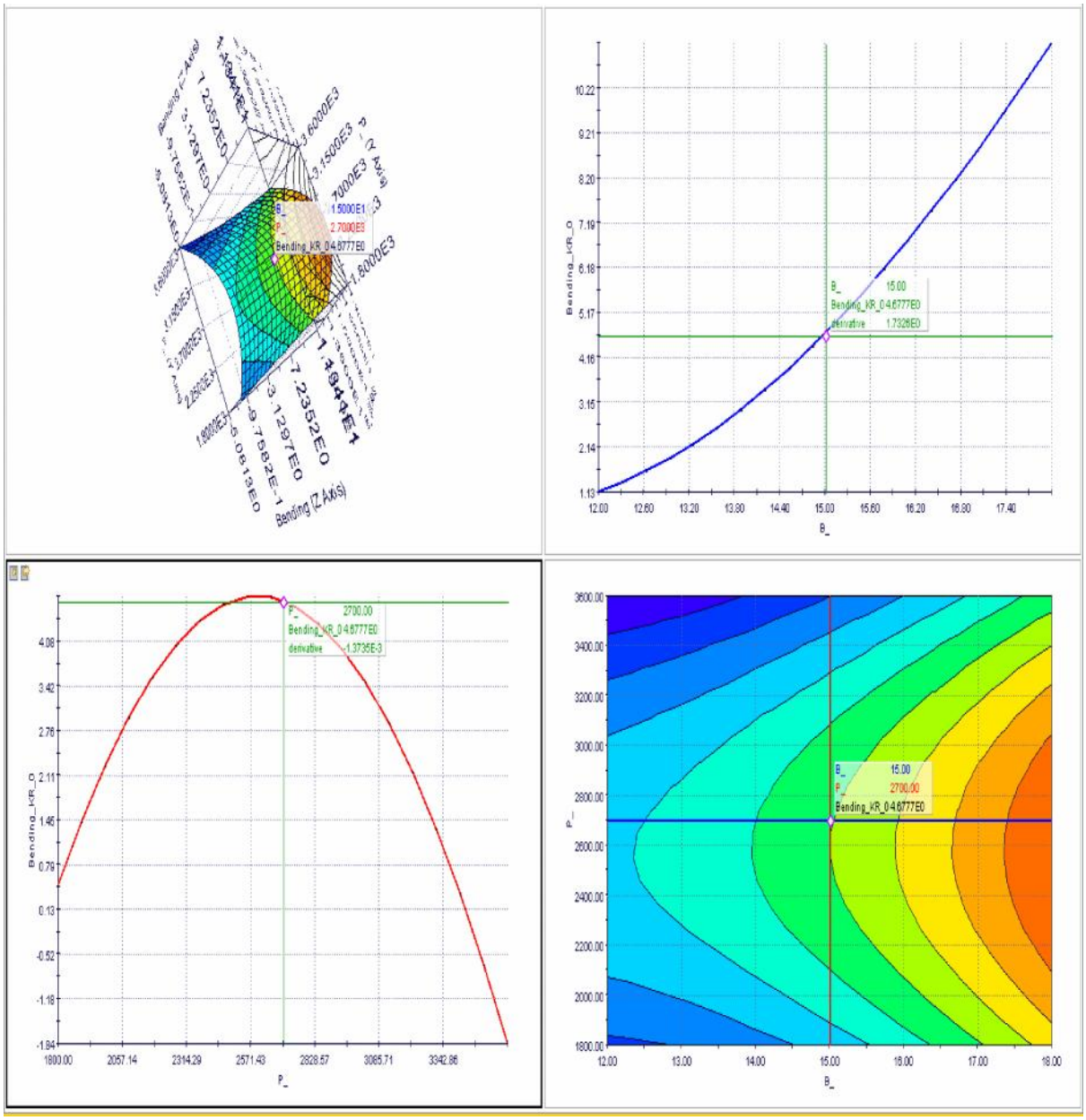

Figure D.4 Laser Power Chart as a Function of Displacement

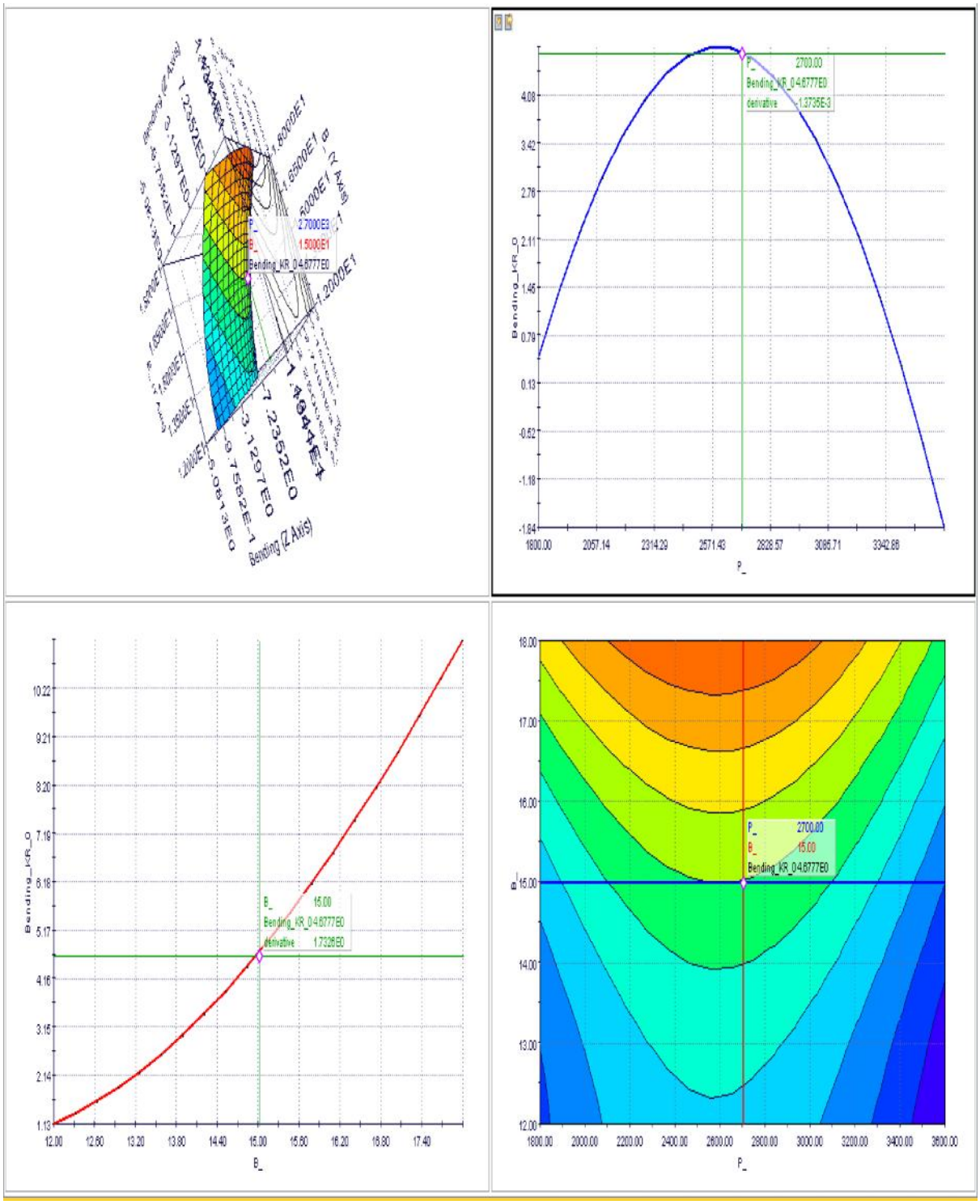

Figure D.5 3D Laser Power Chart as a Function of Displacement

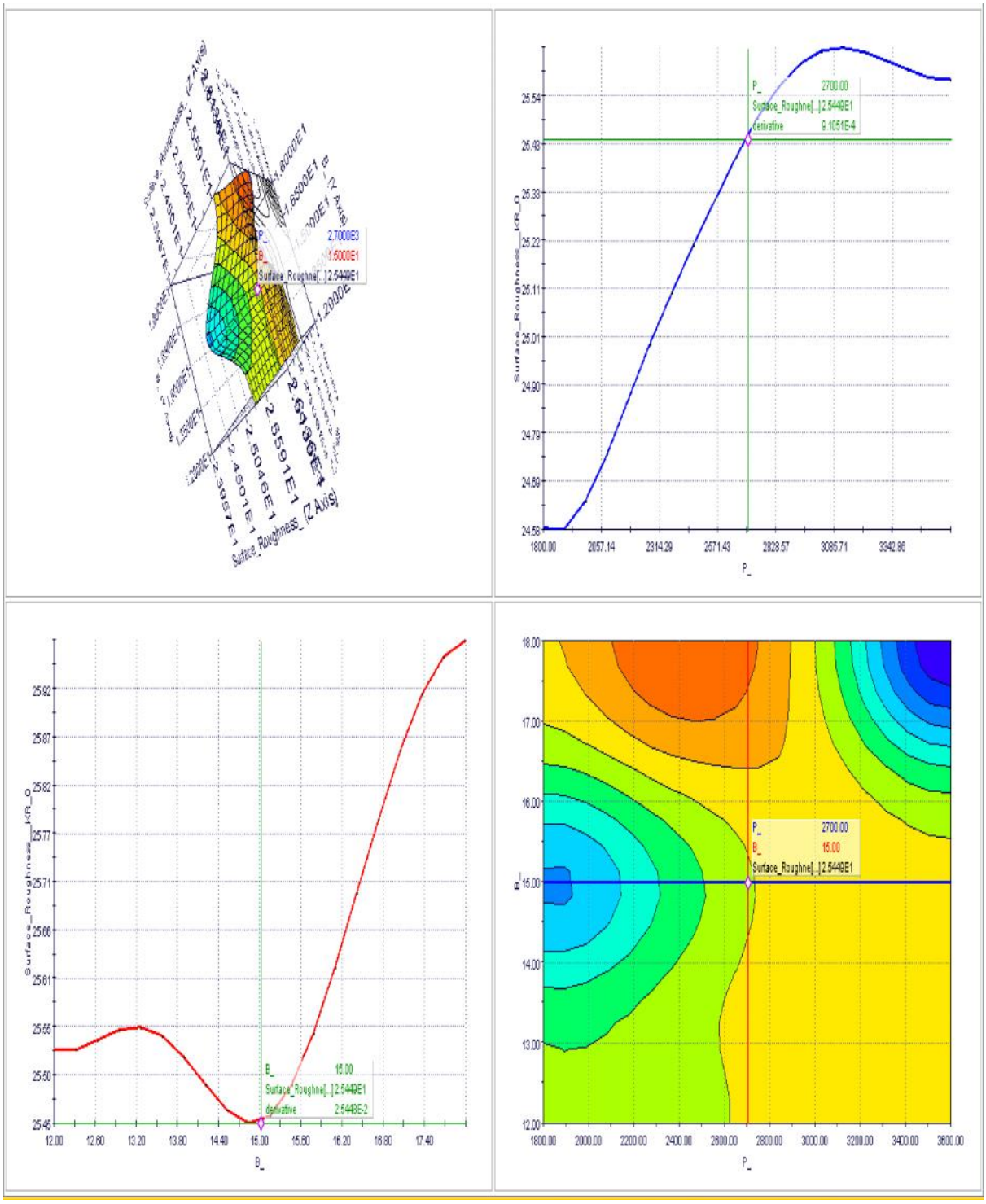

Figure D.6 Laser Power Chart as a Function of Displacement

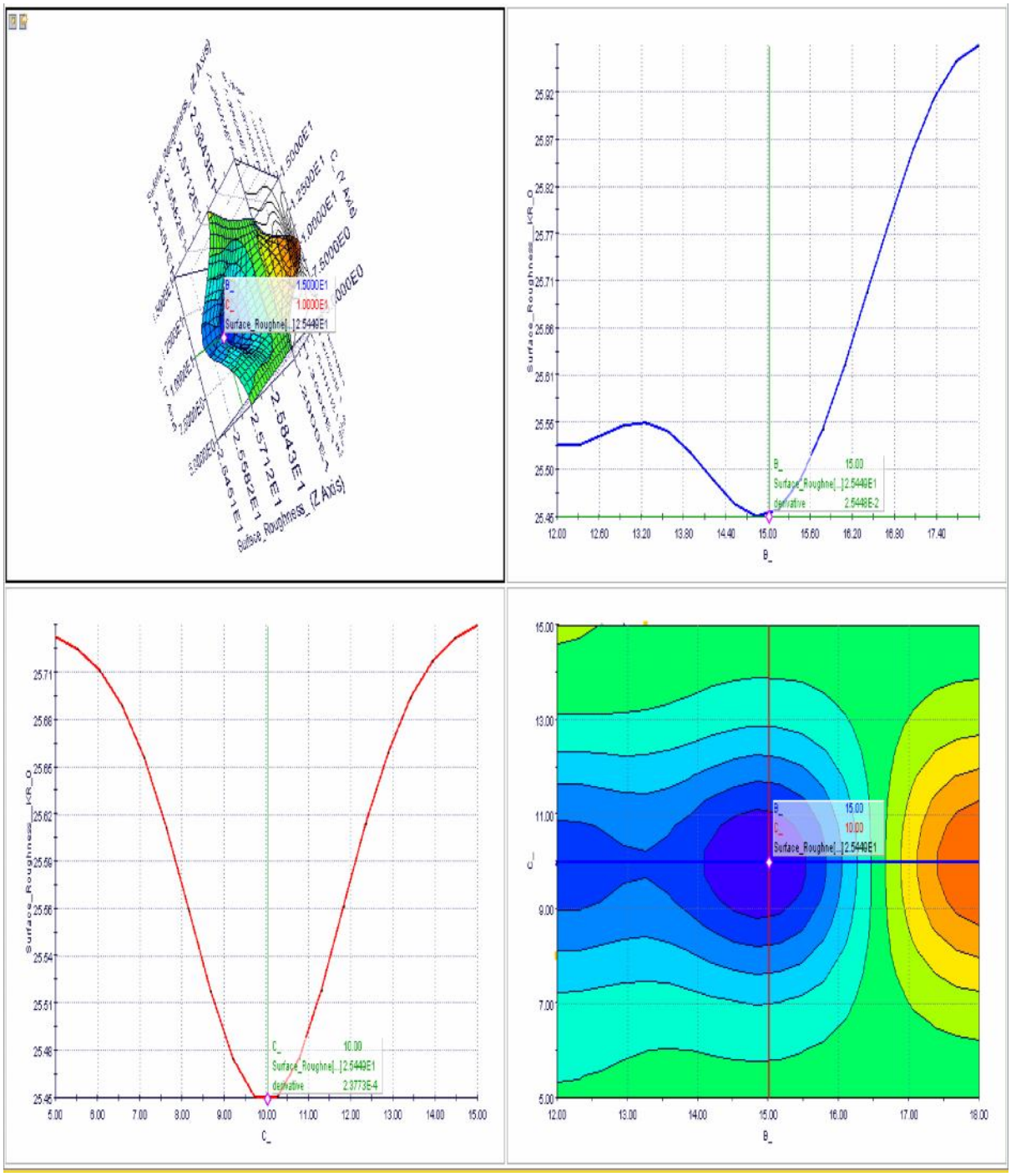

Figure D.7 Cooling Rate Chart as a Function of Displacement

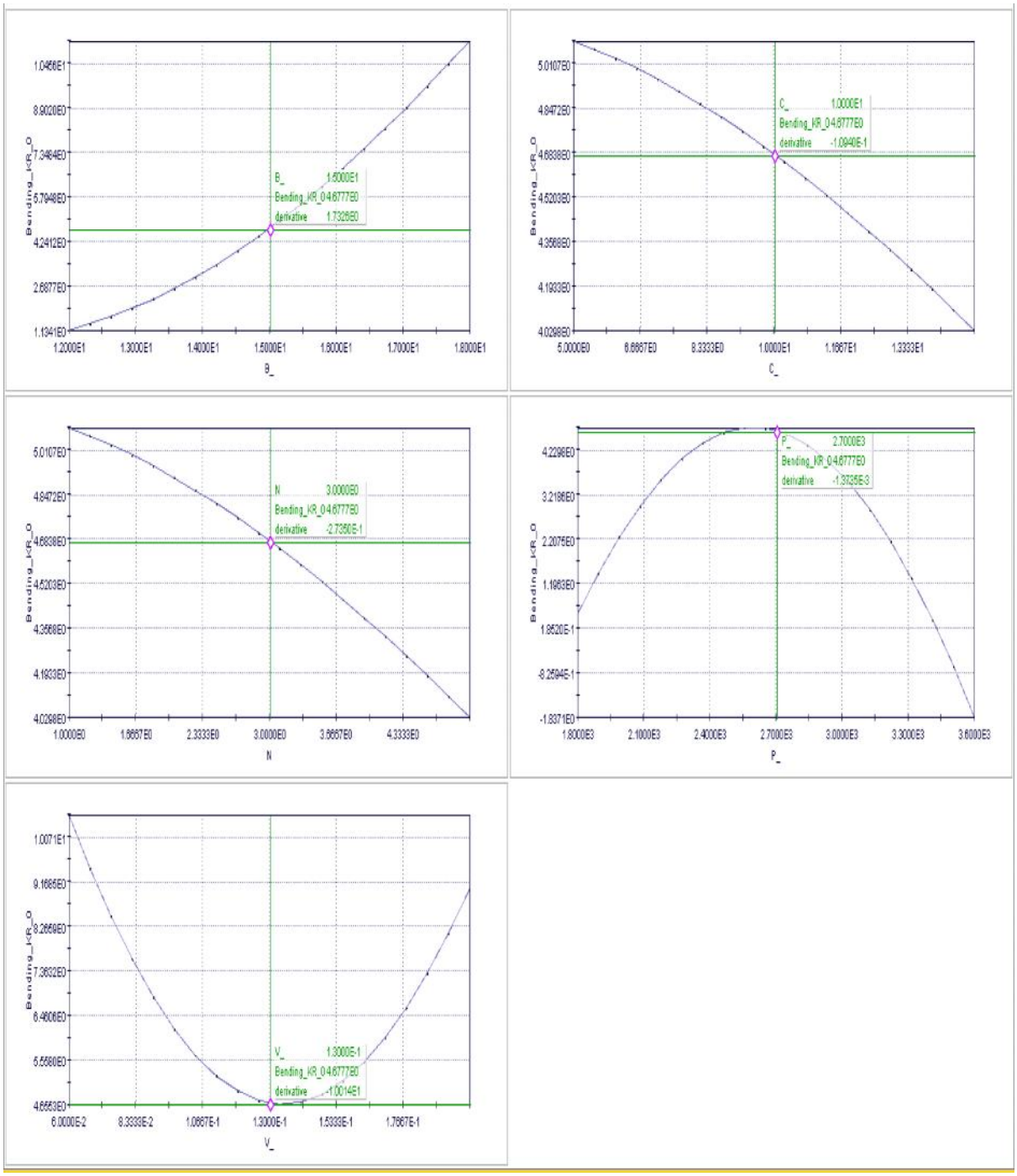

Figure D.8: Function Charts Representing Bending Kriging response as a function for each process input parameter

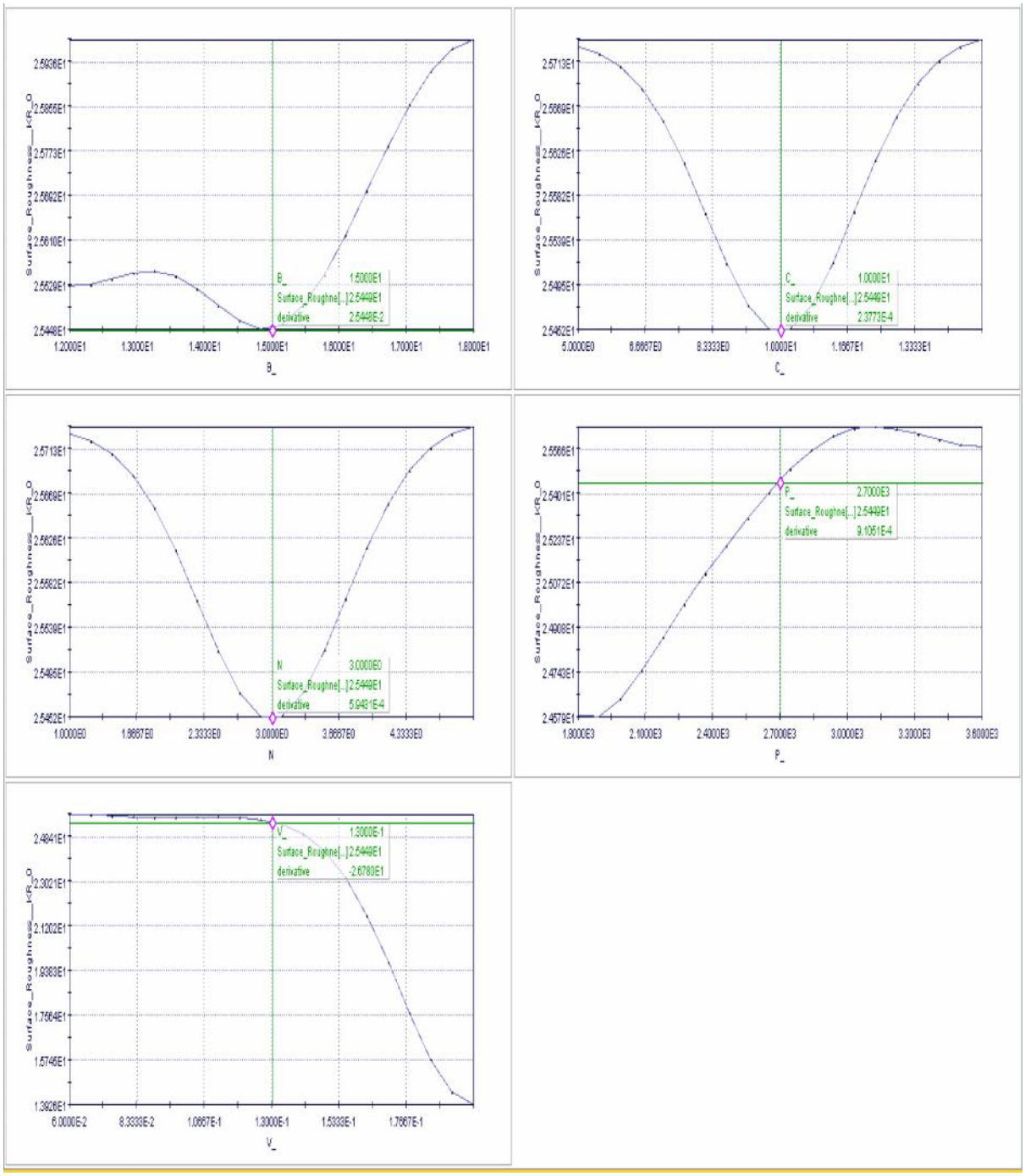

Figure D.9 Function Charts Representing Surface Roughness Kriging response as a function for each process input parameter